Experimental Studies of Highly Charged Ions in a Penning Trap for the Measurement of Electron Magnetic Moments by Double-Resonance Spectroscopy

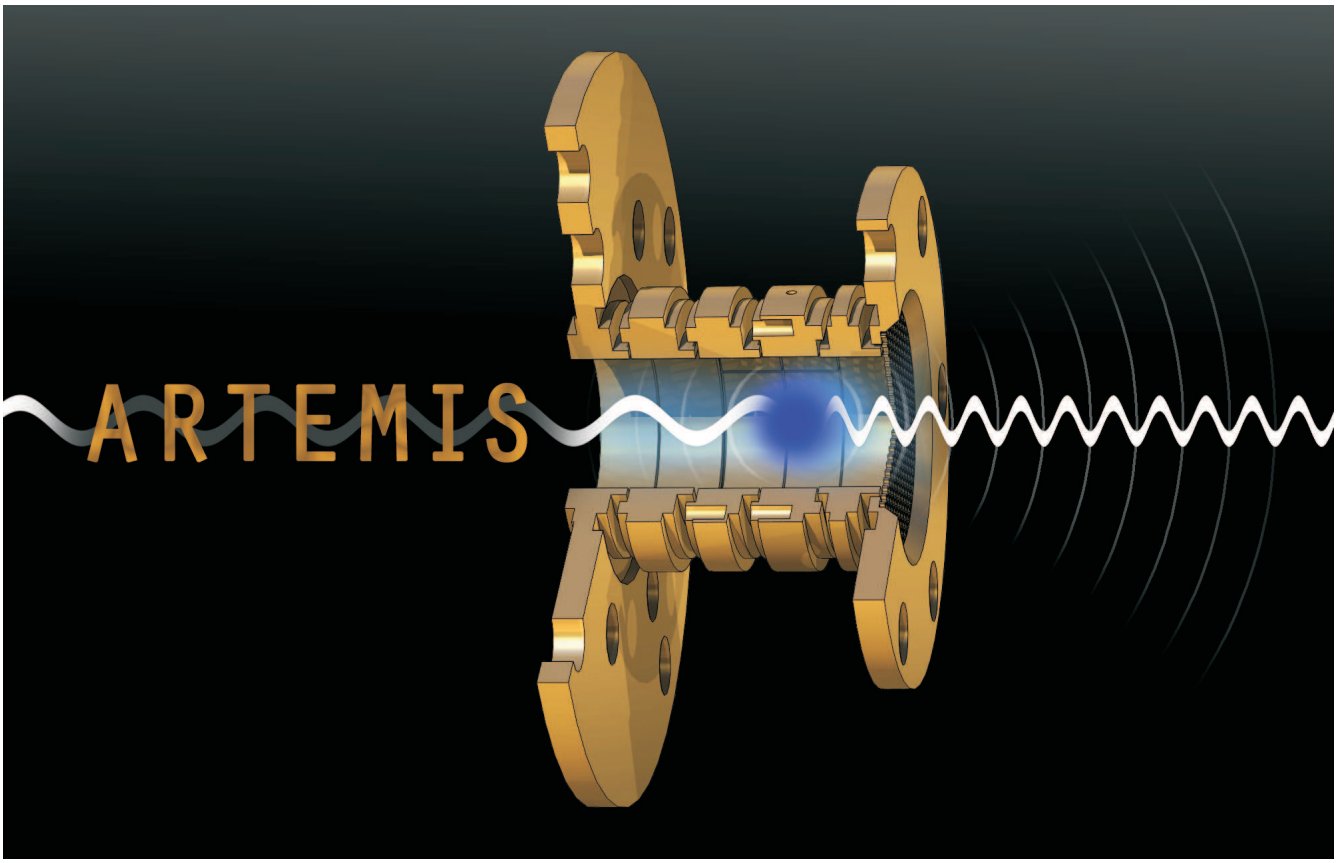

David von Lindenfels

Dissertation
submitted to the
Combined Faculties for the Natural Sciences and for Mathematics
of the Ruperto-Carola University of Heidelberg, Germany
for the degree of
Doctor of Natural Sciences

Put forward by

David-Friedrich Freiherr von Lindenfels

Born in Lüneburg

Oral examination: 18.11.2015

Experimental Studies of Highly Charged Ions in a Penning Trap for the Measurement of Electron Magnetic Moments by Double-Resonance Spectroscopy

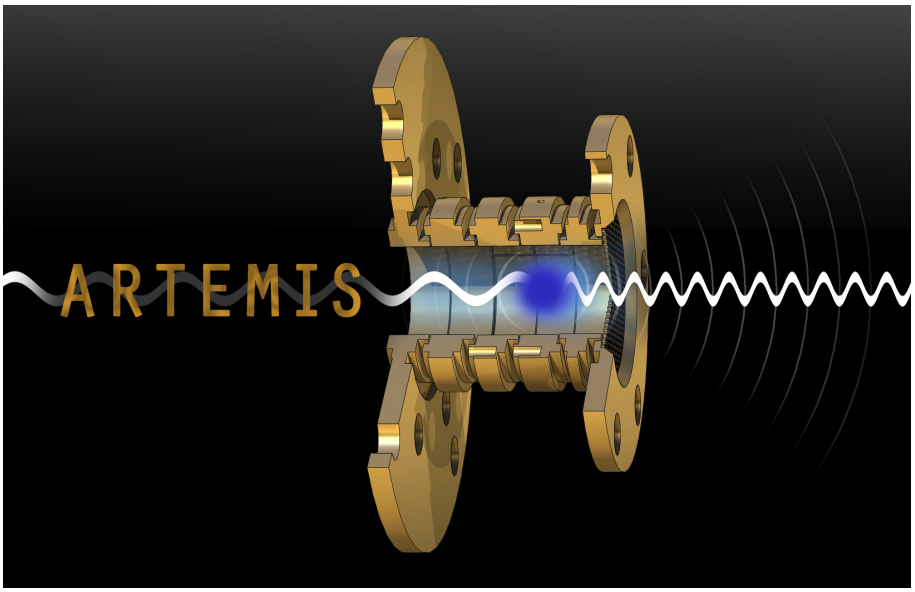

Referees: Priv.-Doz. Dr. Wolfgang Quint

Prof. Dr. Markus Oberthaler

Experimentelle Studien mit hochgeladenen Ionen in einer Penningfalle zur Messung magnetischer Momente von Elektronen mithilfe von Doppelresonanzspektroskopie.

Zusammenfassung: Durch präzise Messungen von g-Faktoren gebundener Elektronen in hochgeladenen Ionen werden die aktuellsten theoretischen Berechnungen überprüft, die unter anderem relativistische Effekte der Elektronenkorrelation, die QED gebundener Zustände und Zeeman-Effekte höherer Ordnung berücksichtigen. Mit Laserstrahlung regen wir den Feinstrukturübergang in Bor-ähnlichem Argon ($^{40}Ar^{13+}$) an und messen Mikrowellenübergänge zwischen Zeeman-Unterzuständen im Magnetfeld einer Penningfalle. Diese Laser-Mikrowellen Doppelresonanztechnik erlaubt mit unserem Versuchsaufbau eine Bestimmung des g-Faktors mit neunstelliger Genauigkeit. Wir haben eine neuartige „halboffene“ Penningfalle mit hoher Fluoreszenznachweiseffizienz und einer eingebauten Elektronenstrahl-Ionenquelle zur Erzeugung hochgeladener Ionen aus Gas aufgebaut, welches durch ein kryogenes Ventil eingelassen wird. In Zukunft sollen schwerere Ionen aus der HITRAP-Anlage bei GSI eingefangen und die Spektroskopiemethode auf den Hyperfeinstrukturübergang von Wasserstoff-ähnlichem Bismut ($^{209}Bi^{82+}$) angewandt werden, um magnetische Momente von Elektronen und Kernen zu messen. Diese Arbeit stellt experimentelle Entwicklungen sowie Erzeugung, Kühlung, Transport und dauerhafte Speicherung hochgeladener Argon-Ionen vor.

Titel: Logo des ARTEMIS Experiments, englisches Akronym für „Asymmetrische Falle zur Messung magnetischer Momente von Elektronen in Ionen“. Es stellt die vergoldete Spektroskopiefalle mit einer angedeuteten blauen Ionenwolke dar.

Experimental Studies of Highly Charged Ions in a Penning Trap for the Measurement of Electron Magnetic Moments by Double-Resonance Spectroscopy.

Abstract: A precise measurement of bound-electron g factors in highly charged ions provides stringent tests for state-of-the-art theoretical calculations, such as relativistic electron-correlation, bound-state QED, and higher-order Zeeman effects. We excite the fine-structure transition of boronlike argon ($^{40}Ar^{13+}$) with laser radiation and probe microwave transitions between Zeeman sub-levels in the magnetic field of a Penning trap. From this laser-microwave double-resonance technique the g factor can be determined on a ppb level of accuracy in our apparatus. We have built a novel 'half-open' Penning trap with high fluorescence-detection efficiency and an integrated electron-beam ion source for production of highly charged ions from gas, injected through a cryogenic valve. In the future, heavier ions shall be captured from the HITRAP facility at GSI and the method shall be applied to hyperfine-structure transitions of hydrogenlike bismuth ($^{209}Bi^{82+}$) in order to measure electronic and nuclear magnetic moments. This thesis presents experimental developments as well as production, cooling, transport, and long-term storage of highly charged argon ions.

Title: Logo of ARTEMIS, the 'AsymmetRic Trap for the measurement of Electron Magnetic moments in IonS', depicting the gold-plated spectroscopy trap with a blue ion cloud indicated.

Contents

List of Figures

List of Tables

Chapter 1

Introduction

– Why another g-Factor Experiment? –

What would we require of an experiment in physics? First, it should aim at fundamental characteristics of nature, such as the properties of elementary particles, the strength of their interactions, or the consistency of our theoretical description thereof. Then, a quantity should be picked that relates to the basic laws of nature without much need of interpretation. Last, the experiment should be carried out with high precision.

Heavy highly charged ions are suitable candidates for being object of a measurement, since the strong electromagnetic fields close to a heavy nucleus enhance the effects of atomic physics, which have first been understood by the study of neutral atomic hydrogen. Phenomena such as fine and hyperfine structure and the Lamb shift are magnified to the visible optical regime and beyond. This makes them in many cases easier to observe, for instance by laser-spectroscopic methods; it also increases sensitivity in the isolation of the individual contributions, such as relativistic and quantum-electrodynamic effects.

Precision is achieved by the choice of a cryogenic Penning trap as measurement apparatus. It features long storage time for particles in well-defined conditions and with potentially high density. Over the course of the past decades, many instruments and methods have been developed to exploit the potential of this device.

The magnetic field of a Penning trap causes angular momenta of the intrinsic spin and the classical ion motion to assume well-defined frequencies, namely the cyclotron frequency and the Larmor frequency of the Zeeman effect. This is of particular advantage, since frequencies are the most precisely measured observable in physics. From these we can derive ratios of masses or magnetic moments. So together with a mass standard, a Penning trap is a very accurate scale.

Likewise, the ratio of the magnetic moment and the angular momentum of an elementary particle can be determined. This ratio, called gyromagnetic (g) factor, is well suited for probing fundamental physics, because it is very sensitive to the quantum nature of physics. Quantum electrodynamics (QED), the quantum theory of interaction between charged particles and electromagnetic fields [Fey49], predicts phenomena such as self energy, vacuum polarization and combinations of these. These effects manifest themselves by an observable deviation in the magnetic moment from the predictions by pure relativistic theory. In different systems, such as free versus bound electrons, light versus heavy elements, the g factor has individual values, caused by the

variable magnitude of relativistic, quantum-electrodynamical, nuclear, and other contributions.

The latest experimental result of the free-electron g factor is $2\times1.001\,159\,652\,180\,73(28)$ [HFG08], while relativistic theory has exactly 2 [Dir28]. The experiment is the currently most stringent test of free QED theory, which could even be enhanced with a more precise value of the fine-structure constant $\alpha = e^2\hbar c/(4\pi\varepsilon_0)$. This dimensionless parameter measures the strength of the electromagnetic interaction and is the cardinal point for the perturbative approach to QED, which obtains all results as a power series in the small parameter α/π. It predicts $2\times1.001\,159\,652\,181\,643(38)(763)$, where the larger error contribution results from the uncertainty of the currently best independent value of α^{-1}, namely $137.035\,999\,037(91)$, which originates from rubidium recoil measurements [BCG$^+$11]. Therefore the combination of highly precise experiments and theoretical calculations is used to determine that quantity to a value of $137.035\,999\,157(33)$ [AHKN15].

The g-factor measurement of electrons bound in neutral gallium atoms [KF47, KF48], together with the discovery of the Lamb shift [LR47], and their respective explanations by QED [Sch48, KL49] brought the young theory to breakthrough as a predictive formalism. This was only after quantum mechanics had been well established for massive particles, both non-relativistic [Sch26] and relativistic [Dir28]. The quantum behavior of nature has however first been discovered with electromagnetic fields [Pla00, Ein05] and can thus claim a longer history. It took half a century of brilliant ideas to develop a consistent mathematical description for the quantized field theory. And still, the perturbative formalism of a power-series expansion in α/π is known to be insufficient: It is an asymptotic series which does not converge, but at a certain level, higher orders start growing again. Hence this method cannot be the conclusion in this quest.

Composite systems of one or several electrons bound to a nucleus open a variety of other interesting aspects in contrast to free electrons. Hydrogenlike (one-electron) ions allow a very precise theoretical treatment as a two-body problem. The single electron is exposed to the unshielded nuclear fields, which are extraordinarily strong. Especially for heavy ions, the average electric field is of the order of 10^{16} V/cm, see Fig. 1.1. This is not only caused by the Z-times stronger field at a fixed position, but also by the roughly Z-fold contracted electronic wave functions, hence the approximate Z^2-dependence of the principal transition energies in hydrogenlike ions.

This has several consequences. Firstly, the high density of virtual photons enhances QED effects correspondingly. Then, other contributions appear, or even predominate over the quantum-electrodynamic corrections. Among the effects depicted in Fig. 1.2, the relativistic correction is by far the strongest, which has been analytically calculated by Breit [Bre28]. Nuclear effects are competing with the QED terms and are less well known. This is where lithium- and boronlike (3- or 5-electron) ions enter: Due to the exclusion principle, these ions have ground-state valence electrons in the $2s$, and $2p$ orbitals, which have different properties from the $1s$ state. Thus, the nuclear effects can be eliminated by the comparison of different charge states of the same (heavy) isotope [SGO$^+$06]. This allows a stringent test of QED in extreme fields and thus another independent determination of α.

The finite orbital angular momentum of a P term couples to the spin momentum, which leads to a spectroscopic fine structure—as it is named because in neutral atoms this effect splits optical transitions by a few GHz. In highly charged ions, the energy difference is enhanced with the fourth power of nuclear charge and itself gets shifted into the visible regime. For instance, the two levels of the $P_{1/2}-P_{3/2}$ doublet in boronlike Ar^{13+} are separated by 680 THz, which corresponds 441 nm

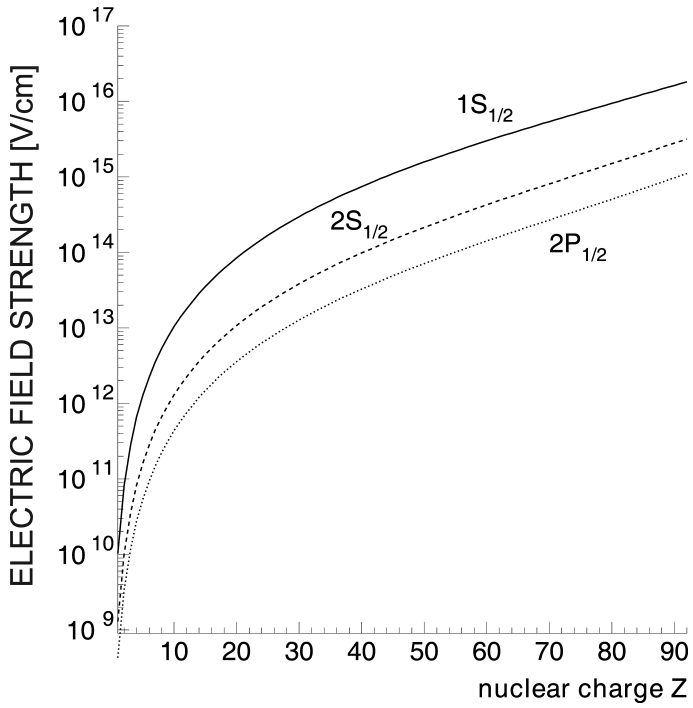

Figure 1.1: Expectation value for the electric field of a nucleus with charge Z, at the position of a single electron in the lowest bound states.

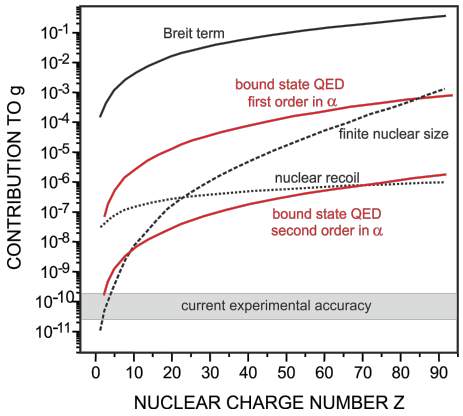

Figure 1.2: Contributions to the g factor of a single $1s$ electron bound to a nucleus with charge Z.

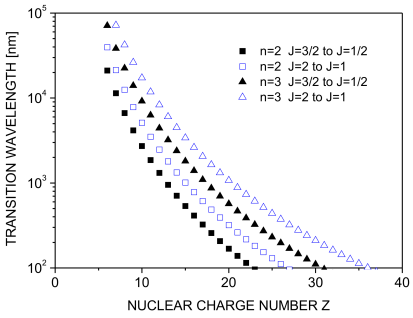

(a) Estimation of the fine-structure transition wavelength, by the transition energy of an electron bound to a nucleus with charge number Z, excited to different states.

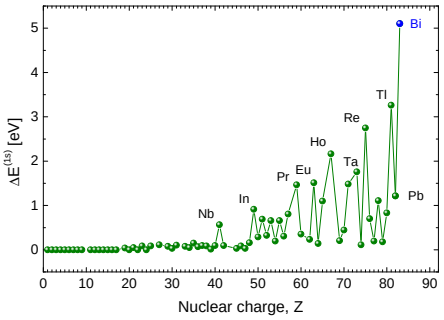

(b) Hyperfine-structure transition energy of a single $1s$ electron bound to a suitable nucleus with charge Z.

Figure 1.3: The smooth Z^4-dependence of the fine-structure splitting (inverse of wavelength) vs. the hyperfine-structure splitting, which is proportional to Z^3 and the nuclear magnetic moment.

wavelength. Figure 1.3(a) lists transition wavelengths for fine-structure splittings at different principal quantum number n, obtained from Dirac theory (single relativistic electron in the central field of a point-like nucleus [Dir28]), depending on the nuclear charge number Z. If the electronic terms were realized by a valence electron in the ground state of B-, O-, Al-, and S-like ions, the effect of closed electronic shells would have to be accounted (screening correction), and the wavelength would shift a little. Still, the nuclear charge enhances the fine-structure splitting very strongly. This offers the possibility for laser-microwave double-resonance (LMDR) spectroscopy as a complementary method to the continuous Stern-Gerlach effect, which is used for systems with s electrons, where no other magnetic moments play a role.

In a similar way as for the free electron, precise g-factor measurements with a bound electron are combined with accurate theory for the determination of fundamental constants. In this case, a weak point of the theory test is the electron mass. So the measurements of hydrogenlike carbon [HBH$^+$00], oxygen [VDS$^+$04], and silicon [SWS$^+$11] have been exploited to propose a new value. The measurement with the mass standard carbon has recently been refined and resulted in $m = 0.000\,548\,579\,909\,067(17)$, measured in atomic units [SKZ$^+$14].

Apart from the electric effects, the hyperfine-structure splitting is induced by the magnetic field of a spin-carrying nucleus, and likewise increases due to the proximity of an electron bound to a heavy nucleus. For hydrogenlike bismuth ($^{209}Bi^{82+}$), the transition is even in the ultraviolet regime, which is also due to the extremely high nuclear spin of $I = 9/2$, see Fig. 1.3(b). Again, double-resonance spectroscopy can be employed. Here, it serves to disentangle the electronic magnetic moment from the one of the nucleus. The latter can thus be determined without diamagnetic shielding due to closed electron shells [QMSV08]. The studies with double-resonance spectroscopy of Ar^{13+} are technically related to the case of $^{209}Bi^{82+}$. Thus they have an additional motivation as commissioning of the apparatus for later use with heavy ions.

Besides the determination of fundamental constants, we can focus on particular theoretically predicted phenomena. Lithiumlike and boronlike ions allow a study of correlation of a valence electron with closed electron shells. Apart from that, theoretical treatment of a 3-electron system

requires to consider negative-energy states in the Dirac sea, which calls for experimental confirmation. Boronlike ions feature a low-lying excited state, which modifies the magnetic moment, depending on the magnetic field. At a field strength of 7 Tesla, this higher-order Zeeman effect significantly changes the Larmor frequency from the expectation of a constant magnetic moment. This non-linear behavior shall be studied in the present thesis, along with the linear Zeeman effect. The investigation has been proposed in an earlier publication [LWG$^+$13], from which I drew some parts in the introduction and the following chapters.

The thesis is organized in four main parts. A theoretical introduction to the concept of first- and higher-order Zeeman effects is followed by a proposition how these contributions can be measured in a Penning-trap apparatus. Our experimental setup with instruments for electronic and optical detection is presented in the subsequent chapter. The last part explains the implementation of a measurement and reports successful production, transport, and storage of ions. The document is concluded with an outlook to the steps required for accomplishing the measurement.

Chapter 2

Theoretical Description

– The non-linear magnetic moment of a ^2P electron –

This chapter presents the theoretical background of bound-electron magnetic moments, alongside with a definition of the quantities of interest. The primary goal of our experiment is to measure the magnetic moment of bound electrons, as it appears in the linear Zeeman effect of optical spectroscopy. Boronlike argon (Ar^{13+}, ArXIV) is a first test candidate with the prospect of testing other interesting physics with heavier ions. After a first hint to nonlinear behavior as a function of the magnetic field B in [Lin10, p. 9], the aspect of strong-field effects was thoroughly studied in [LWG+13]. The most important ideas and predictions shall be summarized in this chapter. The last section gives an overview of further literature for the Zeeman effect, wavelength, and lifetime in this atomic transition.

2.1 The Linear Zeeman Effect

A spinning body with given spatial distribution of charge $\rho_Q(\vec{r})$ and mass $\rho_M(\vec{r})$ can be assigned an angular momentum

$$\vec{L} = \int \mathrm{d}^3 r \; \rho_M \, \vec{r} \times \vec{v}$$

and a magnetic (dipole) moment

$$\vec{\mu} = \frac{1}{2} \int \mathrm{d}^3 r \; \rho_Q \, \vec{r} \times \vec{v},$$

according to [Jac75]. We can define the gyromagnetic ratio of such a system (ratio between the vector quantities) and compare it to $\frac{Q}{2M}$ times the angular momentum, Q and M being the total charge and mass, respectively, of the body. If the two distributions are proportional to each other and do not, for instance, have different r.m.s. radii, then the ratio is simply equal $\frac{Q}{2M}$. Deviations indicate more complicated structure.

For quantum particles with half-integer spin, the Bohr magneton is introduced, which for the electron reads $\mu_B = e\hbar/2m = 58\,\mu\mathrm{eV/T} = 14\,\mathrm{GHz/T}$, with the charge e and mass m of the

electron and Planck's constant, $\hbar$. This is used to define the dimensionless gyromagnetic (hence g), or Landé factor,

$$\frac{\vec{\mu}_J}{\mu_B} = g_J \cdot \frac{\vec{J}}{\hbar}. \tag{2.1}$$

According to the nature of the angular momentum (S for spin, L for orbital, J for total electronic momentum etc.), a subscript is attributed, e.g. g_L, g_S. Again, this quantity gives insight into fundamental properties of the considered particle: An orbital angular momentum satisfies the expectation from non-relativistic quantum mechanics, $g_L = 1$, while the spin momentum does not, as pointed out in the introduction. An external magnetic field $\vec{B}$ induces an anisotropic potential,

$$V_{\vec{\mu}} = -\vec{\mu} \cdot \vec{B}, \tag{2.2}$$

in which the magnetic moment precesses with the Larmor frequency ν_L. The motion is quantized to energy levels with the spacing

$$\Delta E = h\nu_L = g_J \mu_B B, \tag{2.3}$$

corresponding to a change of the projection $M_J \cdot \hbar$ by one quantum.

In this thesis, we consider the boronlike charge state of the most abundant argon isotope, $^{40}Ar^{13+}$, having zero nuclear spin. It has two closed s shells and a $2p$ valence electron. With the spin of that electron, a fine-structure doublet (LS-coupling) of the levels $^2P_{1/2}$ and $^2P_{3/2}$ is formed. The metastable excited state ($J = 3/2$) decays to the ground state ($J = 1/2$) with a magnetic dipole (M1) transition of 9.57 ms lifetime under emission of light at a wavelength of 441.26 nm in air (cf. table 2.4).

Dirac theory for a single electron bound to a point-like ^{40}Ar nucleus in these orbitals [Bre28] predicts

$$\begin{aligned} g_{1/2} &= \frac{2}{3} - \frac{1}{6}(Z\alpha)^2 + \cdots \approx 0.663\,8, \\ g_{3/2} &= \frac{4}{3} - \frac{2}{15}(Z\alpha)^2 + \cdots \approx 1.331, \end{aligned} \tag{2.4}$$

where $Z = 18$ is the nuclear charge, see [Lin10] and references therein. The currently best values for the five-electron ion take into account interelectronic interaction ($1/Z$ term and higher orders estimated), quantum electrodynamical (screening correction to the one-loop self-energy term, higher orders estimated), and nuclear recoil effects. The contribution of the negative-energy states is crucially important for the Zeeman effect [LWG+13, GVS+13]. The corrections enter at a level of 10^{-3}. Here is the latest update from [SGV+15]:

$$\begin{aligned} g_{1/2} &= 0.663\,647\,7(7), \\ g_{3/2} &= 1.332\,282(3). \end{aligned} \tag{2.5}$$

2.2 Higher-Order Contributions to the Zeeman Effect

The linear equation 2.3 with a constant g_J holds true exactly only in case of a point-like particle. In atomic systems, it serves as an approximation for low magnetic field. Perturbations arise from excited states that mix with the ground-state Zeeman sub-levels and shift these, as pointed out in [Lin10, LWG+13], and appear as a field-dependent $\vec{\mu}(B)$ in equation 2.2. The effect can be estimated by the relative strength of the fine-structure and Zeeman splittings. These can be seen as zeroth and first order of a power series expansion of the Zeeman effect (Eqn. 2.6). In the present case, with a field of around 7 Tesla, the Zeeman effect is roughly 4 orders of magnitude smaller than the fine-structure energy. According to this reasoning, higher orders in the magnetic field should shift the Larmor frequencies by $\Delta\nu_L/\nu_L \approx 10^{-4}, 10^{-8}$, and so forth. For an experimental accuracy aiming at a ppb (10^{-9}), this is by far not negligible. It needs to be corrected for by calculating the non-linear contributions with the same absolute accuracy as the first order. In turn, some of the non-linear terms can be probed with high sensitivity—section 3.1 is a recipe to resolve the shifts experimentally.

The above-mentioned power-series expansion of the field-dependent energy of a state $|A\rangle = |J,\, M_J\rangle$ has the form

$$\begin{aligned} E_A(B) &= E_A^{(0)} + \Delta E_A^{(1)}(B) + \Delta E_A^{(2)}(B) + \cdots \\ &= mc^2 \sum_i g_J^{(i)}(M_J) \cdot \left(\frac{\mu_B B}{mc^2}\right)^i , \end{aligned} \tag{2.6}$$

with M_J-dependent $g_J^{(i)}$ factors as dimensionless expansion coefficients. These express the strength of each contribution in terms of the magnetic field, rescaled by the Bohr magneton and the electron rest energy, mc^2. The values can be extracted from the definition:

The absolute magnitude of the **zeroth order** is up to definition - the binding energy of the valence electron is around $|E_b| = 750\,\mathrm{eV}$ below the onset of continuum, while the latter can be regarded as zero, or as $mc^2 = 511\,\mathrm{keV}$. The ground state can likewise be defined as reference level. The fine-structure splitting of $\Delta E_{\mathrm{FS}} = 2.81\,\mathrm{eV} = h \cdot 680\,\mathrm{THz}$ is however unambiguous:

$$\begin{aligned} E_A^{(0)} &= \begin{cases} E_0 & \text{for } J = 1/2 \\ E_0 + \Delta E_{\mathrm{FS}} & \text{for } J = 3/2 \end{cases} \\ \Leftrightarrow\ g_{3/2}^{(0)}(M_J) - g_{1/2}^{(0)}(M_J') &= \frac{\Delta E_{\mathrm{FS}}}{mc^2} \end{aligned}$$

The zero-field energies, and subsequently the $g_J^{(0)}$ factors, are independent of magnetic quantum numbers M_J.

The **first order** is given by the linear Zeeman effect, as described above. Still, g_J must not be confused with $g_J^{(1)}$, which contains the half-integer values of M_J:

$$\begin{aligned} \Delta E_A^{(1)}(B) &= g_J\, M_J\, \mu_B\, B \\ \Leftrightarrow\ g_J^{(1)}(M_J) &= g_J\, M_J \end{aligned} \tag{2.7}$$

Higher orders are derived in a perturbative QED framework by a non-linear interaction

(multiple vertices) with the external magnetic field. Like in the first cases, they obey odd or even symmetry relations:

$$\begin{aligned} g_J^{(2)}(-M_J) &= g_J^{(2)}(M_J) \\ g_J^{(3)}(-M_J) &= -g_J^{(3)}(M_J) \\ &\dots \end{aligned} \tag{2.8}$$

For an accurate treatment, the electron-correlation is evaluated rigorously, beyond the screening-potential approximation. Quantum-electrodynamical and nuclear-recoil effects are taken into account as well [LWG+13]. On top of this, the values depend strongly on the fine-structure energy and have therefore been calculated with the value taken from Artemyev [AST+07]. A list of higher-order g values as calculated in [LWG+13] is presented in table 2.1. Evaluation of the interelectronic-interaction correction has meanwhile improved accuracy of the quadratic order roughly by a factor of ten [Gla15]. Signs in the third order are correlated with the sign of M_J. The energy shifts they would produce at 7 Tesla are given in table 2.2. Errors are estimated according to the uncertainty of the linear g factors for the first order, and as 10% for the higher orders.

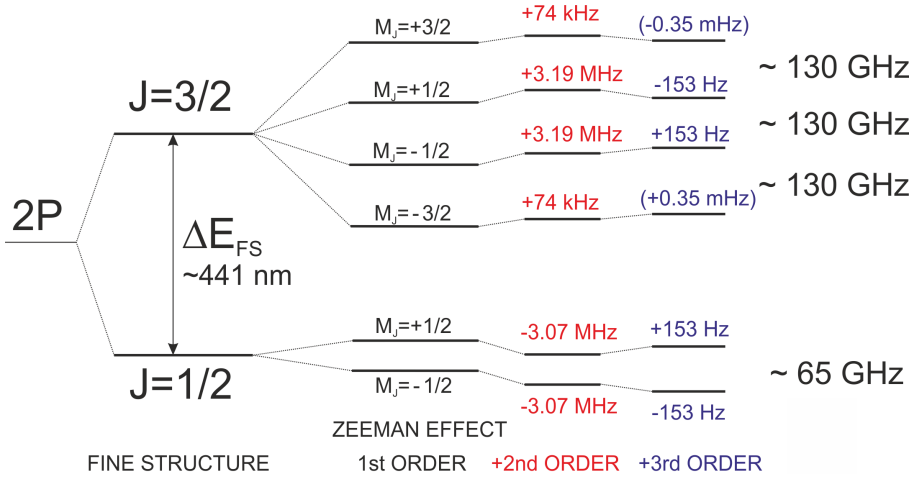

Figure 2.1: Level scheme of the $2\,^2P_J$ states of boronlike argon in an external magnetic field with higher-order contributions to the Zeeman effect (not true to scale). Figure taken from [LWG+13]

Table 2.1: $g_J^{(2)}$ [Gla15] and $g_J^{(3)}$ [LWG+13] factors for boronlike argon.

J, M_J	$g_J^{(2)}(M_J)$	$g_J^{(3)}(M_J)$
$3/2$, $\pm 3/2$	$1.007(15)\cdot 10^3$	$\mp 5.7(6)\cdot 10^3$
$3/2$, $\pm 1/2$	$41.20(15)\cdot 10^3$	$\mp 2.5(3)\cdot 10^9$
$1/2$, $\pm 1/2$	$-39.66(15)\cdot 10^3$	$\pm 2.5(3)\cdot 10^9$

The $\Delta E_A^{(2)}/h$ column of table 2.2 reflects the symmetry in the quadratic order as expressed

Table 2.2: Contributions to the Zeeman energy shifts for boronlike argon at 7 T. First, second, and third orders in the magnetic field are presented in terms of the frequencies $\Delta E/h$. Values taken from [LWG+13] and [Gla15].

J, M_J	$\Delta E_A^{(1)}/h$ [GHz]	$\Delta E_A^{(2)}/h$ [MHz]	$\Delta E_A^{(3)}/h$ [Hz]
3/2, +3/2	195.792 9(4)	0.078 2(10)	−0.000 35(3)
3/2, +1/2	65.264 3(1)	3.201(10)	−153(15)
3/2, −1/2	−65.264 3(1)	3.201(10)	153(15)
3/2, −3/2	−195.792 9(4)	0.078 2(10)	0.000 35(3)
1/2, +1/2	32.510 01(3)	−3.081(10)	153(15)
1/2, −1/2	−32.510 01(3)	−3.081(10)	−153(15)

in equation 2.8: A pair of sub-levels with equal J, $|M_J|$ are shifted in the same direction, so that the Larmor frequency in the ground state is not affected. The shift is however observable in the transition frequencies between $|M| = 3/2$ and $1/2$, which get raised or lowered by around 3 MHz in 131 GHz at 7 Tesla. The major part of that asymmetry originates from the $|M| = 1/2$ states due to the enhanced mixing with their equivalents of the other fine-structure level.

2.3 Zeeman Effect, Wavelength, and Lifetime

The figures so far are quoted from our main collaboration partners, the group of V.M. Shabaev at St. Petersburg State University, Russia. Their latest status has been published by A.A. Shchepetnov [SGV+15]. There are other calculations and measurements for g factors: In table 2.3, we compare their values to predictions by J.P. Santos and F. Parente (Laboratório de Instrumentação, Engenharia Biomédica e Física da Radiação (LIBPhys-UNL), Dep. Física, Faculdade de Ciências e Tecnologia, FCT, Universidade Nova de Lisboa, Portugal), who have included electronic correlation up to $n = 5$ as well as the Schwinger and bound-state self energy corrections [San15].

The group of J.R. Crespo López-Urrutia (Max-Planck-Institut für Kernphysik, Heidelberg, Germany) did several measurements with Ar^{13+} in an EBIT (electron-beam ion trap). R. Soria Orts determined g factors from the Zeeman splitting of fluorescence lines in the magnetic field of the EBIT [SCB+07]. Earlier, I. Draganić and V. Mäckel had measured the wavelength [DCD+03, MKB+11], while A. Lapierre experimentally determined the lifetime [LJC+05] of the fine-structure transition.

Our experiment incorporates laser spectroscopy of the ground-state fine-structure transition of boronlike argon (see chapter 3 for further detail), and therefore we are naturally determining the transition energy and lifetime. These quantities, in particular the lifetime, have been debated in the past, since there is a discrepancy between different theoretical results and the most recent and most precise measurement, as summarized in table 2.4.

L. Natarajan (Department of Physics, University of Mumbai, India) has included 470 orbitals and the frequency-dependent Breit interaction to her fully relativistic calculations on the lifetime of $^2P_{3/2}$ state of B-like Ar. J.P. Marques (BioISI - Biosystems & Integrative Sciences Institute, Faculdade de Ciências da Universidade de Lisboa, Portugal) has published his results with quantum-electrodynamic and electronic correlation contributions included, while K. Koc (Department of

Table 2.3: Calculated and measured values for the g factors, characterizing the linear Zeeman effect in the ground and excited fine-structure levels. g' values and uncertainties are calculated with Eqns. 3.4 and 3.5 from the other columns.

Reference	$g_{1/2}$	$g_{3/2}$	g'
calculated:			
Shchepetnov [SGV$^+$15]	0.663 647 7(7)	1.332 282(3)	3.333 198(9)
Santos [San15]	0.663 74(1)	1.332 40(1)	3.333 46(3)
measured:			
Soria Orts [SCB$^+$07]	0.663(7)	1.333(2)	3.336(9)

Computer Science, Pedagogical University, Kraków, Poland) specifies certain QED contributions, namely electron self-energy and vacuum polarization. As mentioned before, Koc provides alternative values with correction for the electron anomalous magnetic moment. A.N. Artemyev (Physikalisches Institut, Universität Heidelberg, Germany) presented an ab initio QED calculation with an effective-screening-potential approximation, adding the two lowest-order QED and electron-correlation effects [AST$^+$07]. In a more recent paper [AST$^+$13], he makes use of the extended Furry picture and four different screening potentials. The recommended value of the NIST atomic spectroscopy database is quoted for completeness, after the HD EBIT references.

All theoretical references list a value obtained from ab-initio calculations and then correct it for the experimentally measured transition energy. The corrected values mostly agree with the measurement within the 10^{-3} uncertainty, while the less accurate the wavelength can be predicted, the stronger discrepancy is produced in the direct lifetime calculation. It is striking to see that Koc's consideration of the anomalous magnetic moment ($*$) rather increases the discrepancy. These circumstances and the relatively low level of accuracy in the lifetime measurement by Lapierre et al. motivate us to investigate this issue and contribute to the discussion.

A short comment on the effect of a magnetic field to the results presented in table 2.4 is necessary, since theoretical predictions for both wavelength and lifetime are made without accounting for an external magnetic field, while our measurement as well as the ones in the Heidelberg EBIT are performed in a field of 5 to 8 Tesla. As indicated in the discussion of the quadratic Zeeman effect, this field strength has to be regarded as a rather weak perturbation to the spin-orbit coupling. Accordingly, the presence of an external magnetic field should be of low influence.

The leading-order modification is of course the linear Zeeman effect, which allowed the determination of g factors in [SCB$^+$07]. The field-free transition energy can however be derived from averaging the Zeeman-shifted frequencies as in [MKB$^+$11]. This method can even be improved by correcting for quadratic shifts on the level of 10^{-8} (cf. Eqn. 3.7), being below resolution of the above mentioned experiments.

The lifetime of a magnetic dipole transition is proportional to the third power of the energy splitting, and thus a shift of the frequency results in a threefold effect to the lifetime. In 8 Tesla, the maximum Zeeman shift amounts to 185 GHz, leading to almost 10^{-3} relative change in lifetime, which is on the edge of detectability in [LJC$^+$05]. One could imagine that lifting the degeneracy of Zeeman sub-levels by a magnetic field might even have principle consequences beyond the gradual

Table 2.4: Several calculated and measured values for the transition wavelength and lifetime of the fine-structure transition in boronlike argon. In the last column, lifetime calculations are corrected for experimental transition energy. Koc also corrected calculations for the anomalous magnetic moment (*).

Reference	λ [nm, air]	τ [ms]	corr. τ [ms]
calculated:			
Natarajan [Nat14]	441.30(4)	9.575 9(24)	9.573 6(24)
Artemyev [AST$^+$13]	441.241(58)		
Marques [MIP12]	440.19(2)	9.513(1)	9.583(1)
Koc [Koc09]	441.173(33)	9.576 9	9.582 8
Koc* [Koc09]		9.533	9.538 4
Artemyev [AST$^+$07]	441.261(70)		
measured:			
Mäckel [MKB$^+$11]	441.255 68(26)		
Lapierre [LJC$^+$05]		9.573(4)(5)	
Draganić [DCD$^+$03]	441.255 9(1)		
NIST [RKRN11]	441.255 6		

effects estimated above. However, all sub-levels of the upper state have the same lifetime (in the zero-field limit, as demonstrated in App. B), which is clear because they are just differing in the projection of a vector to an almost arbitrary quantization axis. And in practice, it would never be possible to place ions into a completely field-free environment and thus restore isotropy.

Chapter 3

Measurement Principle

– Laser-spectroscopic measurement in a Penning trap –

The 'AsymmetRic Trap for the measurement of Electron Magnetic moments in IonS' (ARTEMIS) is a Penning trap experiment for measuring g factors of bound electrons by laser-microwave double-resonance spectroscopy [LBB$^+$11]. The Larmor frequency of such systems, stored in a magnetic field of several Tesla strength, is in the range of a hundred GHz, see Eqn. 2.3. Transitions between adjacent spin states can thus be excited by resonant microwave radiation.

We assume an atomic ion with an excited electronic state a few electronvolts above the ground state. This is suitable for laser spectroscopy with a level scheme as depicted in Fig. 3.1, for instance. Laser radiation with the frequency ν_6 can drive a closed transition between extremal Zeeman sub-states, provided there are ions in the state $|1/2, +1/2\rangle$. Hence, the optical fluorescence signal serves for probing population of Zeeman sub-levels of atomic terms. Appearance or disappearance of optical scattering can therefore be used to detect a microwave resonance. An electrode configuration for efficient collection of fluorescence light, emitted axially upon laser excitation of stored ions, has been designed for this kind of measurements. More details about the properties of the trap can be found in section 4.3.

Currently there is no microwave excitation available in our experimental setup, so section 3.1 is dedicated to the conclusions which can be drawn from a pure laser-spectroscopic measurement. A more general treatment of laser-microwave double-resonance spectroscopy and its application to various atomic systems is given in [QMSV08, LWG$^+$13].

The uncertainties in determining the Larmor frequency by purely optical spectroscopy are of the order of some MHz—in contrast to the foreseen sub-Hz resolution of a microwave scan. Still we can easily resolve the Zeeman splitting of 65 GHz. This should allow for an improvement of the magnetic moment measurement to the 10^{-4} level of accuracy, and perhaps a first experimental hint to a nonzero quadratic effect.

According to Eqn. 2.3, the second experimental ingredient of a g-factor measurement—besides the Larmor frequency—is the magnetic field calibration. Section 3.2 relates the B field to the motion of ions stored in a Penning trap. Frequency shifts due to the size of an ion cloud are estimated in section 3.3. Section 3.4, presents the mechanism we use for detection of ions and their motions. The last part of this chapter, section 3.5 discusses error propagation.

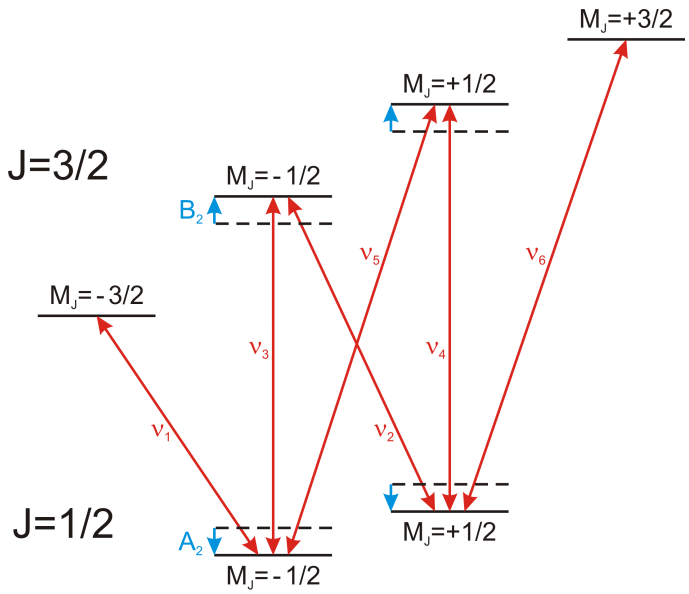

Figure 3.1: Spectroscopy of the $2\,^2P_{1/2}$—$2\,^2P_{3/2}$ fine-structure transition, as in a boronlike argon ion, with Zeeman effect. The level scheme (not true to scale) and all optical transitions (red double arrows) are shown. The major higher-order contributions, namely the shifts of the $|M_J| = 1/2$ sub-levels, quadratic in the magnetic field, A_2 and B_2, are shown as blue arrows

3.1 Disentangling Optical Transition Frequencies

One way to resolve the shifts that appear in the expansion 2.6 would be by varying the field strength, but this is not an option for the present apparatus. Other than that, measuring individual frequencies of multiple transitions within the two fine-structure levels allows to disentangle the linear from the quadratic order, if we neglect the cubic effect. We can distinguish different cases, depending on which of the optical transitions are observable with the required precision. To this end, the energy shifts of all states are abbreviated with capital A_i, B_i, B'_i. Note that the definitions differ from the small a_i, b_i, b'_i in [LWG+13]:

$$\begin{aligned}
A_i &\equiv |\Delta E^{(i)}_{|1/2,\,1/2\rangle}(B)| = |\Delta E^{(i)}_{|1/2,\,-1/2\rangle}(B)|, \quad i = 1,2,3,\\
B_i &\equiv |\Delta E^{(i)}_{|3/2,\,1/2\rangle}(B)| = |\Delta E^{(i)}_{|3/2,\,-1/2\rangle}(B)|, \quad i = 1,2,3,\\
B'_i &\equiv |\Delta E^{(i)}_{|3/2,\,3/2\rangle}(B)| = |\Delta E^{(i)}_{|3/2,\,-3/2\rangle}(B)|, \quad i = 1,2,3.
\end{aligned}$$

Mind the symmetry equations 2.8 for the inversion of M_J. For clarification, here is the relation with generalized X, standing for the state:

$$X_i = mc^2\,|g^{(i)}_X(X)|\left(\frac{\mu_B B}{mc^2}\right)^i.$$

Keeping in mind the symmetry relations 2.8, the A, B, B' define all frequencies. Their values are listed in table 3.1. We assume the magnetic field to be exactly equal to 7.003 T, such that the values of the shifts do not unnecessarily suffer from current uncertainties. Once the field is known

more precisely, the numbers can be rescaled.

Table 3.1: Summarized A_i, B_i, B'_i Zeeman shifts for boronlike argon, at 7.003000 T.

expans. order	A_i [GHz]	B_i [GHz]	B'_i [GHz]
1^{st}	32.523 95(3)	65.292 3(1)	195.876 8(4)
2^{nd}	0.003 084(10)	0.003 203(10)	0.000 078 3(10)
3^{rd}	0.000 000 154(15)	0.000 000 154(15)	0.000 000 000 000 35(3)

The B' and most higher-order terms are of minor relevance for the following reasons: The simple relation 2.7 for the first order implies $B'_1 = 3B_1$, rendering explicit use of B'_1 unnecessary. Among the higher orders, only A_2 and B_2 are in range of experimental resolution, see table 2.2 and section 3.5.1. We will however keep the smaller shifts in the calculation, marked in gray, and at suitable places mention their relevance. Particularly in equations 3.3, 3.7, and 3.9, which define how to disentangle the relevant shifts, the total amount of perturbations at 7.003 T is specified. In case of increased spectroscopic precision or magnetic field strength, these contributions might be of interest.

The optical transitions 1 through 6 as in Fig. 3.1 can be written in these terms as:

$$\begin{aligned}
\nu_1 &= \Delta E_{\text{FS}} + A_1 - 3B_1 + A_2 + B'_2 + A_3 + B'_3 = \Delta E_{\text{FS}} - 163.349\,7(4)\,\text{GHz} \\
\nu_2 &= \Delta E_{\text{FS}} - A_1 - \ B_1 + A_2 + B_2 - A_3 + B_3 = \Delta E_{\text{FS}} - \ 97.809\,9(1)\,\text{GHz} \\
\nu_3 &= \Delta E_{\text{FS}} + A_1 - \ B_1 + A_2 + B_2 + A_3 + B_3 = \Delta E_{\text{FS}} - \ 32.762\,0(1)\,\text{GHz} \\
\nu_4 &= \Delta E_{\text{FS}} - A_1 + \ B_1 + A_2 + B_2 - A_3 - B_3 = \Delta E_{\text{FS}} + \ 32.774\,6(1)\,\text{GHz} \\
\nu_5 &= \Delta E_{\text{FS}} + A_1 + \ B_1 + A_2 + B_2 + A_3 - B_3 = \Delta E_{\text{FS}} + \ 97.822\,5(1)\,\text{GHz} \\
\nu_6 &= \Delta E_{\text{FS}} - A_1 + 3B_1 + A_2 + B'_2 - A_3 - B'_3 = \Delta E_{\text{FS}} + 163.356\,1(4)\,\text{GHz}.
\end{aligned} \tag{3.1}$$

These frequencies contain as a main part the fine-structure interval $\Delta E_{\text{FS}} = h \cdot 680\,\text{THz}$, which could be seen as $B_0 - A_0$ in the above formalism. Independent values for this number are listed in table 2.4 (in terms of the wavelength in air), and the best precision of around 150 MHz was not sufficient as a reference if we wanted to decompose a single laser frequency into individual shifts. On top of this, our own frequency calibration would enter as a systematic source of uncertainty of around 10 MHz, cf. Sec. 3.5.1. The quadratic shift of the lower level (A_2) would appear as a constant offset and could not be isolated empirically. This, however, would not matter, because the magnitude is only 3 MHz, and it is known theoretically to 10 % accuracy.

If multiple transition frequencies are measured with a common reference, many of these issues

can be avoided by proceeding with frequency differences $\Delta_{ij} \equiv \nu_i - \nu_j$:

$$\begin{aligned}
\Delta_{61} &= -2A_1 + 6B_1 && - 2A_3 && - 2B_3' \\
\Delta_{52} &= +2A_1 + 2B_1 && + 2A_3 - 2B_3 && \\
\Delta_{62} &= && + 4B_1 - B_2 + B_2' && - B_3 - B_3' \\
\Delta_{51} &= && + 4B_1 + B_2 - B_2' && - B_3 - B_3' \\
\Delta_{54} &= +2A_1 && + 2A_3, &&
\end{aligned} \tag{3.2}$$

while the last difference is not accessible in our experiment. However, its appeal is apparent: The relatively direct determination of the ground-state g factor. The transitions 4 and 5 would apart from that be a pair of pumping and repumping excitations, which is also true for 2 and 5. Having such a pair rather than a one-way pump is necessary for a repeated measurement with the same ion sample.

Transitions 1 and 6 access the most distant $|3/2, \pm 3/2\rangle$ sub-levels as their respective upper terms, which has two advantages: They are closed transitions and thus the easiest to measure. And they are the outermost lines out of the Zeeman sextet, and thus their difference has the least relative uncertainty. If these are the only available values, we can still derive a combined linear g factor

$$\begin{aligned}
\Delta_{g'} \equiv \Delta_{61} + 0.3\,\mathrm{kHz} &= \left(3\,g_{3/2} - g_{1/2}\right)\mu_B\,B \\
&= g'\,\mu_B\,B,
\end{aligned} \tag{3.3}$$

with the definition

$$g' \equiv 3\,g_{3/2} - g_{1/2}. \tag{3.4}$$

The 0.3 kHz are the theoretically predicted contribution of the third order.

The uncertainty in the theoretical prediction of this combined g factor can be estimated as follows: The calculated effects shifting the g factors in the two respective fine-structure states, equation 2.5, are so different from each other that the uncertainties can be considered as independent [Sha15]. Then we arrive at a propagated error of

$$\delta g'_{\mathrm{th}} = \sqrt{(3\,\delta g_{3/2})^2 + (\delta g_{1/2})^2} = 9.0 \cdot 10^{-6} \tag{3.5}$$

with the individual uncertainties of $\delta g_{1/2} = 7 \cdot 10^{-7}$ and the strongly dominating $\delta g_{3/2} = 3 \cdot 10^{-6}$. The theoretical value including this error margin reads

$$g'_{\mathrm{th}} = 3.333\,198(9),$$

and the experimental test of this prediction shall be one of the first relevant results of ARTEMIS.

The average of frequencies ν_1 and ν_6 will in general be the best estimation for the fine-structure splitting, unless we can measure at variable magnetic field strength and thus estimate the quadratic

terms A_2, B_2' [1]:

$$\Sigma_{16} \equiv \nu_1 + \nu_6 = 2\,\Delta E_{\mathrm{FS}} + 2A_2 + 2B_2' \tag{3.6}$$

$$\Sigma_{\Delta E_{\mathrm{FS}}} \equiv \nu_1 + \nu_6 - 6.32(2)\,\mathrm{MHz} = 2\,\Delta E_{\mathrm{FS}} \tag{3.7}$$

If we have more than two frequency measurements, we can combine them to more advanced differences $\Delta_{ijkl\ldots} \equiv \nu_i - \nu_j + \nu_k - \nu_l \pm \ldots$ and disentangle the different contributions:

$$\begin{aligned}
\Delta_{6152} &= \Delta_{61} + \Delta_{52} = 8B_1 - 2B_3 - 2B_3' \\
\Delta_{6154} &= \Delta_{61} + \Delta_{54} = 6B_1 - 2B_3' \\
\Delta_{5126} &= \Delta_{51} - \Delta_{62} = 2B_2 - 2B_2' \\
\Delta_{52525216} &= 3\Delta_{52} - \Delta_{61} = 8A_1 + 8A_3 - 6B_3 + 2B_3'
\end{aligned} \tag{3.8}$$

$$\begin{aligned}
\Delta_{B_1} &\equiv \Delta_{6152} + 0.3\,\mathrm{kHz} = 4\,g_{3/2}\,\mu_B\,B \\
\Delta'_{B_1} &\equiv \Delta_{6154} + 0.7\,\mathrm{mHz} = 3\,g_{3/2}\,\mu_B\,B \\
\Delta_{B_2} &\equiv \Delta_{5126} + 0.157(2)\,\mathrm{MHz} = 2\,g^{(2)}_{3/2}(1/2)\,\frac{(\mu_B\,B)^2}{mc^2} \\
\Delta_{A_1} &\equiv \Delta_{52525216} - 0.3\,\mathrm{kHz} = 4\,g_{1/2}\,\mu_B\,B
\end{aligned} \tag{3.9}$$

Δ'_{B_1} would be an alternative in case ν_4 could be measured. The contained third-order term is almost six orders of magnitude smaller than the (still negligible) one in Δ_{B_1}.

3.2 Ion Motion in a Penning Trap

This section summarizes the principles of a Penning trap, which can be studied in more detail in many textbooks, e.g. [MGW05]. The trap ideally consists of a strong homogeneous magnetic field

$$\vec{B} = (0, 0, B)$$

for radial confinement of charged particles. A relatively weak electrostatic quadrupole field

$$\vec{\mathcal{E}} = \frac{U_0}{2d^2}\,(\vec{\rho} - 2\vec{z})\,, \tag{3.10}$$

or the according electrostatic potential

$$\Phi(\rho, z) = \Phi_{\mathrm{harm}}(\rho, z) \equiv \frac{U_0}{4d^2}(\rho^2 - 2z^2) \tag{3.11}$$

prevents the ions from axial escape. We use cylindrical coordinates $\vec{z} \equiv (0, 0, z)$, $\vec{\rho} \equiv (x, y, 0)$, $\rho = \sqrt{x^2 + y^2}$, while $\vec{r} = (x, y, z) = \vec{\rho} + \vec{z}$ is the Cartesian vector; the (effective) trapping voltage $U_0 < 0$ and the characteristic dimension $d = \frac{1}{2}\sqrt{{\rho_0}^2 + 2{z_0}^2}$, ρ_0 and z_0 being dimensions of the

[1] Here we can count both quadratic terms as negligible, because they are taken up by the systematic error. In contrast to the quadratic order, the cubic contribution cancels exactly here.

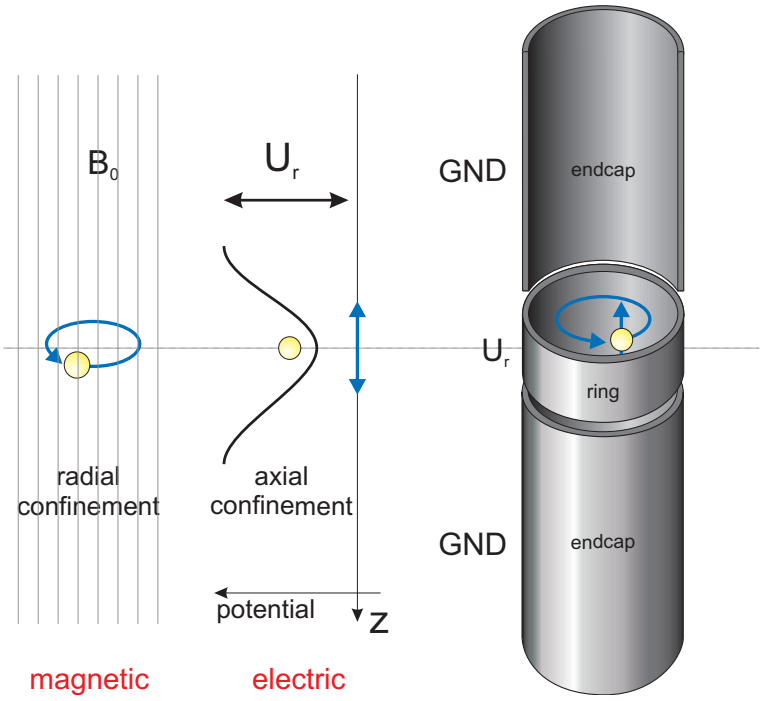

Figure 3.2: Confinement and motion in a simple Penning trap.

trap, will be further explained in section 4.3, where the shaping of such a field will be discussed. A simplified configuration and the ion motion are depicted in figure 3.2.

As mentioned before, particles confined in a Penning trap oscillate or circulate with well-defined frequencies. They are related to the free cyclotron frequency, which is used to calibrate the magnetic field. We will derive the equations of motion for an ion with (positive) charge Q and mass M, as well as their solutions, from the Lorentz force:

$$\begin{aligned} \vec{F} &= Q\left(\vec{v}\times\vec{B}+\vec{\mathcal{E}}\right) \\ = M\ddot{\vec{r}} &= QB\,\dot{\vec{r}}\times\vec{e}_z + \frac{Q|U_0|}{2d^2}\left(\vec{\rho}-2\vec{z}\right) \\ \Leftrightarrow \ddot{\vec{r}} &= \omega_c\,\dot{\vec{r}}\times\vec{e}_z + \frac{\omega_z^2}{2}\left(\vec{\rho}-2\vec{z}\right), \end{aligned} \tag{3.12}$$

with the axial and cyclotron angular frequencies ($\omega = 2\pi\nu$):

$$\omega_z \equiv \sqrt{\frac{Q|U_0|}{Md^2}} = \sqrt{\frac{2c_2QU_r}{Md^2}}. \tag{3.13}$$

$$\omega_c \equiv \frac{QB}{M}. \tag{3.14}$$

For completeness, the axial frequency is also supplied in terms of the applied ring voltage U_r, and geometry parameter c_2, see section 4.3. The independent z component reads

$$\ddot{z} = -\omega_z^2 z, \tag{3.15}$$

and describes a harmonic oscillation in z-direction with the angular frequency $\omega_z \approx 2\pi \cdot 0.83\,\mathrm{MHz}$ (values for $^{40}\mathrm{Ar}^{13+}$ in the trap that is presented in section 4.3). For the motion in the $z = 0$ plane ('radial motion'), we introduce a complex variable $\boldsymbol{\rho} \equiv x + iy$, consistent with $|\boldsymbol{\rho}| = \rho$, and the complex force $\boldsymbol{F} \equiv F_x + iF_y = M\ddot{\boldsymbol{\rho}}$. The velocity is simply the derivative of $\boldsymbol{\rho}$: $\boldsymbol{v} \equiv \dot{\boldsymbol{\rho}} = \dot{x} + i\dot{y}$. Now the vector product $\vec{v} \times \vec{B}$, with a magnetic field perpendicular to the $z = 0$ plane, can be expressed by multiplication with an imaginary number:

$$\begin{aligned} \vec{F}_{\mathrm{mag}} &= QB\,\vec{v} \times \vec{e}_z \\ \Rightarrow \boldsymbol{F}_{\mathrm{mag}} &= QB\,(\dot{y} - i\dot{x}) = QB\,(-i\boldsymbol{v}). \end{aligned}$$

Then the radial equations of motion take the form

$$\ddot{\boldsymbol{\rho}} = -i\omega_c\dot{\boldsymbol{\rho}} + \frac{\omega_z^2}{2}\boldsymbol{\rho}.$$

With the ansatz

$$\boldsymbol{\rho}(t) = \boldsymbol{\rho}_0\,\mathrm{e}^{-i\omega t}, \quad \boldsymbol{\rho}_0 \neq 0$$

they can be solved and converted to a quadratic equation for ω:

$$\begin{aligned} -\omega^2\boldsymbol{\rho} &= -\omega_c\omega\boldsymbol{\rho} + \frac{\omega_z^2}{2}\boldsymbol{\rho} \\ \Leftrightarrow 0 &= \omega^2 - \omega_c\omega + \frac{\omega_z^2}{2} \qquad (3.16) \\ \Rightarrow \omega_\pm &= \frac{\omega_c}{2} \pm \sqrt{\frac{\omega_c^2}{4} - \frac{\omega_z^2}{2}}. \qquad (3.17) \end{aligned}$$

Equation 3.16 and its solutions 3.17 can be understood from an intuitive balance-of-forces point of view: The outward-pointing inertial ($\propto \omega^2$) and electrostatic ($\propto \omega^0$) forces are balanced by the inward-directed magnetic force ($\propto \omega^1$). We assume the electrostatic term to be relatively weak: The stability condition for trapping,

$$2\sqrt{\frac{|U_0|}{2d^2}}\sqrt{\frac{M}{Q}} < B, \qquad (3.18)$$

is equivalent to the requirement that the square root in Eqn. 3.17 be real. In the given situation, this is by far satisfied, justifying the above assumption. Then, the forces can either be balanced with a rather high frequency, close to the cyclotron frequency, which is the limit for zero electric field. This solution is obtained by neglecting the constant term (and ruling out the trivial solution of $\omega^2 = \omega_c\omega$). In reality, the electric force adds to the centrifugal force. The balance can be restored by a reduced cyclotron frequency, since it affects the positive centrifugal part more strongly than the negative magnetic one. Therefore ω_+ is named the 'reduced cyclotron frequency' and for $^{40}\mathrm{Ar}^{13+}$ in 7 T it has the approximate value $2\pi \cdot 35\,\mathrm{MHz}$. The second solution is obtained with low frequency. Here we can neglect the centrifugal force and balance the electric and magnetic forces. Ions drift through the crossed electric and magnetic fields, as in a Wien filter, with a velocity

$\omega_- \cdot \rho = \mathcal{E}/B$, or

$$\omega_- \approx \frac{\omega_z^2}{2\omega_c} = \frac{|U_0|}{2d^2}\frac{1}{B}. \tag{3.19}$$

The finite centrifugal force is compensated by a slightly higher frequency, replacing ω_c in equation 3.19 by ω_+. The so-called 'magnetron frequency' amounts to $2\pi \cdot 0.01\,\mathrm{MHz}$ in our trap and is almost independent of the charge-to-mass ratio.

Stored ions can move with any linear superpositions of the three presented eigenmotions, namely the reduced cyclotron, the magnetron, and the axial motions. Thus the corresponding frequencies ω_+, ω_-, and ω_z can be measured by pickup and resonant amplification of image currents (cf. Sec.3.4). The above defined (free) cyclotron frequency is best determined by a quadratic sum,

$$\omega_c^2 = \omega_+^2 + \omega_z^2 + \omega_-^2, \tag{3.20}$$

as stated in the invariance theorem [BG82]. As the name indicates, this quantity is invariant under tilt or ellipticity of the trapping fields (or at least less sensitive to these imperfections) than the intuitive $\omega_c = \omega_+ + \omega_-$ formula. In order to match the experimental resolution of the magnetic field with the spectroscopic uncertainty of around 10^{-9} in the final stage of microwave spectroscopy, we need to determine the (reduced) cyclotron frequency with that accuracy. The axial frequency is defined by an LC circuit (section 4.6) and ions are tuned into resonance by setting the trap depth U_0. This should then be reproducible on the ppm level. The magnetron frequency needs to be determined with $7 \cdot 10^{-3}$ relative uncertainty. See section 3.5.2 for the derivation of these statements.

3.3 Axial-Frequency Shifts of an Ion Cloud

One advantage of the laser-microwave double-resonance technique over the Stern-Gerlach method is that it is performed without a magnetic bottle. The magnetic field can be as homogeneous as technically possible, which saves us from uncertainties due to the coupling of different motional degrees of freedom and related frequency shifts [VQN10].

In turn, laser spectroscopy of forbidden transitions brings up new requirements in order to enhance the low fluorescence signal to a detectable degree. Some adaptations go along with sources of uncertainty in the B-field calibration: A trap geometry favorable for efficient collection of emitted light is presented in section 4.3. A spectroscopic mesh is introduced, which might corrupt harmonicity of the trapping potential. The light is guided to a high-quantum-efficiency single-photon detector, as reported in section 4.10. Also, the ion number is increased from unity to many thousands or millions. This circumstance, together with an imperfect trapping potential, leads to perturbations of the motional frequencies, such that the equations of the previous section do no longer accurately hold. The combined effect of space charge and anharmonicity shall be estimated in this section by considering the cloud size and the amplitude-dependent shift in axial frequency of a single ion.

The Coulomb force pushes ions apart from each other, such that some ions easily reach displacements corresponding to thousands of Kelvin for single trapped ions: The ion density is restricted to a maximum value defined by the storage voltage and the charge state [YDP89]. In our trap, it

is

$$\rho_Q \leq \frac{3\varepsilon_0|U_0|}{Qd^2} \approx 2 \cdot 10^4\,\mathrm{mm}^{-3}. \tag{3.21}$$

A spherical cloud of 10^5 Ar^{13+} ions would then occupy a volume with roughly 1 mm radius. We need to be aware that a finite temperature smears out the cloud to much larger distances from the trap center. The ions are produced with electrons at keV energies, and we have no efficient way of cooling internal degrees of an ion cloud. Furthermore, without magnetron centering, ions can even orbit at large magnetron radii, which is energetically preferred even for a single particle, due to the radially outward-directed electric force (Eqn. 3.10).

In a perfect quadrupole potential as in equation 3.11, this would have no effect. Our trap (the spectroscopy trap in contrast to the less specialized creation trap—see section 4.3 for an introduction of their respective functions and shapes) was designed such that the potential on the z-axis follows as closely as possible the harmonic z^2-shape. However, in reality we have to face inaccurate manufacturing, misalignment, detuned or unstable trapping voltages. These imperfections lead to anharmonicities which shift the motional frequencies of individual particles, depending on their motional amplitudes.

The situation of a mixed cloud is even worse: Firstly, different ion species can separate radially [DO99] and therefore are subject to species-dependent radial shifts. Secondly, they oscillate at significantly different frequencies, such that each sub-cloud sees a different space-charge shift [WVST06], produced by the other species, reducing the axial frequency. In a pure cloud, individual ions move in a space-charge-modified potential, as well. But in this case, the center of charge and center of mass coincide, therefore this does not affect the observable motion of the ion cloud as a whole [BPB$^+$88].

Here we estimate the effect of an imperfect trapping potential ($\Phi(\rho, z) \neq \Phi_{\mathrm{harm}}(\rho, z)$ instead of the idealized expression 3.11) on a cloud with ions at large amplitudes, both radial (a_ρ) and axial (a_z). This is often done by perturbation theory, using the 4^{th} and 6^{th}-order coefficients of a power-series expansion for the potential and expressing frequency shifts as a function of axial energy [GHR89, VQN10]. This is not useful in the present case and would probably by far underestimate frequency shifts, for several reasons:

- Axial energy is only one cause of displacement and is in many cases negligible compared to Coulomb repulsion. A formalism which is fit for the present case should be directly applied to amplitudes.
- Our spectroscopy trap has been optimized with respect to the leading-order anharmonic coefficients (cf. Sec. 4.3). Residual imperfections would be largely made up by the 8^{th} or higher orders, which are not considered in this formalism. Neither are contributions from odd orders, because they vanish for a symmetric trap, but presumably not for ours.
- Radial amplitude has proven to contribute strongly to frequency shifts, but is likewise neglected in [GHR89]. The radial spread of an ion cloud is substantially lower while applying a rotating-wall to trap electrodes [BVST12, BHM$^+$93], which is foreseen for the spectroscopy trap.

Hence, a more general approach is chosen, calculating the axial-frequency shift numerically for a single ion in either of the two traps belonging to the present experiment. The calculation has been

done with the best available expressions for the potentials $\Phi(\rho, z)$, partially drawn in figure 3.3. A single trapped ion with amplitudes a_ρ and a_z would oscillate between turning points z_1, z_2, defined by the two conditions

$$Q\,\Phi(a_\rho, z_1) = Q\,\Phi(a_\rho, z_2),$$
$$z_1 - z_2 = 2\,a_z,$$

where the potential energy is equal to the axial energy E_z (excess over the rest energy E_0). In a 1-dimensional problem, the energy-conservation law,

$$M/2\,(\mathrm{d}z/\mathrm{d}t) + Q\,\Phi(a_\rho, z) = E_z - E_0$$

can be transformed into an integral of the elapsed time between turning points,

$$T(a_\rho, a_z) = \int_{z_2}^{z_1} \mathrm{d}z\,\sqrt{\frac{2M}{Q\,[\Phi(a_\rho, z_1) - \Phi(a_\rho, z)]}},$$

from which we can calculate the shift

$$\delta\nu_z(a_\rho, a_z) = \frac{1}{T(a_\rho, a_z)} - \frac{\omega_z}{2\pi}$$

with respect to the unperturbed axial frequency as defined in equation 3.13. The shifts are shown in figure 3.3, as well—while the potentials are plotted below the respective $\delta\nu_z(a_\rho, a_z)$ graphs with slightly higher range in order to reveal the anharmonicities more clearly.

We start the discussion with the creation trap (Fig. 3.3(b)), because it is more intuitive. At zero radius, the (always negative) shift grows up to −6.5 kHz for 4 mm amplitude. This is roughly 1 % of the axial-resonator frequency of 635 kHz, which requires −20.5 V to bring Ar^{13+} ions to resonance. The same effect is reached at a radius of around 3 mm and vanishing amplitude. At 5 mm radius the shift is even −48 kHz. These down-shifts are induced because the potential rectifies at the trap boundaries ($\rho_0 = 8.7\,\mathrm{mm}, z_0 = 7.7\,\mathrm{mm}$), which is well visible in figure 3.3(d). Only for a combination of large radius and large amplitude, ions see the potential leap between neighboring electrodes, which could in principle shift the frequency up if energetically possible.

The shifts in the spectroscopy trap (Fig. 3.3(a)) are rather moderate: On axis, the (still negative) shift is below a kHz up to 4 mm amplitude. This can be understood from the much more harmonic potential at $\rho = 0\,\mathrm{mm}$ (Fig. 3.3(c)) due to an extended trap length ($z_0 = 9.0\,\mathrm{mm}$), and the more sophisticated 5-pole trap geometry (see Sec. 4.3). Also in this trap, the orbit radius plays a more crucial role than the axial amplitude: If the a_ρ is increased to 4 mm, the frequency shift changes between +2.5 kHz in the limit of zero amplitude and a minimum of −2.3 kHz at $a_z =$ 3.6 mm. At 5 mm radius, the shift changes sign several times, depending on the axial amplitude, with absolute values of up to ±10 kHz. This is caused by the rather uneven structure seen at $\rho = 8\,\mathrm{mm}, z \approx 12\,\mathrm{mm}$, originating from the sectioning of electrodes (again at $\rho_0 = 8.7\,\mathrm{mm}$). Still, the large majority of ions will be found at smaller amplitudes. Thus the frequency spectrum won't be wider than a few kHz, which is well below 1 % of the axial frequency of 833 kHz, corresponding to a trap voltage of −50 V for Ar^{13+} ions.

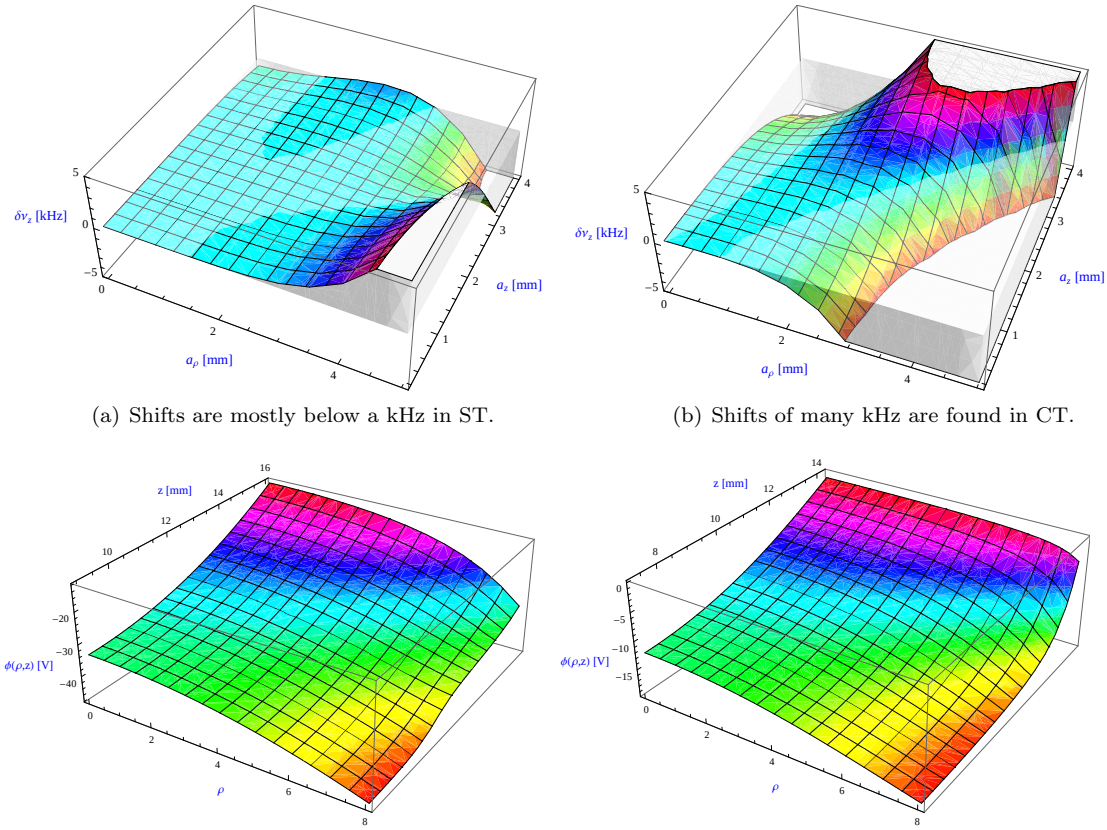

(a) Shifts are mostly below a kHz in ST.

(b) Shifts of many kHz are found in CT.

(c) Potential in a sector of ST.

(d) Potential in a sector of CT.

Figure 3.3: Plots of the axial-frequency shift for a single Ar^{13+} ion, and the electrostatic potentials in the spectroscopy (ST) and creation trap (CT), respectively. The potentials are functions of the radial (ρ) and axial coordinate (z), while the shifts are plotted as a function of radial (a_ρ) axial amplitude (a_z).

Summarizing, we can say that in both traps the shifts depend dramatically on the radial amplitude, while in the spectroscopy trap the axial frequency is much more stable than in the creation trap, which seems sufficient for the current stage of the experiment. Later, the magnetic moment will be determined more directly by microwave excitation. The enhanced accuracy in the Larmor frequency needs to be matched with a more precise cyclotron-frequency measurement. To that end, the determination of motional frequencies will require the reduction to a single particle [Lin10].

3.4 Resonant Detection of Ion Motions

Ions are detected and cooled by the technique of resonant image-current amplification in a tuned circuit [Ulm11, WD75]. Figure 3.4 shows an ion in axial motion and the main components of the resonant circuit, namely the inductance L of a dedicated coil and the capacitance C_T that naturally comes with the trap electrodes. The circuit is closed via common ground and the filter capacitance C_F, which is much larger than C_T (hence negligible) and is required to supply the

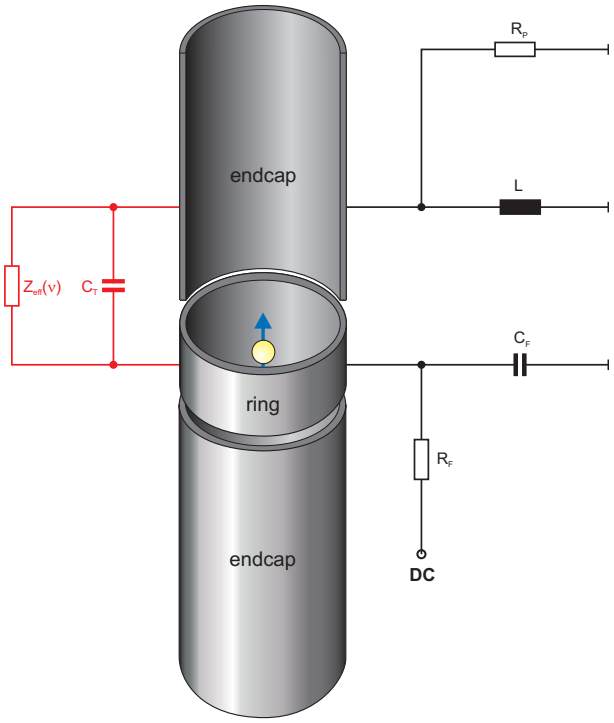

Figure 3.4: Resonant detection of stored ions.

ring with a finite DC bias.

This configuration forms a parallel LC circuit, and can be described by a total impedance $Z_{\text{eff}}(\nu)$, following a Lorentzian curve with resonance frequency

$$2\pi\,\nu_{LC} = \frac{1}{\sqrt{LC}},$$

and width

$$\Gamma_{LC} = \frac{2\pi\,\nu_{LC}^2\,L}{R_P},$$

resulting in a quality factor

$$Q_{LC} = \frac{\nu_{LC}}{\Gamma_{LC}}.$$

On resonance, L and C cancel and the impedance is limited by the inevitable parallel resistance R_P of the order of many MΩ. The parameters are matched to the oscillation frequencies of the trapped ions—values of the component used in our setup are supplied in section 4.6.

The high resonant impedance converts the image current to a synchronous voltage drop in the circuit, which is supplied at the electrode, damping the ion motion. Typical values for single particles are fA currents and nV resonant voltages. At the same time, the voltage drop is amplified and used to detect ions resonantly. The total amount of energy can be estimated from this signal and assigned to ions with a particular motion frequency—axial (Eqn. 3.10) or cyclotron (Eqn. 3.15),

depending on the configuration of the pickup electrode. The example in figure 3.4 would detect axial oscillation; if the ring is split in two halves and signal is picked up from one segment, the system will be sensitive to radial motion. A damping term adds to the equation of motion (3.12) and leads to a cooling time constant of

$$\tau_1 = \frac{D^2 M}{R_P\, Q^2} \approx 1\,\mathrm{s}$$

for a single $^{40}Ar^{13+}$ ion. Q and M are the ion charge and mass, D is the effective electrode distance of a few cm.

Theoretical treatment of a composite cloud in an anharmonic trap is very cumbersome, but some estimations of the cooling behavior are made in [VHH+14], in connection with comprehensive simulations of single-species clouds [Ste15]. An ion cloud can oscillate as a whole (center of mass or charge), and there are internal (relative) motions, which are addressed with much lower efficiency. But under certain conditions (multi-species cloud, anharmonic trap), the internal degrees and also radial motion couple to the axial center-of-charge oscillation and can thus be detected and cooled by an axial resonator. The heat reservoirs in this chain are linked to each other by exchange efficiencies ('time constants'), which are not constant, but strongly depend on the ion temperature and density. With the estimations in [VHH+14], we arrive at a rate for the transfer from radial to axial, corresponding to the Spitzer self-collision time τ_T of thermalization within a plasma,

$$\tau_T \approx (4\pi\varepsilon_0)^2\, \frac{3\sqrt{M}(k_B T)^{3/2}}{4\sqrt{\pi}\rho_Q Q^4 \ln\Lambda}, \tag{3.22}$$

with $\ln\Lambda \approx 20$ being the so-called 'Coulomb logarithm'. This time constant is of the order of many seconds for a cloud of Ar^{13+}, which at a thermal energy of around a keV will presumably not reach the maximum density postulated in the previous section (Eqn. 3.21), but after a while of cooling, the efficiency will be dramatically enhanced.

Measurements of the cooling behavior in section 5.5 are consistent with this rough estimation.

The time constant for energy transfer between disordered and ordered axial motions can be estimated with the inverse of the axial resonance width, because both are due to the trap anharmonicity. With observed relative peak widths up to a few percent, this cooling time is well below a millisecond, just alike the coupling of the axial motion to the LC circuit on resonance, which is the single-particle time constant divided by the ion number.

3.5 Uncertainties

The formulas presented in the previous sections combine several directly observable quantities with each other to derive the magnetic moments of interest. Measurement errors are propagated in these calculations. The standard Gaussian formalism for a product $f(x, y) = c \cdot x \cdot y$, with constant c and uncorrelated x and y, is the quadratic sum of relative uncertainties,

$$\frac{\delta f}{f} = \sqrt{\left(\frac{\delta x}{x}\right)^2 + \left(\frac{\delta y}{y}\right)^2}. \tag{3.23}$$

All relations beyond this simple rule are explained in the following subsections, along with a quantitative estimation of the relevant uncertainties.

3.5.1 Optically Determined Zeeman Shifts

Even if the ions are cooled to the resistive limit of 4 Kelvin, Doppler broadening of resonance lines plays a significant role due to the square-root dependence on temperature [Dem93]. For the present fine-structure transition we expect a broadening (standard deviation, $\sigma = \nu\sqrt{k_B T/(Mc^2)}$) of 60 MHz, being $9 \cdot 10^{-8}$ of the fine-structure transition energy, but $5 \cdot 10^{-4}$ or $9 \cdot 10^{-4}$ of the respective Larmor frequencies.

With sufficient statistics, the center of a resonance line can be determined more precisely than this, and the actual (Doppler) uncertainty will be smaller than the linewidth. This will be the case for the closed transitions ($\delta\nu_1 = \delta\nu_6 = d_1\sigma$, $d_1 \ll 1$), while the others will presumably be harder to define ($\delta\nu_2 = \delta\nu_5 = d_2\sigma$, $d_2 \approx 1$ for the pumping visible transitions; $\delta\nu_3 = \delta\nu_4 = d_3\sigma$, $d_3 \gg 1$ for the hypothetical case of measuring invisible transitions 3 and 4).

The uncertainty of the laser frequency relative to the calibration is below a MHz and thus negligible. The systematic error of the calibration by tellurium (cf. Sec. 4.9) lines can be estimated with $\delta_{\mathrm{cal}} \approx 5\,\mathrm{MHz}$, according to long-term reproducibility studies [Vol14]. This is relevant for the determination of the fine-structure interval according to Eqn. 3.7. Frequency differences as in definitions 3.2, 3.3, 3.8, and 3.9 are however insensitive to a constant shift. When combining measured optical transition frequencies to derive energy shifts, we only need to consider multiple appearance of the Doppler uncertainty.

All except Δ_{A_1}, see Eqn. 3.9, are sums or differences of 4 independent optical frequencies, in which the absolute statistical errors are added quadratically:

$$
\begin{aligned}
(\delta\Delta_{g'})^2 &= 2\,d_1^2\sigma^2 \\
(\delta\Delta_{B_1})^2 &= 2\left(d_1^2 + d_2^2\right)\sigma^2 \\
(\delta\Delta_{B_2})^2 &= 2\left(d_1^2 + d_2^2\right)\sigma^2 + (0.002\,\mathrm{MHz})^2 \\
(\delta\Delta'_{B_1})^2 &= \left(2\,d_1^2 + d_2^2 + d_3^2\right)\sigma^2 \\
(\delta\Delta_{A_1})^2 &= 2\left(d_1^2 + (3\,d_2)^2\right)\sigma^2.
\end{aligned}
$$

In case of the sum 3.6, the calibration enters as systematic (correlated) error:

$$
(\delta\Sigma_{\Delta E_{\mathrm{FS}}})^2 = 2\,d_1^2\sigma^2 + (0.02\,\mathrm{MHz})^2 + (2\,\delta_{\mathrm{cal}})^2.
$$

3.5.2 Cyclotron Frequency

The partial derivatives of a squared sum of the form

$$
x^2 = \sum_i x_i^2
$$

as in equation 3.20 are

$$\begin{aligned}\frac{\partial x}{\partial x_i} &= \frac{\partial x}{\partial (x^2)} \frac{\partial (x^2)}{\partial (x_i^2)} \frac{\partial (x_i^2)}{\partial x_i} \\ &= \frac{1}{2x} \cdot 1 \cdot 2x_i = \frac{x_i}{x}.\end{aligned}$$

Since the cyclotron frequency of around 35 MHz is almost identical to the reduced one, the derivative is practically 1. With the axial and magnetron frequencies being 0.83 and 0.01 MHz, respectively, we find the uncertainty of the free cyclotron frequency to be

$$\begin{aligned}(\delta\nu_c)^2 &= \sum_{i=+,z,-} \left(\frac{\partial \nu_c}{\partial \nu_i} \delta\nu_i \right)^2 \\ &\approx (\delta\nu_+)^2 + (0.024\,\delta\nu_z)^2 + (0.000\,3\,\delta\nu_-)^2. \end{aligned} \tag{3.24}$$

For a resolution of the free cyclotron frequency of $10^{-9}\nu_c = 35\,\text{mHz}$, all terms in this sum should be below $(35\,\text{mHz})^2/3 = (20\,\text{mHz})^2$, directly translating to a maximum allowed uncertainty of 20 mHz in the reduced cyclotron measurement.

The resulting $\delta\nu_z = 0.8\,\text{Hz}$ correspond to $1 \cdot 10^{-6}$ of the axial resonance frequency, determined by the resonator attached to the spectroscopy trap (cf. Sec. 4.6). The square-root relation $\nu_z \propto \sqrt{|U_r|}$ (Eqn. 3.13) reduces the relative voltage error to half the size for the relative frequency uncertainty. The Ar^{13+} resonance in the voltage spectra appears at $-50\,\text{V}$, in which $2 \cdot 10^{-6}$ relative width translate to 0.1 mV. The magnetron frequency should be determined with 70 Hz or $7 \cdot 10^{-3}$ relative uncertainty.

Chapter 4

The Apparatus

– Overview and Commissioning –

The measurement is carried out with Ar^{13+} ions produced and stored in a cryogenic Penning trap. After creation by electron-impact ionization of argon gas inside a creation trap (CT), the ion cloud is cooled and transported into a spectroscopy trap (ST). There it is illuminated with laser and microwave radiation—subsequently emitted fluorescence light is monitored with a single-photon-counting detector. Furthermore, the magnetic field is measured via the ion motions. Chapter 5 reports how these steps are performed in our composite apparatus. The present chapter gives an overview of the experimental setup as depicted in figure 4.1 and presents the single components with some benchmark tests. Some of the instruments were already mentioned in [Lin10], but have undergone substantial development.

The core of the experiment consists of a chamber with the two traps (Sec. 4.3) and the electron source (Sec. 4.4) inside, as well as a gas injection system attached below (Sec. 4.5). The cryogenic electronics, namely two printed circuit boards for low-pass filtering (Sec. 4.7) and three resonator coils with amplifiers for cooling and resonant detection of ions (Sec. 4.6), are found above the chamber, next to the imaging optics (Sec. 4.10). All electromagnetic signals from DC to visible light enter and leave the trap chamber through the UMF ('Unterer Montage-Flansch', German for 'lower mounting flange', aka 'pinbase') by electrical vacuum feedthroughs and a spectroscopy window (Sec. 4.2). The description of these components will be followed by a wiring diagram (Sec. 4.8).

This core is assembled as a lengthy column within a cryostat, suspended from a cryocooler (Sec. 4.2) and hosted inside the warm bore of a superconducting magnet (Sec. 4.1). Outside the magnet chamber there are more components of the gas injection system, and furthermore vacuum pumps, the optical detector, room-temperature filtering and amplification electronics, several highly stable voltage supplies, RF synthesizers, a spectrum analyzer, signal multiplexers, a fail-safe system ('watchdog') and the master control PC. The laser system with a slave PC is set up in an air-conditioned lab and connected with the experiment via a 27 meter long glass fiber (Sec. 4.9).

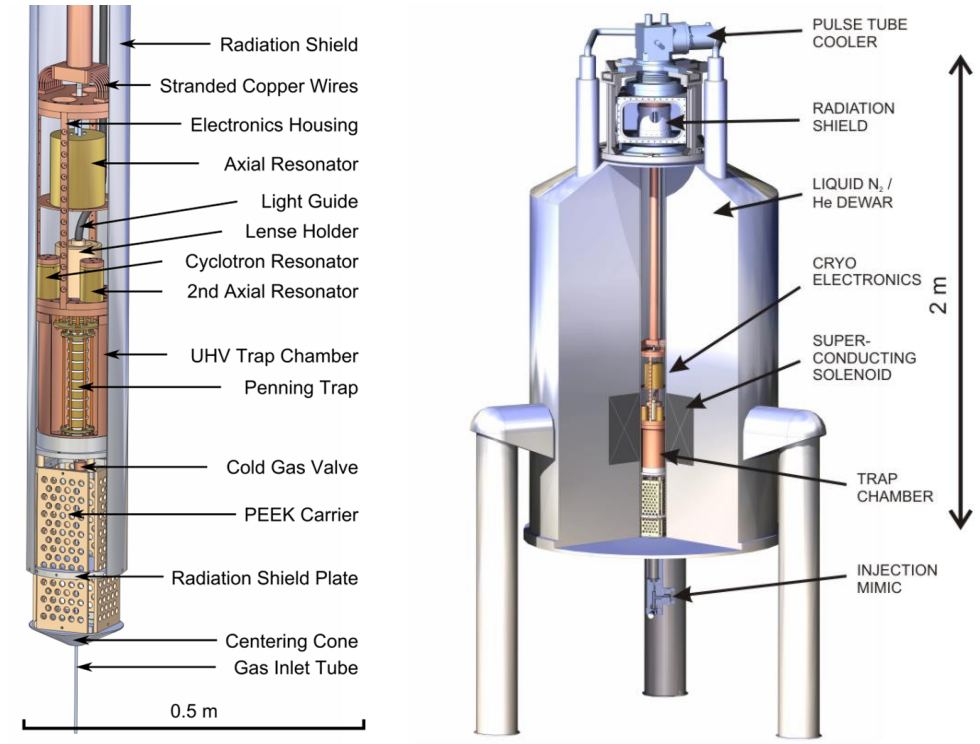

(a) Experimental core, with radiation shield and trap chamber cut open.

(b) Section through the experimental apparatus.

Figure 4.1: Overview pictures of the experimental setup, with length scale.

4.1 The Magnet and Outer Vacuum Chamber

The magnet system VARIAN 7T160 is built around a principal persistent-mode solenoid, immersed in liquid helium to ensure a temperature of 4 Kelvin. The helium and a surrounding liquid-nitrogen container are evacuated-double-wall dewars, minimizing the heat load and thus helium consumption. The magnet is a ready-made system, which has been set up, energized and optimized initially by the company in 2009. The value of 7.003 T could be reproduced three years later. It has a vertical room-temperature bore of 160 mm diameter and 1730 mm length, which allows independent modification and cooling of the experiment column.

The design stability of the magnetic field is better than 1 ppm/h. The specified field homogeneity is better than 0.1 ppm over a 1 cm^3 cubic volume. Furthermore, around this magnetic field center is a larger cylindrical volume with 0.5 cm diameter and 10 cm length over which the specified field homogeneity is smaller than 10 ppm. This is attained by active and passive shielding. A set of superconducting shim coils have been tuned to reduce field distortions, and small amounts of ferromagnetic material has been brought inside the warm bore for further adjustment. On the outside the field strength drops soon, such that at most places it is below 50 G, (cf. App. A). The liquid helium dewar holds 300 liters for around 10 months and the exhaust is attached to a recovery system at GSI for compression and reliquification.

The magnet bore is used as an insulating vacuum chamber for minimizing thermal and gas load to the cooled inner components. To this end it is closed with a lower flange that features

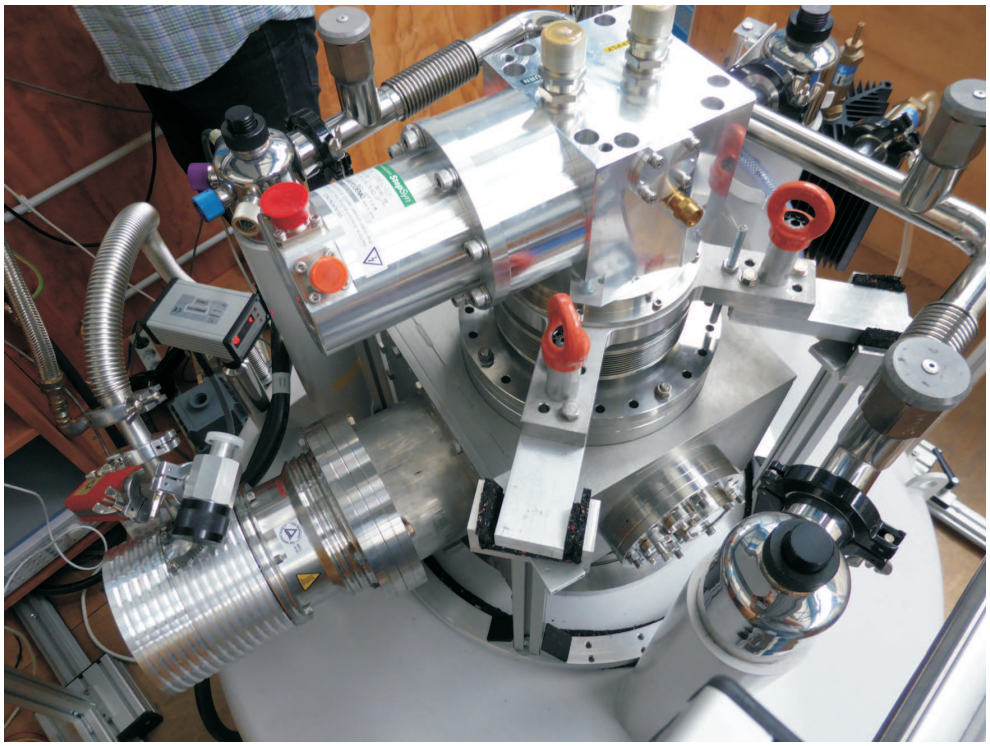

Figure 4.2: Photograph of the magnet hat with turbo pump, cryocooler, and optics flange.

an EDWARDS AIGX active ion gauge and an O-ring sealed compression port with a stainless-steel tube for gas injection. The injection system will be discussed in section 4.5 and chapter 5.3.

On the upper side of the magnet bore, there is a cuboid 'hat' vacuum chamber (Fig. 4.2), which has standard CF flanges that feature all in- and outgoing connections between the experimental core and the peripheral instruments. Two faces feature electrical feedthroughs (cf. Sec. 4.8), another one for optics (Sec. 4.10) and—at a later stage—microwaves. A LEYBOLD Mag W 400 P turbomolecular pump is attached on the last side. The pump is backed with an EDWARDS RV12 pump and monitored with an EDWARDS APG active Pirani vacuum gauge.

A pulse-tube cryocooler is positioned on top of this box. It is supported by the magnet via rods and a vibration-damping rubber layer—the vacuum connection to the hat is implemented with flexible bellows. This construction is made for the purpose of reducing the propagation of vibrations from the cryocooler to the trap, as described in section 4.2. All junctions of the magnet vacuum are welded or rubber sealed.

4.2 The Cryogenic System and Core Electronics

The experiment column is cooled by a SUMITOMO SRP-082B-F-70H pulse-tube cryocooler (cold head, synonymously). F-70H stands for the water-cooled compressor (7 kW power consumption). These components form a closed system of helium gas at a pressure around 20 to 24 bar in the supply line and 16 bar in the return line.

Cooling to liquid-helium temperature has several advantages over a room-temperature setting:

Ions in thermal equilibrium with the system have lower motional amplitudes, which renders motional and optical frequencies more precise. Ions live longer due to the excellent vacuum, which is reached without further effort. Electronic noise of amplifiers is reduced and coil wires get superconducting, such that low-energy ions can be detected.

The cold head has two cold stages. The first stage at around 30 to 45 K is capable of 40 W cooling power and is used to pre-cool most electrical DC connections as well as an aluminum shield for protection against 300 K black-body radiation. Thus it minimizes thermal load to the second stage. The shield has an inner diameter of 146 mm and surrounds most of the inner parts. Like some other components it is covered with a multi-layer (RUAG 'Cryogenic Insulation Coolcat') foil of aluminum-coated Mylar with meshed spacers between layers. The high reflectivity and multiplicity of this element has a high insulating impact.

The second stage at around 4 Kelvin cools a 705 mm long OFHC (Oxygen-free high thermal conductivity) copper rod with 1 W of cooling power. The rod is connected to the cryogenic electronics ('4-leg') housing and trap chamber via stranded copper wires for vibrational decoupling. The trap chamber rests on a centering cone for accurate alignment with the lower magnet flange and a pedestal of four PEEK (polyether ether ketone) boards for thermal insulation [Wie12]. Thus, we can ensure that the cryogenic parts are thermally well connected to the cold head, while mechanically they hold on to the silent magnet. Farther above, the cold head is carried by a support construction with rubber granulate building protection mats, reducing propagation of any vibrations to the magnet (Fig. 4.2). The fully assembled core is depicted in figure 4.3, where also the vacuum part of the optical fiber (in blue) and the image guide (in black) are seen. Several other figures of this chapter show the core from different perspectives.

The electronics housing has been designed for efficient cooling and allowing space for the core parts. A frame with four legs (hence the name '4-leg housing') and two rings carries the lens mount, HV filter board, RF resonators, and several cable coolers (cf. explanations in Sec. 4.8). An additional half leg is attached to the lower ring for holding the LV filter close to the LV feedthroughs of the UMF. Both filter boards are backed by a copper plate, distributing the low temperature to the entire board via APIEZON N grease and a layer of Kapton foil. The 4-leg housing is made from OFHC copper with a cross section of at least 144 mm^2 for thermal conduction to the lower-lying trap chamber.

The trap chamber is found below the 4-leg housing. It consists of the UMF and a hollow cylinder, made from OFHC copper. The flange features five high-voltage and twenty low-voltage ceramic-insulated electric feedthroughs to the trap electrodes, and a quartz window for optical access to the spectroscopy trap. It also serves as definition for all GND levels (cf. Sec. 4.8). Furthermore, the electrode tower is assembled and mounted to the UMF while this is turned upside down (Sec. 4.3).

We use carbon ceramic (TMi-CCS) resistors to monitor the temperatures in several places. The resistors are squeezed into small copper boxes with indium foil and APIEZON N grease. The boxes are mounted to the following four components: an oven for gas injection (resistor without box, cf. Sec. 4.5, Chn. A, for wiring cf. Sec. 4.8); the pre-cooling terminal of the first stage (Chn. B); the axial resonator attached to creation trap (cf. Sec. 4.6, Chn. C); and the 4-leg housing (Chn. D). They are wired with pre-cooled constantan cables and read out by a KEITHLEY 2700 multimeter (with KEITHLEY 7700 multiplexer), with a 4-point resistance measurement. The

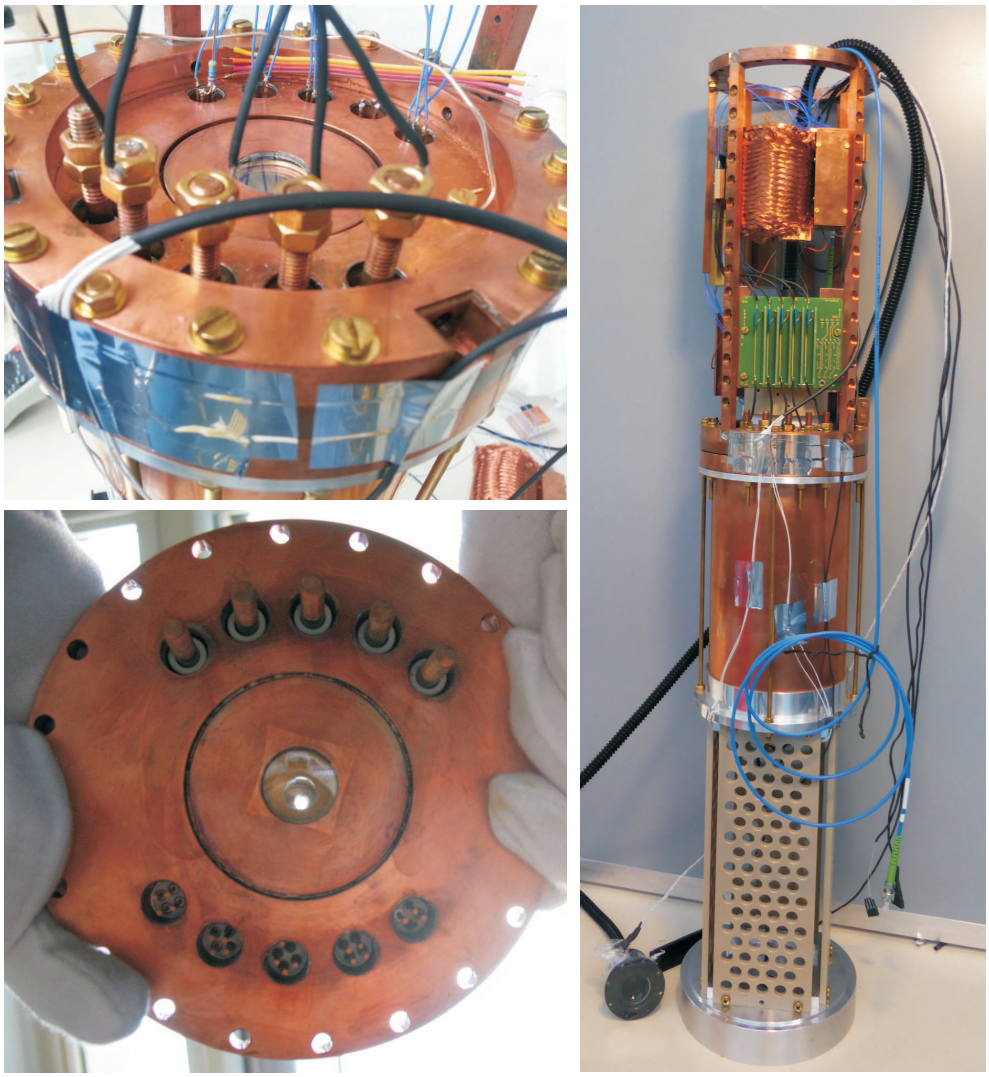

Figure 4.3: Photographs of the UMF with some of the wiring (upper left) and viewing through the quartz window, spectroscopy mesh and and trap tower (lower left) and of the fully assembled experiment core (right).

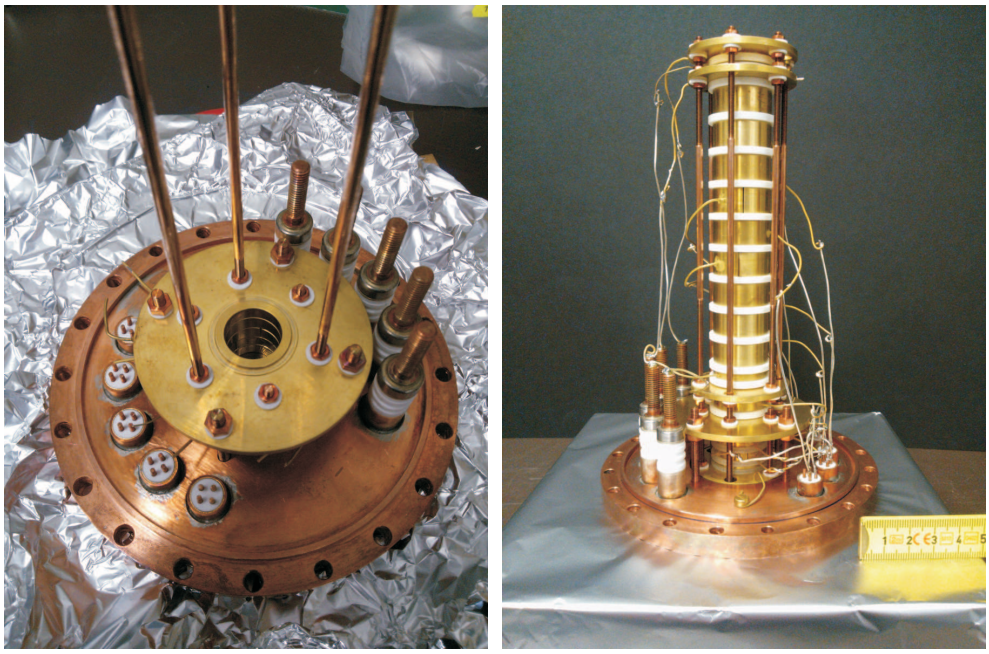

Figure 4.4: Photographs of the trap assembly. On the left, only the ST has been mounted to the UMF. On the right, the second part (the CT and the electron source) have been joined and all electrodes have been soldered to the feedthroughs. During mounting, the trap is oriented upside down.

resistance values are roughly inverse with temperature and vary between 4 kΩ at 4 K, 1.4 kΩ at 77 K, and 1 kΩ at 300 K. These sensors are routinely monitored during an experiment. Upon evacuation below of the magnet 10^{-4} mbar the cold head cools the entire apparatus to the design temperatures within roughly a day, while the system takes several days to warm up passively. At cryogenic temperature, the pressure is much lower (cryo-pumping, 10^{-6} mbar measured at a remote port of the magnet).

4.3 Two Penning Traps

The ions are produced and stored in dedicated regions of the inner vacuum chamber, which are denoted as spectroscopy trap (ST) and creation trap (CT). This section explains the purpose, design, performance and in some aspects the operation of the respective traps, and their voltage supplies. The electrodes for both traps have been made from OFHC copper, soldered with connector wires, and galvanically plated with a 20 μm thick diffusion barrier of silver and a layer of less than a micrometer of gold for protection against oxidation and smaller surface patches, which would cut measurement accuracy. Figure 4.4 presents photographs of the trap assembly with open chamber. The left part is a view into the spectroscopy trap. The right shows S1 grounded (wire bolted to the UMF), which is currently not the case. It has been connected to a feedthrough and soft-grounded on the outside (cf. Sec. 4.8). Figure 4.5 explains the nomenclature of electrodes. Among the engraved numbers, S stands for 'spectroscopy trap', T for 'transport electrode', H for 'high-voltage electrode', C for 'creation trap' (next subsection), and F for 'field-emission electron

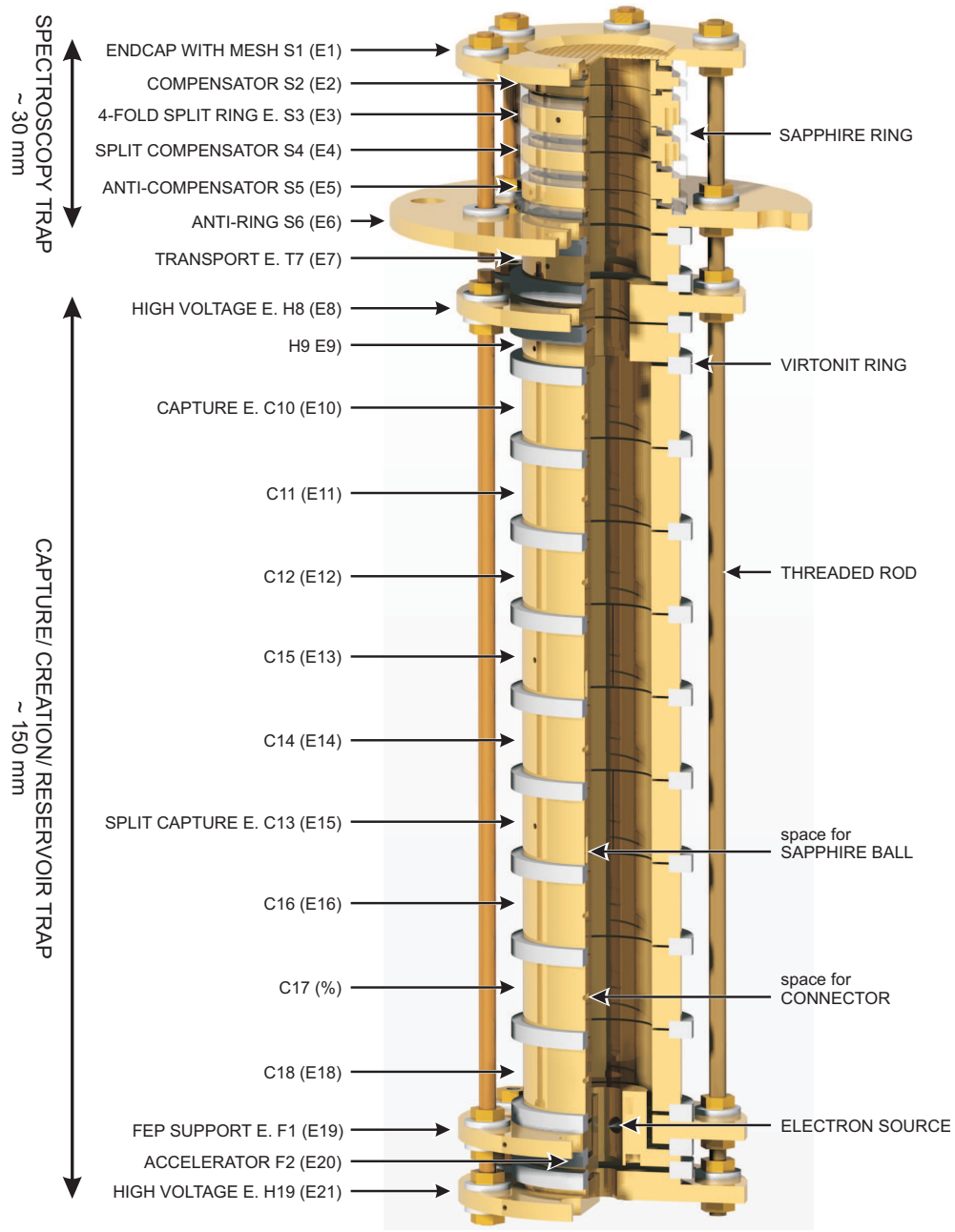

Figure 4.5: Cut drawing of the complete electrode stack with function names, engraved (S, T, H, C, F) and systematic (E) numbers of electrodes. For historic reasons these are not identical.

source' (section 4.4). C13 and C15 have been exchanged because we wanted a split electrode below the trap center C14, and C13 was more suitable for that purpose. The electron source was added to the design later. C17 does not have its own supply, but is connected to C11. For these reasons we have introduced a coherent system of E numbers (only after engraving).

4.3.1 Spectroscopy Trap

The actual measurement takes place in the spectroscopy trap, which was designed to satisfy ambitious demands: On the one hand, the laser-spectroscopic scheme requires optical excitation of the fine-structure transition and efficient collection of fluorescence light emitted by the subsequent decay. The optical detection system should be close to the trapped ions and cover a large solid angle. Simultaneously, the large ion cloud must be stored under stable and well-defined conditions—particularly the calibration of the magnetic field demands for a harmonic electrostatic potential. As discussed in section 3.3, this makes the oscillation frequencies independent of the amplitudes. To this end, the trap should be highly symmetric—in the best case, it consists of conducting hyperboloids, following the equipotential surfaces of the idealized quadrupole potential Φ_{harm}, as defined in equation 3.11. But this configuration doesn't allow fluorescence detection, and is undesirable for several other practical reasons [GM84]. Most modern-day precision Penning traps are cylindrical, maintaining rotational symmetry about the z axis (ideally aligned with the direction of the homogeneous magnetic field) and inversion symmetry about the $z = 0$ plane. If the geometry of the electrodes and the voltages are carefully chosen, machined, and supplied, the transition to the cylindrical shape is no limitation of accuracy. Furthermore, ions need to be injected into the trap. An opening for this purpose finally breaks the symmetry of the closed cylindrical trap. A fourth specification is the electronic detection efficiency, which limits the overall size.

Feasibility of combining these requirements in a half-open cylindrical trap has been demonstrated in [Lin10, LVQ$^+$14]. The design is derived from the concept of an orthogonal electrically compensated (5-pole) closed cylindrical Penning trap as presented in [GM84] and depicted in the left part of figure 4.6. This kind has a ring electrode between two compensation electrodes, which are hollow cylinders with the constant inner radius ρ_0 and lengths of $z_r \approx z_c \approx 0.6\,\rho_0$. It is closed by two flat endcaps, each at distance z_0 from the center. The endcaps are kept at ground potential, the ring at $U_r < 0$, the compensators are slightly reduced to the voltage TU_r, with a tuning ratio T of around 0.8.

In the present case, the upper endcap is realized as a flat mesh with 60 % optical transmission. The lower one is replaced by further hollow cylinders, painted in gold in the right part of figure 4.6. If these were copies of the 3 hollow cylinders together with another endcap below, and if they were supplied with voltages at the opposite sign of the original ones (hence the name 'anti-trap'), they would by symmetry ensure a plane with zero potential in the place of the missing lower endcap and thus maintain the original potential shape.

For the actual design, the optimization of the closed compensated Penning trap [GM84] was re-evaluated with a semi-analytical method. To that end, the potential for a given configuration of electrodes is calculated analytically and expanded as a (Taylor) power series for the axial coordinate z about the trap center at z_0 (the upper endcap is defined as $z = 0$ and the axis points

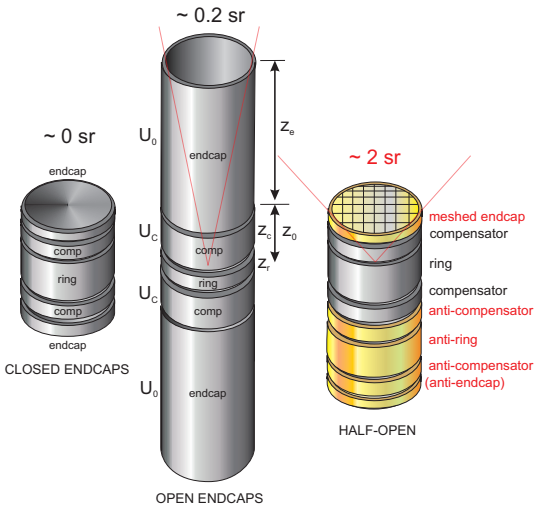

Figure 4.6: Schematic drawings of closed, open, and half-open traps, with approximative specifications of the respective solid angle available for spectroscopy.

downwards). If the ring electrode is supplied with a voltage U_r and the rest is grounded, the potential on axis is

$$\Phi^{(\mathrm{Ring})}(0,z) = U_r \sum_{j\geq 0} e_j \left(\frac{z-z_0}{d}\right)^j .$$

The characteristic dimension of the trap, $d \equiv \frac{1}{2}\sqrt{{\rho_0}^2 + 2{z_0}^2}$, is used to define dimensionless expansion coefficients. Mind that for a symmetric trap and biasing, the sum contains only even terms. If instead the compensators are kept at TU_r, the potential reads

$$\Phi^{(\mathrm{Compensators})}(0,z) = TU_r \sum_{j\geq 0} d_j \left(\frac{z-z_0}{d}\right)^j .$$

The potential of a fully supplied closed trap is a linear combination,

$$\Phi^{(\mathrm{closed})}(0,z) = U_r \sum_{j\geq 0} c_j \left(\frac{z-z_0}{d}\right)^j$$

with composed coefficients $c_j = e_j + Td_j$. The harmonic potential of equation 3.11 would be reproduced with $U_r = U_0$, $c_2 = -0.5$ and all other coefficients zero.

The e_j and d_j coefficients depend on the geometry only, while c_j contains the tuning ratio of voltages. This means that for a given geometry, the leading-order anharmonicity, c_4, can be tuned out by applying $T = -e_4/d_4$, which is referred to as 'electric compensation'. If the dimensions are chosen properly, the next order (c_6) vanishes simultaneously. As mentioned before, the main goal is stability of the axial frequency. It should in particular also be independent of the tuning, which is achieved by a vanishing d_2, the so-called 'orthogonality condition'. For a given trap length $2\,z_0$, the length z_r of the ring electrode and the radius ρ_0 are chosen to satisfy these conditions. This design is fixed as the 'closed trap'.

In the next step, the lower endcap is removed and additional electrodes are introduced below.

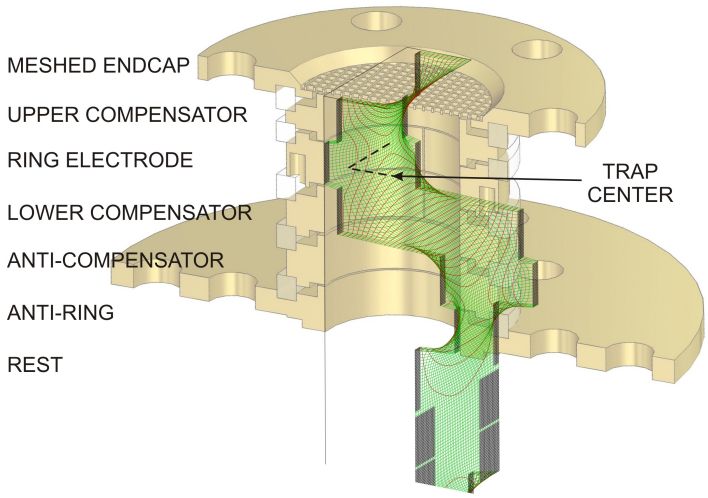

Figure 4.7: Cut drawing of the asymmetric trap with function names of electrodes. Simulation of the potential overlaid. The trap center is marked: geometrical position in the cutting plane (tip of arrow) and place in the potential (upper end of dashed line), which is not identical, due to the perspective and potential coordinate.

The starting point is the 'anti-compensator' next to the lower compensator and with inverted voltage, following the idea of an 'anti-trap'. This idea cannot be fully realized because also the extension needs to be open on the lower side. For compensation of this modification, the lengths (z_{ac}) of this electrode and of the next one, the 'anti-ring' (z_{ar}), as well as the anti-ring tuning and the bias of the less important 'rest' (generalized remaining electrodes) needed to be revised. These are determined by a fitting method with the condition of zero potential in the former place of the endcap. The additional electrodes still mimic a grounded endcap and thus a closed trap. The calculations have been discussed in great detail in [Lin10, LVQ$^+$14][1].

The resulting geometry is plotted in figure 4.7, overlaid with a SIMION calculation of the trapping potential. Numerical results are presented in the following tables. Table 4.1 presents two versions of the geometry—"theor." is the result of the above indicated semi-analytical calculations for the closed trap and of the fit method for the asymmetric trap, as found with WOLFRAM Mathematica. "prod." are the values used for the technical drawings, with 20 μm silver added and shrunk by a thermal contraction factor 0.9967. The anti-ring S5 has been ordered a little too long, which was caused by a confusion about the gap size z_g. Obviously a finite gap is needed between

[1] However, with two mistakes: Equation 5.7 of [Lin10], which is equation 10 of [LVQ$^+$14], should read:

$$a_n^{(a,b)} = \frac{2}{n\pi}\left[\cos\left(\frac{n\pi a}{z_t}\right) - \cos\left(\frac{n\pi b}{z_t}\right)\right]\sin\left(\frac{n\pi z_g}{2z_t}\right)\frac{2z_t}{n\pi z_g}$$

instead of

$$a_n^{(a,b)} = \frac{4}{n\pi}\left[\cos\left(\frac{n\pi a}{z_t}\right) - \cos\left(\frac{n\pi b}{z_t}\right)\right]\sin\left(\frac{n\pi z_g}{z_t}\right)\frac{z_t}{n\pi z_g}.$$

It was incorrectly copied from the Mathematica code. Furthermore, the explanation before the equation contains a misleading didactic reduction. This can be avoided by the wording: "... For an electrode between $z = a$ and $z = b$ (more precisely: with gaps symmetric about $z = a$ and $z = b$) at unit voltage, ..."

Table 4.1: Dimensions of the ST electrodes, in mm. Further explanations are found in the text.

Version	z_0	ρ_0	d	z_g	z_{S3}	$z_{S2} = z_{S4}$	z_{S5}	z_{S6}
theor.	9.000	8.713	7.712	0.200	5.392	5.904	6.000	5.640
prod.	8.985	8.728	7.707	0.200	5.382	5.893	6.219	5.730

Table 4.2: Tuning ratios for the ST electrodes. Further explanations are found in the text.

Version	T_{S2}	T_{S4}	T_{S5}	T_{S6}	T_{T7}
theor.	0.7994	0.7994	−0.7994	−1.0207	−0.4025
start	0.8000	0.8000	−0.8000	−1.0200	−0.4000
exact	0.8010	0.8042	−1.1786	17.859	−68.97
least	0.8056	0.8184	−1.9880	56.11	−207.14

adjacent electrodes and we have chosen 0.2 mm. Now for symmetry reasons the gap between S4 and S5 is twice the usual value, which was not consequently taken care of in fixing the dimensions for machining the trap.

Some versions of tuning are found in table 4.2. Electrode Sn is to be supplied with $T_{Sn} \cdot U_r$, and by definition $T_{S3} = 1$. "theor." is the result of the semi-analytical calculations for the closed trap and of the fit method for the asymmetric trap, going along with the "theor." geometry of table 4.1. T_{S2} and T_{S4} are identical—they represent the tuning T of the closed trap. T_{S5} is the anti-compensator voltage and is chosen opposite to T. The voltages of the anti-ring (T_{S6}) and the rest (T_{S7}) are determined by the fit, but are of minor importance. "start" is the tuning used in the current experiment as a first test. The latter two versions have been determined with Mathematica and the "prod." geometry of table 4.1. "exact" solves the linear system of equations for the coefficients c_1 and c_3 through c_6 to vanish. "least" is an optimization for the least square sum of coefficients c_1 and c_3 through c_{10}. The large deviation in the additional tunings ((T_{S6}) and (T_{S7})) is not due to the discrepancy in length of the additional electrodes (z_{S5} and z_{S6})—a test calculation with lengths closer to the theoretical value did not change the tunings much. Apparently the optimization algorithms try to improve the situation in the closed trap, rather than maintaining it, which was the guiding idea of the original introduction by a fit algorithm. This is confirmed by the following observations about the c_j coefficients.

The potential shape obtained by the different tuning options of table 4.2 can be estimated with the Taylor coefficients listed in table 4.3. For small values, $10^{n-1} < |c_j| < 10^n$ is abbreviated with 10^n, while in many cases the value is even close to $\pm 10^{n-1}$. "th. × th." is the "theor." dimensions of table 4.1 with "theor." tunings of table 4.2 and therefore reproduces the design conditions of the trap. "th. × pr." applies the "theor." tunings to the actually machined trap ("prod." of table 4.1). "start", "exact", and "least" result from the respective tunings with the "prod." geometry.

The results reflect the guidelines for designing the trap: The two leading-order even anharmonicities c_4 and c_6 were required to vanish; symmetry (odd coefficients) was guaranteed by the symmetric shape of the closed trap, while the additional electrodes were introduced to maintain the original potential. c_8 is the lowest order that is not affected by these requirements—and it

Table 4.3: Coefficients for the Taylor expansion (Eqn. 4.1) of the potential in the half-open trap. Further explanations are found in the text.

Version	c_1	c_2	c_3	c_4	c_5	c_6	c_7	c_8	c_9	c_{10}
th. × th.	10^{-6}	−0.5226	10^{-6}	10^{-6}	10^{-7}	10^{-4}	10^{-8}	0.02	10^{-8}	10^{-2}
th. × pr.	10^{-3}	−0.5229	10^{-4}	10^{-3}	10^{-4}	10^{-3}	10^{-7}	0.02	10^{-4}	10^{-2}
start	10^{-3}	−0.5229	10^{-4}	10^{-3}	10^{-4}	10^{-3}	10^{-7}	0.02	10^{-4}	10^{-2}
exact	0	−0.5231	0	0	0	0	10^{-2}	0.02	10^{-2}	10^{-2}
least	10^{-4}	−0.5237	10^{-3}	10^{-2}	10^{-2}	10^{-3}	10^{-2}	0.01	10^{-2}	10^{-2}

is very interesting to see that in all cases this is in fact larger than the other coefficients. All other versions than the design one ("th. × th.") are worse than that in most expansion orders. This shows that even the best tuning cannot fully compensate a suboptimal geometry. Still most results are quite acceptable, even with the rounded tuning values ("start"). The frequency shifts presented in section 3.3 were calculated for this set of parameters. It maintains a potential even better than "least", where a lot of quality is sacrificed for a small reduction in c_8. The "exact" solution achieves its aim: the specified coefficients are around 10^{-14} or below—which is almost zero within machine precision. But again, this comes at a price, namely the relatively high values of c_7 through c_{10}.

There are several reasons why the aforementioned results are only approximations to the real situation in the trap and should therefore not be overestimated:

- The analytic treatment of the boundary-value problem requires a constant radius. All calculations for the asymmetric trap were done with the assumption of a cylindric trap volume with 72 mm. In the final design, the stack of electrodes with uniform radius (S2 through T7) is only around 40 mm long and is continued with the narrower high-voltage electrodes (see Fig. 4.5), which are kept at ground.

- The high-voltage electrodes might however even improve the situation, because the geometry now resembles the ideal of an anti-trap more closely, having the HV electrodes as lower endcap.

- Machining accuracy is always an issue. Even though the comparison shows that the solutions are relatively stable with respect to small deviations. A deformation of the mesh is more likely to modify the trapping potential, but it cannot be studied within the present framework, see the discussion in [Lin10]. After detecting a deformation we have tried to render the mesh more even, but this will still not be perfect. A promising solution using another quartz window with a conductive indium-tin-oxide (ITO) layer is currently under investigation.

- Deviations from the ideal geometry at far distance from the trap center have only very weak effect. The potential is screened with a factor of roughly

$$\left|\frac{\partial\Phi(0,z_0)}{\partial U(z)}\right| \lessapprox \exp\left(-\pi\,\frac{|z-z_0|}{\sqrt{2}\rho_0}\right), \tag{4.1}$$

  which is approximately $4\cdot10^{-4}$ in case of the lower endcaps. The aforementioned test of

stability (done with S5/6) hence is not too significant; on the other hand, the tuning of remote electrodes is of less importance (vice versa, the optimization can easily produce exorbitant numbers for these parameters). Last, the precise shape of the lower endcap or "rest", is also not so crucial for a good potential shape.

- The coefficients were calculated at the geometric trap center $z = z_0$, while a finite c_1 shifts the actual position of the minimum, where the local c_1 vanishes, and also other coefficients might have different local values. The effect of this was tested by several iterations of optimizing tunings and finding a minimum. Most coefficients were quite stable, only c_1 was reduced basically to zero.

The spectroscopy trap is supplied with a HV 200-8 device by STAHL ELECTRONICS. It has eight individually programmable bipolar channels with a range of $\pm 200\,\mathrm{V}$, and a ramp function. If this is active, an external reference voltage (U_{ref}) between 0 and 5 V needs to be supplied to the input on the rear side. The output of each channel will then be

$$U_{\mathrm{out}} = U_{\mathrm{prog}} \cdot U_{\mathrm{ref}} \,/\, 5\,\mathrm{V}, \tag{4.2}$$

if U_{prog} is the programmed voltage. Therefore, the internal reference corresponds to roughly 5 V reference, if the calibration is done well. Limited accuracy, precision and load stability of an external reference can make the internal reference mode indispensable—the instrument has been calibrated exactly for this application and the specifications (Tab. 4.4) are better than most variable references. However the external reference allows fast proportional ramping of the entire trap (fixed tunings, varying ring voltage), which is very useful for scanning the contents of the trap in a wide range of M/Q. Different ion species are brought in resonance with the tuned circuit successively and can be identified by the applied voltage, see sections 3.4 and 5.2.3. This functionality is extensively used in all measurements about ion creation, cooling, and transport and can even be part of the magnetic field calibration, see chapter 5.

For ultimate precision, there are even better supplies at hand, bought from the same company: An ultra-high precision voltage source UM 1-14-28, with low-noise (LN) option, for the three electrodes of the original trap (S2-4, ring and both compensators)—find the specifications of all voltages supplies in table 4.4. It settles quite slowly (5 s for 99.99 % of step size), which can be accelerated by choosing the 'fast mode' instead of 'ultraprecise mode'. The further electrodes are supplied with devices from the BS series. These are less stable than UM, which is allowed due to the exponential screening, equation 4.1. BS 1-8 has some channels reserved for S6, T7, and H8/9 in LV mode (see Sec. 4.8), further channels are foreseen for different load-free purposes, such as bias for a diode filter and resonance-matching of the cyclotron resonator by a capacitance diode. For S5 we have foreseen BS 34-1. The eight channels of this device are added by an analog circuit in order to reduce fluctuations by a factor of $\sqrt{8}$. All devices by STAHL ELECTRONICS are galvanically separated from the PC and receive USB commands by an opto-coupler. The UM and BS sources also have a sense GND input, to which the outputs are referenced. This GND is defined by UMF, which is also wired to the endcap mesh, S1. The connection is done via a $10\,\mathrm{M}\Omega$ resistor ('soft GND') such that the endcap can also be used as a Faraday cup (FC) for various measurements in the context of ion production (cf. Sec. 5 and 4.4). For further details of the wiring refer to section 4.8.

Table 4.4: Specifications of the voltage sources, as in [Sta13]: Absolute accuracy (calibration), output range, short-term fluctuations, programming resolution, and temperature drift. Details are found in sections 4.3, 4.4, and 4.6. HV 200-8 is similar to HV 250-8.

Device name	abs. acc.	range	fluct. (1 min)	prog. res.	temp. drift
UM 1-14-28	10 ppm	−29 V	0.04 ppm	0.03 ppm	0.5 ppm/K
BS 34-1A	15 ppm	±31 V	0.5 ppm	1 ppm	< 5 ppm/K
BS 1-8B	100 ppm	±24 V	5 ppm	20 ppm	< 10 ppm/K
HV 250-8	100 ppm	±250 V	5 ppm		< 17 ppm/K
HV-FEP		±2000 V		500 ppm	
BS 1-10 cryo	140 ppm	±5 V	2 ppm	1 ppm	5 ppm/K

The output voltage of UM is restricted to a range of $-29\,\mathrm{V} < U_r < +1\,\mathrm{V}$. Together with the currently present resonator frequency of 833 kHz, this limits the range of detectable charge states to $M/Q < 1.8\,\mathrm{u/e}$, which leaves us with protons only. With −60 V, all species down to $^{40}\mathrm{Ar}^{11+}$ can be addressed (or any $M/Q < 3.72\,\mathrm{u/e}$). Higher voltages are not recommended, because the cryo-electronics of the trap are only specified up to 50 V. Also this combination of devices has no possibility of ramping, which makes an overview measurement very hard.

With the given geometry, the trap has an opening half-angle (between a light beam and the z axis) of $\theta_{\mathrm{trap}} = \arctan(\rho_0/z_0) = 44.1°$. We use a collimating lens (cf. Sec. 4.10) with numerical aperture of $NA = \sin\theta_{\mathrm{lens}} = 0.703$, corresponding to a very similar half-angle of $\theta_{\mathrm{lens}} = 44.7°$. Currently the angle is restricted by the window in the UMF, which has 9 mm radius at a distance of 18 mm. A cone with this half-angle of $\theta_{\mathrm{window}} = 26.6°$ covers a solid angle of 0.666 sr, which is 5.3 % of 4π sr.

The directional characteristic ($I(\theta) \propto 1 + \cos^2\theta$, cf. App. B.2) of the projection changing transitions (1, 2, 5, 6) favors small angles. Therefore 7.5 % of all photons are emitted into the relatively small solid angle. With the 44.1° angle of the trap itself, the solid angle would be 1.77 sr (or 14.1 % of 4π sr), while the weighted solid angle would be 18.4 %.

4.3.2 Creation Trap

The second trap involved in this experiment has been designed for preparation of the ion cloud. In the current setup, this means creation of ions (hence the name 'creation trap', 'CT') by electron-impact ionization of injected neutral argon atoms and subsequent charge breeding. After the charge-state distribution has reached a high amount of Ar^{13+}, the cloud is cleaned by selective RF excitation of unwanted species. Finally, the pure $^{40}\mathrm{Ar}^{13+}$ cloud is resistively cooled and transported into the spectroscopy trap.

The trap can also be used as a reservoir in case of an experimental scheme that consists of laser-spectroscopic measurements with a large cloud in turn with the precise determination of motional frequencies with a small cloud or a single ion. Switching between these modes by ion transport might be faster than preparing a new ensemble every time.

Another use of this trap is fast capture of an ion bunch that is injected from an external source—such as an electron-beam ion source (EBIS) or the HITRAP facility at GSI, which is soon to be connected to ARTEMIS. It is designed to supply bunches up to 10^5 ions of bare or few-electron

Table 4.5: Dimensions of the electrodes, in mm, and coefficients for the Taylor expansion (Eqn. 4.1) of the potential in the creation trap.

z_0	ρ_0	d	z_g	c_2	c_4	c_6	c_8	c_{10}
7.241	8.728	6.727	0.200	−0.5631	0.001	0.05	−0.005	−0.004

heavy ions (up to uranium) every minute. These ions are produced in the GSI accelerator, cooled to liquid-helium temperature, and transported at a few kV of acceleration potential. Therefore, 'CT' can also be translated with 'capture trap'. In addition to resistive cooling, the methods of sympathetic cooling with electrons or laser-cooled beryllium ions are being considered for this case.

The principle behind the design of this trap is the simpler variant proposed in [GM84], namely the mechanically compensated (3-pole) closed cylindrical Penning trap. It has the same symmetry as the electrically compensated trap, but it uses only a ring electrode between two flat endcaps. The definitions of ρ_0, z_0, and U_r are the same, the compensator and tuning voltage do not exist—therefore the c_j coefficients are identical with e_j, which will be omitted. c_4 vanishes for $\rho_0 \approx 1.203\, z_0$, while this geometry simultaneously produces a near-to-maximum c_2 [GM84].

We chose $\rho_0 = 8.73\,\mathrm{mm}$ as in ST and $z_0 = 7.24\,\mathrm{mm}$, which satisfies the compensation condition quite well ($\rho_0 = 1.205 z_0$). Further parameters are found in table 4.5. A ring voltage of $-20.5\,\mathrm{V}$ is required for $^{40}\mathrm{Ar}^{13+}$ ions to oscillate axially with the resonator frequency 635 kHz.

Just like in the case of the spectroscopy trap, the endcaps need to give way for ion transport. Again, the potential can be conserved by replacing a grounded endcap with a mirror trap. In this case it would be an 'anti-ring' at the opposite voltage of the ring electrode and a grounded endcap behind that anti-ring. The full gap is then again $2\, z_g$ long. This principle can be infinitely repeated with alternating voltages. We extended the trap to nine identical copies of the ring electrode, see figure 4.5.

With this geometry, no electrical tuning of the anharmonicities is needed, which makes the commissioning easier. On top of that, the relatively long single electrodes of the CT can produce quite a deep axial potential well—if a single electrode is supplied with U_r and all others are grounded. This is the case during transport. The normalized voltage (identical to the c_0 coefficient[2]) for the CT electrodes as well as for H8/9 is roughly 0.8, while the axial wells of single ST electrodes are only at around 40 % of the applied voltage.

At both ends, there are high-voltage electrodes, which are currently being supplied with around $-1\,\mathrm{kV}$ and serve as source and reflector for electrons to the purpose of charge-breeding, see section 4.4. In the injection scheme they are foreseen for reflection and capture of externally produced ions and will to that end be biased with fast switchable positive HV. These deviations at the ends can be neglected in the center, again because of exponential suppression, which in this case is even below $\mathrm{e}^{-9\pi z_0/(\sqrt{2}\rho_0)} \approx 6 \cdot 10^{-8}$. The biases for the creation trap are produced by the HV 250-8, a device very similar to the HV 200-8 for ST. This one ranges to $\pm 250\,\mathrm{V}$ and has a digital $(0\,/\,5\,\mathrm{V})$

[2]This coefficient is not the one of the calculated closed trap, but of the extended one. It can be estimated from the theoretical one (0.59) by redefining $-U_r$, the voltage of the anti-rings, as ground. Then, $c_{0,\mathrm{ext}}$ is approximately $(c_{0,\mathrm{closed}} + 1)/2$.

input as selector between external and internal reference. Further details are found in section 4.8.

4.4 The Electron Source

The trap chamber comprises an electron gun (tip or field emission point, hence FEP) producing a current of a few 100 nA at an energy around 1 keV in the creation trap. The primary intention is electron-impact ionization and charge breeding, as will be discussed in section 5.4; further applications may be found in sympathetic cooling and potentially electron-impact excitation of high-lying metastable states inaccessible to laser radiation.

The electron source consists of the tip itself, attached to a support electrode F1 (= E19), which can be seen in figure 4.8(a). This entity is supplied with a potential of around −1 kV, defining the energy of the electron beam in the largest part of CT (modified by the local potential of ±0.2 kV on axis). A split accelerator electrode F2 (= E20) closely surrounds the tip and produces the accelerating field. To that end it is supplied with around +1 kV, relative to the tip. The electron source is completed by the guiding magnetic field and the confining reflectors. These are H19 (= E21) and optionally H8/9 (= E8/9), which are best seen in the overview picture 4.5. The latter can be switched to individual low-voltage inputs of a two-channel HV switch, see section 4.8.

If all reflectors are on high voltage and around 0.4 kV more negative than the tip, this is the 'reflectron' mode. Electrons get recycled many times, until space charge prevents more electrons from being accelerated out of the tip and the overflow gets consumed by the accelerator or the CT electrodes. If H8/9 are switched to LV during electron emission, the electron beam gets pushed toward CT by a small asymmetry due to the negative H19 and passes the trap once, before it gets drained by S1.

The voltage supply, HV-FEP (custom-made by Stahl electronics), features a floating positive 'Acc.' channel, referenced to the negative 'FEP' channel. The 'refl.' channel is again referenced to chassis, just as 'FEP'. By design, the negative channels are specified for down to −4 kV. Currently the instrument is however restricted to −3 kV, which is sufficient. After all, the wiring in the experimental core doesn't allow more than ±2 kV. All channels are equipped with floating nano-ampere meter and a safety current limitation to around 10 μA. Further information is listed in table 4.4.

Production and test have been reported in [Lin10]. No. 2 of the studied tips was the best. The critical voltage of 0.41 kV implies a radius of 30 nm, in contrast to the estimation of around 2 μm, derived from the conditions of production. Two explanations have been presented in order to resolve the discrepancy, one of which stating: "Particular shape: Even if the fracture produces a flat top of 2 μm diameter, the edge can be much sharper. Depending on the overall geometry in the field emission setup, this can still lead to a high electric field. In this case, any deformation would blunt such edges, thus fast etching and brittleness support this phenomenon" [Lin10, p. 56]. Both numerical conclusions and the interpretation were very well confirmed by electron microscope images taken shortly after the tests, shown in figure 4.8(c).

After several cycles of assembling, disassembling and cooling in between, the tip in use might have degraded. Therefore we have revised the functionality. We applied different combinations of FEP (values of −1.0 and −1.5 kV) and reflector voltages (values of −1.0, −1.5, and −2.0 kV). In each case, we searched the accelerator voltage which produces an FEP current of certain values,

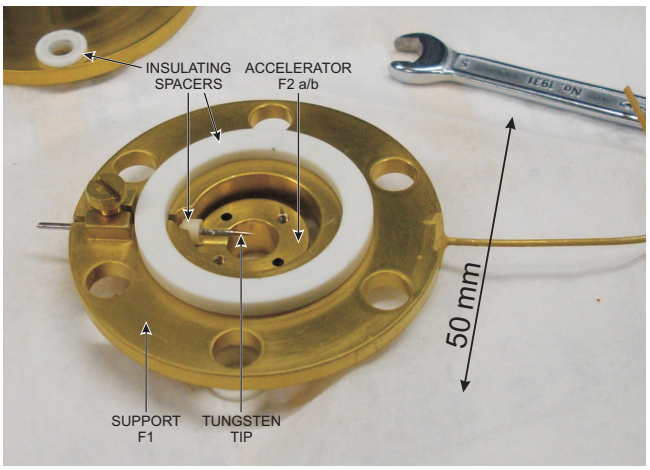

(a) F1 and F2 with tungsten tip, screw and spacers.

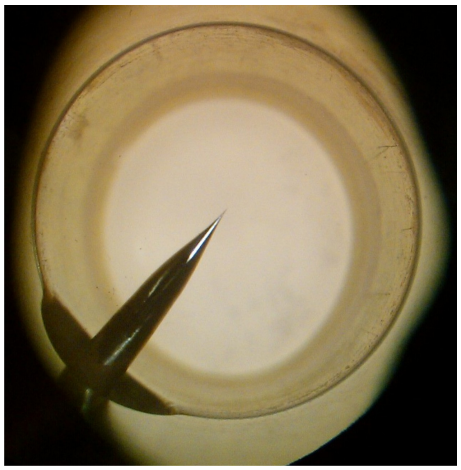

(b) The FEP under a light microscope.

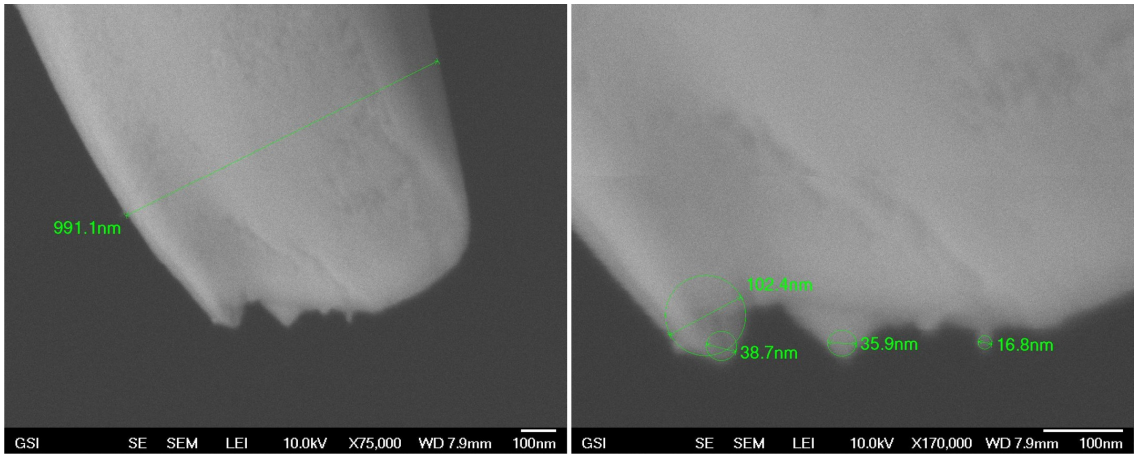

(c) The FEP under a scanning electron microscope (SEM).

Figure 4.8: Images of the electron source.

up to 500 nA. The resulting (inverse) characteristics are drawn in figure 4.9.

The characteristic curves can be sorted in three different groups: High accelerator voltage is required (2.2 kV for 500 nA), if the FEP is grounded. Medium voltage (1.3 kV), if the FEP is negative, but less negative than the reflector (by at least 0.5 kV). The lowest voltage (1.0 kV) is needed, if the FEP is equal or more neg than the reflector. In all cases the FEP starts firing at about 0.65 kV accelerator voltage. In agreement to this, we observed a transition in the emission behavior, if the accelerator is kept at 1.0 kV and the ratio of reflector and FEP voltage is changed: If that ratio has a value above 1.2 or 1.3, the FEP current is always around 150 nA. With ratios below 0.9, the FEP fires with 450 nA current.

This is best interpreted by a space-charge modified potential, considering the nearby CT electrodes, partly biased with −250 V, and the grounded chamber: With the FEP being more negative than the reflector, electrons are not confined and we observe an unperturbed tip characteristic. If instead the reflectors enclose electrons in a well, they induce a negative space-charge potential, which reaches to the tip and reduces the current (or equivalently, higher accelerator voltage is

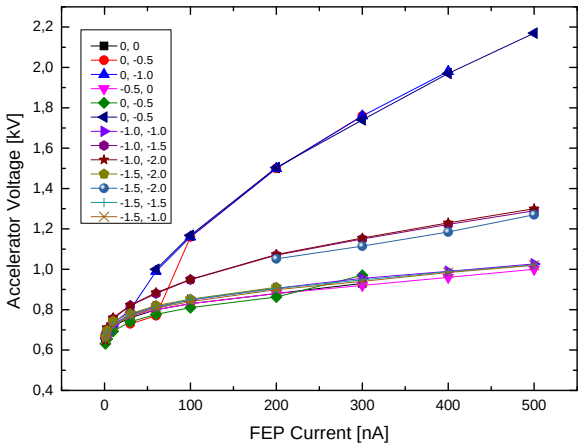

Figure 4.9: Current-voltage-characteristic curves of the electron source at different settings of (FEP, reflector).

required). If eventually the tip is grounded, it dives deeply into the electron cloud and the aforementioned effect is even enhanced. This interpretation is confirmed by measurements with the Faraday cup: In case the reflectors did not confine electrons, a large part of the emission current was detected on the FC, placed behind the reflector doublet H8/9. We therefore sticked to setting the reflector considerably more negative that the FEP, in order to protect the FEP from damaging and the FC from large background.

4.5 The Gas Injection System and Watchdog

Argon atoms are injected into the creation trap from a gas bottle below the magnet for bombardment with electrons (cf. Sec.5.3). There are in total 5 stages of valves (some are depicted in the schematic drawing, Fig. 4.10(a)) in order to protect the trap chamber from pressure and moisture, which would build up ice, reduce ions by charge exchange, and potentially even quench electronic transitions.

For injection of controlled amounts of atoms a pressure-regulating 'prechamber' (Fig. 4.10(b)) has been formed of a small vacuum cross with SWAGELOK and KF technology. The upper port is connected to the trap chamber via two shutoff valves—one is remote-controlled (v1) for defining short pulses, the other one is a backup with manual operation. A stainless-steel tube continues this arm, entering the magnet vacuum chamber through an O-ring sealed compression port. On the left, gas enters through a (large, coarse) metering/shutoff valve (v2), being supplied by a 10 liter bottle of compressed argon gas, purity 4.8, via a pressure reducer and a long stiff hose. The surplus is pumped away with a RV pump, through another metering or shutoff valve (v3) at the lower port, next to a Pirani gauge, which measures the prechamber pressure. The port to the right features a smaller, finer metering valve, backed with a small gas can. This is no longer in use—it might however serve as short-term reservoir, comparable with an electric low-pass filter.

The pressure reducer is set to around 1 to 2 bar overpressure in the tube. The two metering

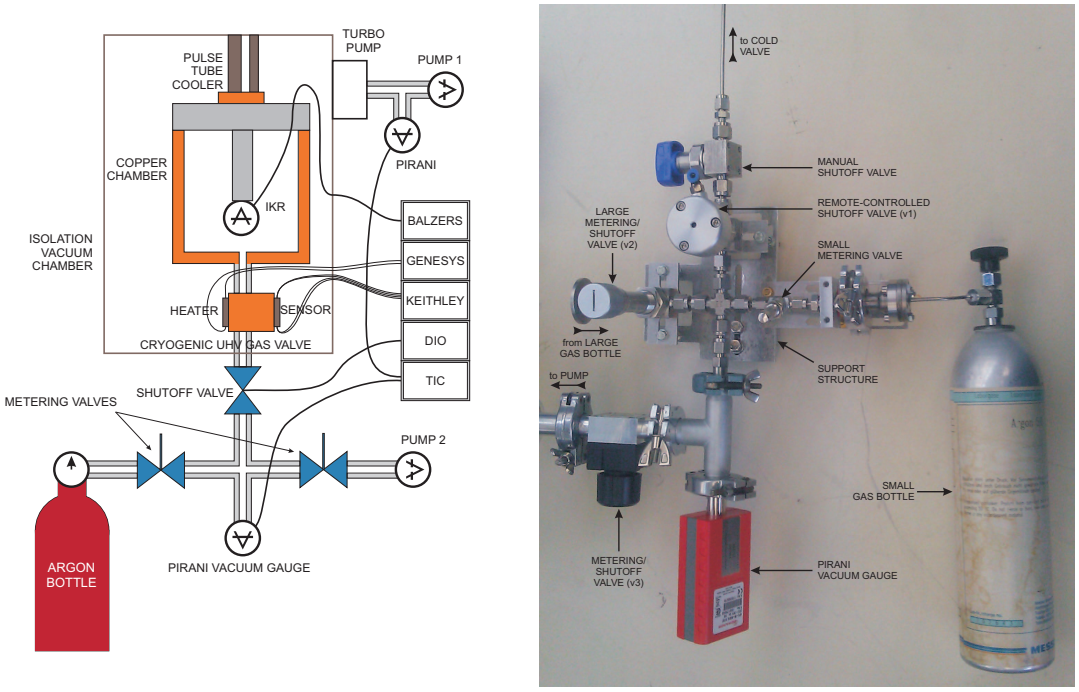

(a) Schematic drawing of the gas injection system—the IKR gauge was in the place of the trap during testing.

(b) Photograph of the prechamber—this is a part of the system which is outside of the outer vacuum chamber.

Figure 4.10: Overview images of the gas injection system.

valves v2 and v3 are set as follows: With closed v2, v3 is regulated such that the residual gas pressure is below 1 % of the desired argon pressure—this is to minimize contaminations without consuming the argon supply too fast: If v3 is opened too far, the large bottle loses its entire content within a few days of operation. With fully open v3, the RV pump produces around 10^{-3} mbar in the prechamber; when all valves are closed, the pressure soon rises above 10^{-2} mbar, even though a helium sniffer confirmed a leak rate as low as 10^{-2} mbar l/s (at $5 \cdot 10^{-3}$ mbar) to the standalone prechamber in a previous test. The pressure falls back to 10^{-2} mbar, if v3 is slightly opened. Then the pressure is raised to around 1 mbar argon by faintly touching v2. This is a sensitive interplay of the metering valve v2 and the pressure reducer, which does not provide stable operation if the downstream pressure is too low. The reducer also overshoots by around a factor of 2 upon opening of the gas bottle. The additional freedom of setting v3 helps in finding a working point. Still we observe pressure fluctuations by some 10 % between night and day.

If the prechamber pressure has reached the design level, it is ready for a short gas pulse. To that end, the remote-controlled valve is charged with pressurized air, supplied from a solenoid valve, which is connected via a 2 m long hose. This complication is necessary, because the target valve is mounted directly below the superconducting magnet, where a solenoid valve could neither be functional nor tolerated. The solenoid valve is a MAC 36A-ACA-JDAC-1BA 3-way valve, connecting the output either to the pressurized-air input, supplied with the local system available at the HITRAP platform, or with atmosphere. It is supplied with 24 V, 5.4 W from a rack power supply, switched by a relay. The power supply and relay are part of the GSI-made ‘watchdog’

(WDG). The name describes a fail-safe function, which will be described below. This instrument can be programmed with a pulse time in the range of 24 to 94 ms. During the pulse, the solenoid is powered, forwarding pressurized air to the target valve, which releases gas into the stainless-steel tube.

The stainless-steel tube is continued inside the magnet vacuum chamber by a second tube via an I-piece with double O-ring—construction requires possibility to disassemble into upper and lower part and this solution offers flexibility of tolerate thermal contraction of the cooled experiment core by a few millimeters. The upper part is hard-soldered to the base plate of the trap chamber (hollow cylinder) via another valve-like instrument, referred to as 'oven' or 'cold valve'—in contrast to the 'cryo-valve' or fast opening valve [Vog14], which is a completely different instrument replacing the cold valve when it comes to injection of externally produced ions.

The cold valve relies on the principle of gas adsorption to cold surfaces, see [Lin10, pp. 39-45] and references therein, particularly [DDD+09]. By several baffles perpendicular to the direction of gas flow, a geometric obstacle to incoming atoms is formed (Fig. 4.12(a)) such that they hit the surfaces many times before they can enter the trap chamber—a simulation with Molflow+ estimates the transmittance of the valve, depending on the sticking probability [Mar10, Tin86, MS08]. From this we derive an average of 60 collisions per atom in the molecular flow regime, which holds up to around 10^{-2} mbar. The system in its full assembly is depicted in figure 4.11. It has a weak thermal contact with the trap chamber, cooling it to around 15 K and can be heated up to at least 100 K by the attached resistors, which justifies the alternative name 'oven'. If the temperature is low enough, all gas will stick to the walls, which is the 'closed' state. Above a certain threshold, there is an increasing probability for atoms to survive all collisions with the valve, making the valve gradually transparent, or 'open'. Another temperature-dependent process, namely desorption, adds a 'source'-like component to the behavior of the valve.

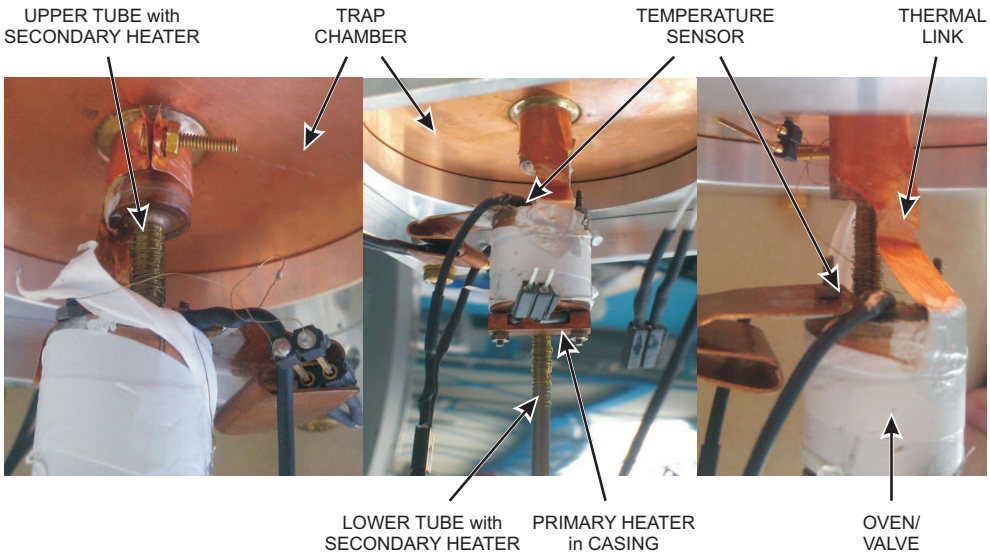

Figure 4.11: Photograph of the cryogenic gas valve (oven) in final setup.

The primary heater is a 0.3 kΩ VISHAY MBB 0207 thin film resistor, wrapped in indium foil and surrounded by a copper casing for good thermal connection with the oven. The secondary

heater consists of a thin constantan wire wound around the tubing above and below the oven many times (Fig. 4.11) for baking the tubes out in case they get clogged after long operation. It has a total resistance of 0.3 kΩ, as well, and is covered with an electrically insulating oxide layer. Both heaters can individually be connected to a GeneSYS TDK-Lambda power supply, capable of 750 W output power, which is more than enough for our application. In case the strong electric noise of this switching power supply disturbs a measurement, it should be replaced by an analog power supply by Hewlett Packard. The oven temperature is measured with one of the CCS sensors, mentioned in section 4.2. The relays for contacting the heaters to the supply are also controlled by the WDG. In contrast to the gas pulse relay, these are made for an external supply. And since the typical time scale of heating is rather seconds, these are controlled without a specified contact time, but require ON and OFF commands, separately.

Systematic tests of the valve have been performed with a temperature stabilization routine and a time-resolving pressure gauge as detector of the transmitted gas upon injecting gas for 100 ms into the valve, see figure 4.10(a) for the setup. Some results are highlighted in sub-figures of figure 4.12. Figure 4.12(b) was obtained with a similar setup, but focusing on the total transmittance without timing information. This test reveals an exponential dependency for low temperature up to a saturation at around 40 K. The time-resolved measurements indicate influence of the gas type (krypton and neon were tested as well) and pressure, the oven temperature, and aging. At 0.1 mbar input pressure (Fig. 4.12(c)), the valve transmits a short gas pulse of around 10^{-9} mbar height and 1 s length, which is almost independent of temperature, in the range from 26 to 38 K. With lower input pressure (0.05 mbar), this pulse cannot be detected. This nonlinear behavior can be interpreted as a laminar pressure wave, pushed through the valve with some atoms having no contact with the walls at all. This is consistent with the transition from molecular to laminar flow in this pressure regime, as explained above. At temperatures above 34 K (for argon), desorption causes an 'after-glow' for many seconds, following the initial pulse. After some days of operation, a test has been done with a pressure of 1.0 mbar: Figure 4.12(d). This time, no signal could be seen below 34 K. Above, the transmission depends strongly on temperature, but still shows the undesirably long time structure. This is fairly consistent with the data from figure 4.12(b), which were however measured with 0.15 mbar input pressure. Some of these results have been published in [LGW+13].

After setting up the experiment for advanced measurement phases, we have revised the valve behavior. We detected transmitted particles via optical fluorescence, Faraday-cup current, and resonant axial-motion signal upon electron-impact ionization. These measurements are reported in section 5.3.

Besides the functionality of switching relays, the WDG device has an optional watchdog function: If it is activated, it watches for a live signal, which is implemented as a toggling logic level (0 or 5 V) with a rate of above 0.8 Hz (half period below 0.6 s). This 'watchdog toggler' is supplied from the output of a PCI card (channel PCI-Do.0, cf. Sec. 4.8). During a procedure which includes gas injection or anything else controlled by the WDG, the toggler is usually requested from the coordinating LabView routine with a half period as low as 0.1 ms. The WDG puts out a logic alarm signal, which is low (0 V) in the 'fired' case: live pulses have failed since the WDG function has been activated, for instance due to a system crash of LabView. In this case, the WDG function has to be restarted (OFF and ON). In all other cases (WDG OFF, or WDG ON

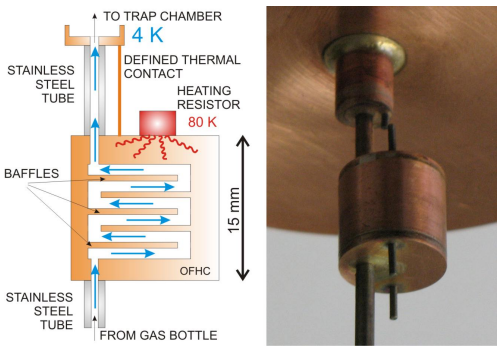

(a) Schematic drawing of the adsorption valve with heater and tubes, soldered to the vacuum chamber, viewed in vertical section, and photograph.

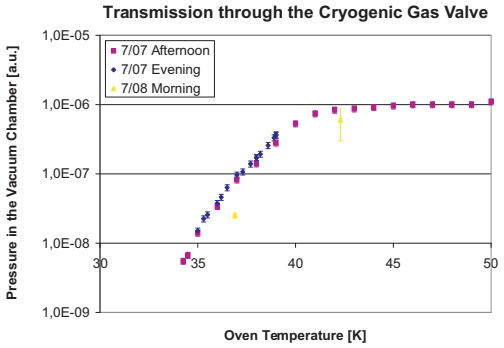

(b) Peak pressure in the vacuum chamber after a medium-pressure gas pulse.

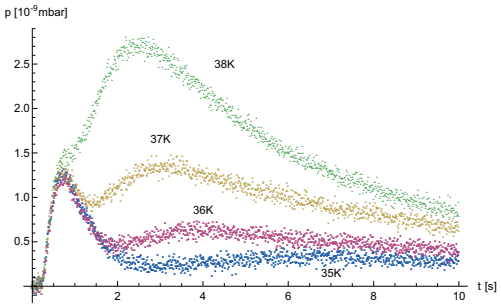

(c) Time-resolved pressure in the vacuum chamber after a medium-pressure gas pulse, background corrected.

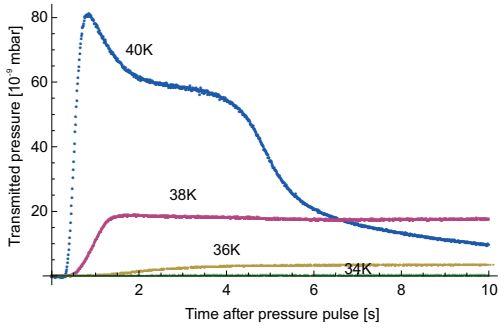

(d) Time-resolved pressure in the vacuum chamber after a high-pressure gas pulse.

Figure 4.12: Cryogenic gas valve: images and tests.

and pulses have come all the time), the WDG output is high (5 V). This WDG output is also connected to according interlock inputs of our most sensitive high-voltage devices, which are the HV-FEP ('watchdog input', cf. Sec. 4.4) and the CPM (channel photomultiplier and its 'HV kill' input, cf. Sec. 4.10). If the interlock function is not wanted for the HV-FEP, a switch next to the input must be set to 'device always on' instead of 'BNC input'. At the CPM, the kill input can be simply disconnected and will be pulled up by the module itself. Regarding the relays discussed in this section, the WDG opens all relays in the fired case and refuses to close them unless restarted.

4.6 Three Non-Destructive Ion Detectors: Resonant Circuits and Cryo-Amplifiers

Part of the cryogenic electronics are three tuned LC circuits for resonant ion detection and cooling of ions via image currents. Their functions are in principle described as follows:

As pointed out in section 3.4, a moving ion induces an RF image current in the range of fA in a trap electrode, as depicted in figure 4.13(a). This current is directed into the detection branch via a high-pass filter, formed by a resistor R_D and a coupling capacitance C_D. This unit separates the RF signal from the DC trap supply, which would otherwise be grounded through the attached

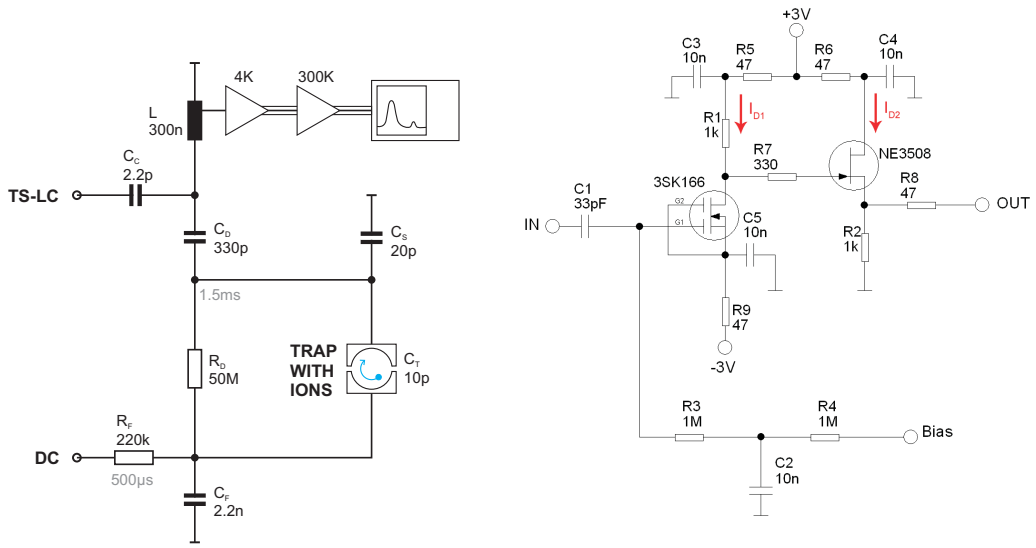

(a) Example diagram of an LC circuit, formed by trap electrodes and a coil.

(b) Circuit diagram of the two home-made cryogenic amplifiers. Source: [Hül11].

Figure 4.13: Circuit diagrams in the context of resonant ion detection.

coil. For clarification, the diagram contains the DC supply (low-pass filtered via R_F and C_F), which is attached to both segments of the electrode. The current then passes through this coil with inductance L in the range of mH or μH into ground. Together with the trap capacitance C_T of about 5 pC and some other stray capacities C_S, the coil forms an LC circuit with a resonance frequency of $2\pi\nu_{LC} = 1/\sqrt{LC}$, matching the axial and cyclotron frequencies of stored ions in the frequency range of 1 or 35 MHz, respectively. All coils have cylindrical housings, shielding them from outer influences, with optimized geometry for obtaining a high resonator quality factor Q_{LC}.

An additional wire is soldered to each coil, exploiting some of the windings as secondary coil, in which a voltage is induced. In case of a high quality factor, the voltage is resonantly raised to the nV regime. This is further processed by a cryogenic 2-stage amplifier (Fig. 4.13(b)), positioned close to the resonator (symbolized by just one 4K amplifier in the drawing). The first stage minimizes load to the resonator due to its high input impedance. The second one (source follower) matches the signal to the impedance of a coaxial cable. With a voltage amplification of around 3, the cryo-amplifier mainly fulfills the purpose of power amplification. Outside the cryogenic vacuum, the signal gets amplified another time and measured with a spectrum analyzer. The resonance circuit can be artificially excited with an external test signal TS-LC, via the coupling capacitor C_C, which is too small to load the circuit significantly.

Two of our detection systems use an almost identical resonator housing, as seen in figure 4.14(a) (together with the lens holder)—their real position in the current setup is depicted in the photograph 4.14(b). These are the cyclotron resonator made by M. Hüllen [Hül11] and attached to a segment of E4 (‘CRES’), and the axial resonator at E2 (‘ARES ST’). M. Shaaban designed this detector, following the example of CRES, therefore also the amplifiers are basically identical. Their circuit diagram is shown in figure 4.13(b), photographs are found in figure 4.15. In these cases, the first stage consists of a 3SK166 dual-gate MES FET by Sony, while the source follower

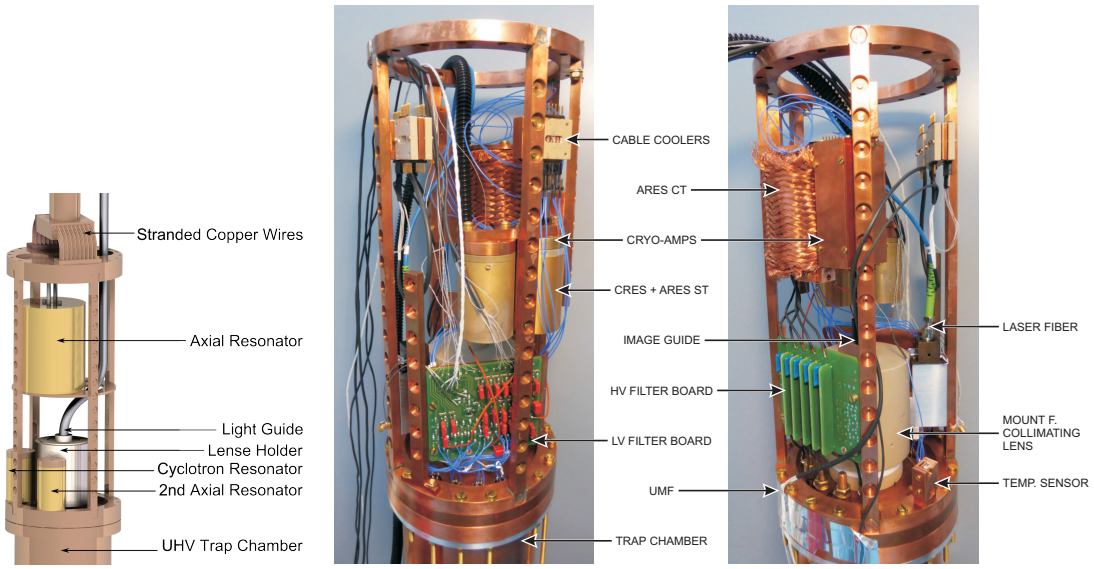

(a) Resonators and optics.

(b) Photos of the experimental core.

Figure 4.14: 4-leg electronics housing with many components shown.

uses a NE3508 (HJ FET) by NEC. Both transistors are based on GaAs, which has semiconducting properties down to 1 K.

The main difference between the two systems is the coil: CRES uses a helical coil of only 10.5 windings with 725 nH inductance, made from 1.5 mm thick silver-plated copper wire. ARES ST has around 300 windings of Teflon-insulated NbTi wire with 75 μm metal diameter, and the inductance is in the range of 3 mH. This material is superconducting below the critical temperature of around 7 K (at 7 T magnetic field—the field-free transition temperature is 9.3 K). The resonator housings are made from silver- and gold-plated OFHC copper.

Despite the high electrical conductivity of a superconductor, heat transfer is very poor. Therefore great care should be taken to cool the wire of the axial resonators. As seen in figure 4.16, the coil is wound around a Teflon body and wrapped in Teflon tape. Some connections cannot be done within the wrapping, so they need to be as short as possible. A short piece of NbTi is soon continued by thick copper, establishing contact to ground, amplifier, and the input from the filter board.

The amplifiers are supplied with each three channels of another device from the BS series of Stahl electronics: BS 1-10 cryo has been designed with 10 channels, capable of ± 5 V output voltage, which supply up to ± 10 mA (4-sector operation). Two inputs for amplifier stabilization via 2 PID loops were replaced by two additional outputs with manual control only. '+3 V' of the amplifiers is a common drain of both transistors (also connected to G2 of the first stage) and '-3 V' supplies the first-stage source (with values according to their names). 'Bias' is the G1 voltage of the first-stage transistor. The second-stage source is grounded and a dedicated AMP GND line conducts this current back from the 4-leg to the supply.

While the axial resonance of ions with resonators is easily tuned by the trap voltage, there is no such option in case of the cyclotron motion. Altering the magnetic field strength would affect the Larmor frequency and our equipment is specialized for a narrow band of operation.

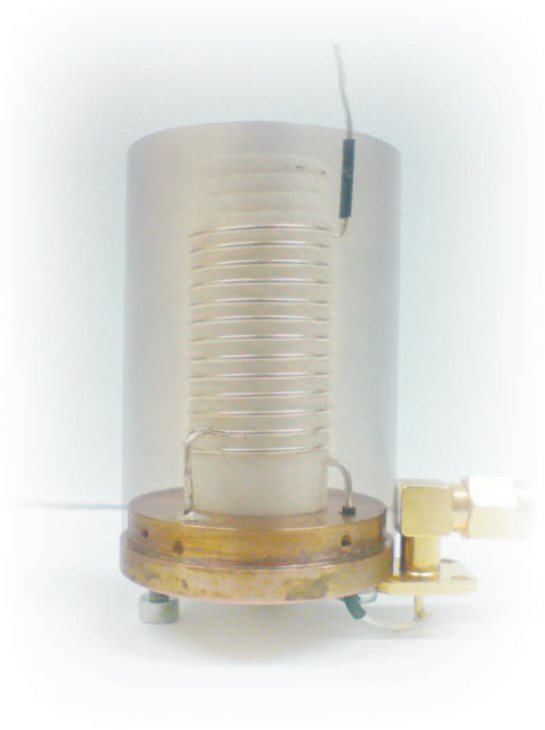

(a) The housing with coil.

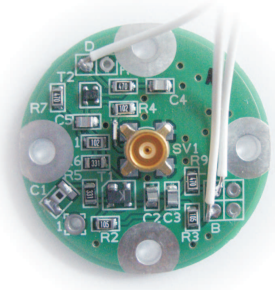

(b) The amplifier board.

(c) The housing with amplifier.

Figure 4.15: Photographs of the cyclotron resonator (CRES). Transparency of Figs. 4.15(a) and 4.15(c) is artificially achieved by photomontage with the purpose of showing the inner parts and the housing in one image. Source: [Hül11].

On top of this, the specified homogeneity of the magnet (cf. Sec. 4.1) would be lost. Instead of this, the effective resonator capacitance can be tuned by adding a grounded branch (parallel to C_S in Fig. 4.13(a)), see [Hül11, p. 21]. It consists of a normal capacitor and capacitance diode, with a value depending of the applied DC voltage. This circuitry is currently not included in the setup, because originally the resonance frequency was rather too low than too high. In this case, additional parallel capacitance is of no use.

The axial resonator attached to E13 (ARES CT) is borrowed from the group of S. Ulmer, BASE, CERN, and can be seen in the photograph 4.14(b). It will soon be replaced by a new detector, which will be rather similar. In this system not only the coil, but also the resonator housing is made of NbTi. We added a jacket of copper strand for cooling the housing and shielding it from the radiation shield, in order to maintain superconductivity. The temperature is monitored and we find it to remain below 7 K even on the warmest days of the year, when the radiation shield temperature rose to almost 44 K. The amplifier is again divided into a first stage with a dual-gate transistor and a source follower with a single gate. In this case, five voltages need to be supplied externally: The drains of both transistors (DR and SFD, both with +3 V) and all gates (G1, G2, SFG). Figure 4.17 shows the amplifier board with recommended values (the amplifier housing has been changed for our purpose).

We performed repeated tests of the resonators with a Rigol-DSA815-TG spectrum analyzer.

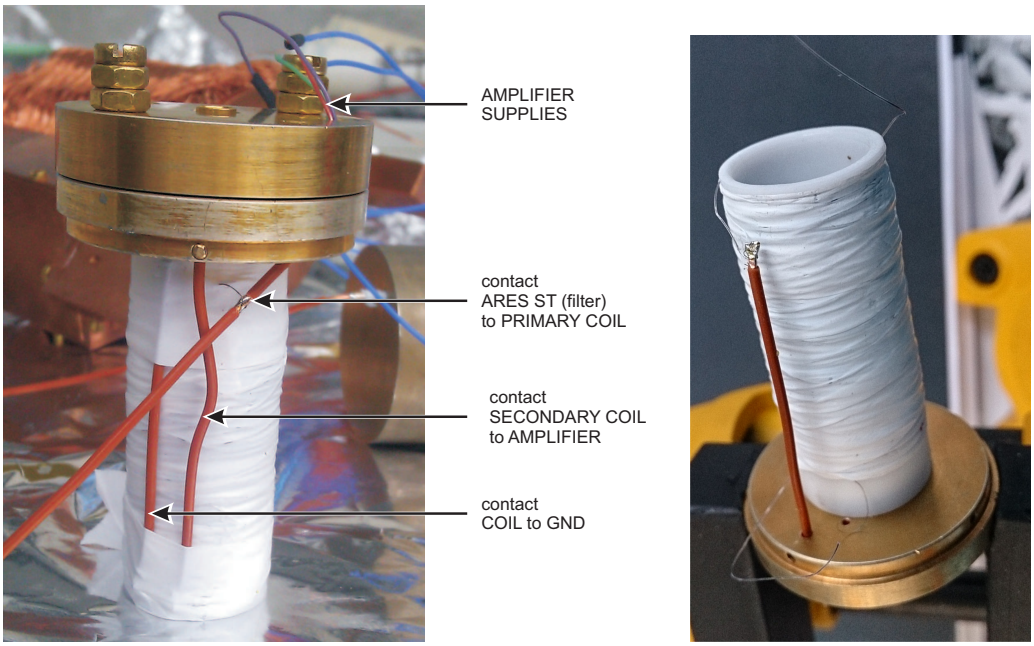

(a) Shortly before closing.

(b) Teflon body visible.

Figure 4.16: Photographs of ARES ST, showing efforts for cooling the NbTi wire.

Table 4.6: Settings and characteristics of the three resonators in use, ARES ST being re-measured after modifications (*).

Resonator	Gate(s) [V]	I_1 [mA]	I_2 [mA]	ν_{LC} [Hz]	$\log P$ [dBm]	Γ_{LC} [Hz]	Q_{LC}
ARES CT	−0.69, 0.00, +0.80	+2.1	+1.6	637.9 k	−105	0.3 k	2.1 k
CRES	−3.84	+3.0	−2.2	35.05 M	−71	0.25 M	140
ARES ST	−4.21	+2.9	−1.4	783.1 k	−100	1.7 k	460
ARES ST*	−4.00	+2.9	−1.85	840 k	−32	15 k	56

Tests were conducted with simulated trap capacities in a cryogenic testing setup outside the magnet, with the full setup in the warm and in the cold, with and without RF excitation by Rigol ('TG' for tracking generator) at the TS-LC input. The most significant results are reported in table 4.6, listing the applied settings (working points), measured resonance frequencies and quality factors. We use the full width at −3 dB below maximum (roughly FWHM) as definition of Γ_{LC}.

I_1 and I_2 are the currents measured in the loaded supply channels. In case of the three-channel amplifiers (CRES; ARES ST, 'Mouw.'), the individual drain currents can be concluded as $I_1 = I_{D1} + I_{D2}$ and $I_2 = -I_{D1}$. With the five-channel amplifier (ARES CT, 'Ulmer'), the assignment is $I_1 = -I_{SFD}$ and $I_2 = -I_{DR}$ (mind the inversion of 1st and 2nd stage). The three gate biases are in the order U_{G1}, U_{G2}, U_{SFG}.

The measurements without (*) are from summer 2014, before opening the experiment for several necessary repairs. After closing we checked the systems again and they appeared slightly changed. The noise signal (without TG) of ARES CT was measured with 100 Hz RBW of Rigol

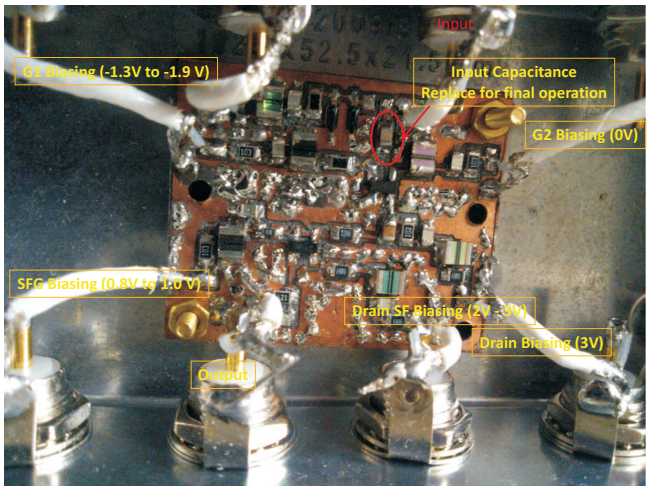

Figure 4.17: Photograph of the ARES-CT amplifier with recommended settings.

(peak height depends on the RBW setting). The measured temperature was 4.94 K. For all measurements presented in chapter 5, we used gate voltages of −0.80, +0.10, and 0.00 V and the peak frequency was 635 kHz.

The CRES working point was determined at the same day, as the lowest bias voltage that reaches maximum peak level. The peak noise level is higher than of ARES CT, because we set RBW to 100 kHz. With video averaging of 32 traces, the signal could be seen.

ARES ST was measured with 300 Hz RBW and 16 traces. This detector appeared at quite different settings and frequency in the later revision, therefore it is dedicated a second raw (*). The amplification behaves plateau-like between −3.8 and −4.1 V 'Bias' voltage, therefore we chose the power-saving working point −4.10 V. The quality factor was then however so low that we needed to excite the resonator with the TG output at −20 dBm. Unfortunately this function slightly shifts the displayed spectrum, due to some internal issues of Rigol. The current operation is at −4.00 V Bias voltage and we detect best ion signal in the 833 kHz band of the spectrum analyzer.

The low quality factor of ARES ST could indicate that part of the coil does no longer get cooled sufficiently, such that superconductivity is lost and the rather high resistance of the normal conducting state of NbTi hampers the resonator current. Something might have broken during shutdown, or the measures for cooling (s. above) were not sufficient in general. However the rather high additional shift in frequency could be a hint to other issues, maybe a broken contact. Anyways, with the detector in this shape it is not possible to see ions without high motional excitation.

Also the CRES frequency has changed a bit compared to the status reported in table 4.6. Nowadays it amounts to 36.5 MHz (in the cold—mind a shift up by 0.5 MHz while cooling down.), which is too high for $^{40}Ar^{13+}$ ions in the given magnetic field. Therefore in future, resonance matching by the capacitance diode could be an option. The risk is however another incompensable down-shift, because the frequency is very sensitive to small variations, even of the wire position. After all, the discussion demonstrates that the working points and resonator frequencies should be revised every now and then. The values presented in table 4.6 are only examples, conveying the range where the parameters should be expected.

4.7 The Filter Boards

Next to the resonators there are two printed circuit boards with low-pass filters and units for coupling and decoupling of AC and DC voltages. They are complemented by a set of four room-temperature boards, hosted in an electrically shielded box at the low-voltage flange of the magnet hat, see section 4.1. The latter comprise low-pass filters for incoming DC channels, as well as frequency converters and amplifiers for outgoing RF signals, and some multiplexing units. Low-pass filtering, mostly in several stages and with cutoff frequencies in the range of 0.1 to 1 ms, is applied to all DC signals entering the magnet chamber. Also the RF inputs are damped or filtered. These measures have the purpose of maintaining a low-noise environment, which is inevitable for two reasons: Unwanted high-frequency signals on the supplies of the trap could resonantly heat stored ions; and in the resonators they could predominate over the very weak ion signal. The role of all these circuit boards, which have been custom-made by STAHL ELECTRONICS, will be further described in section 4.8.

4.7.1 Cryogenic Filters

The two cryogenic filter boards are placed as closely as possible to the UMF—their position can be seen in figure 4.14(b). Figure 4.18(a) and 4.18(c) show zoomed photos of the boards, fully connected with wires. They are bolted to copper plates for a good connection to the cold 4-leg housing, defining ground potential (HF GND and AMP GND, see Sec. 4.8.—as mentioned in Sec. 4.2, live contacts on the rear side are insulated from GND by Kapton foil). The copper plate behind the HV board leaves space at the places of HV contact.

The functional circuit diagram of both filters is shown in figure 4.19, while figure 4.18(d) depicts the plate layout. Apart from filtering, damping, and cooling of incoming lines, the LV board also features circuitry for combining and separating AC and DC signals: Some of the electrodes, which mostly have nonzero DC potential, are used for RF excitation and the power is capacitively coupled into the line after the filter. This is true for E3, E4.0 (pin 42), E5, E15.5 (pin 13), and E16. E3 is four-fold split for the purpose of applying a rotating wall for radial compression [BVST12, BHM$^+$93], but can be supplied with an oscillating dipole field for exciting the cyclotron motion in ST, as well. The AC inputs are damped with a capacitive voltage divider by a factor of 3. 'CT/ST Magnetron Exc' is filtered by a bidirectional diode threshold filter and supplied to one segment of E4 and E15, which are each split in half. Thus they generate a diagonal field component suitable for quadrupole mixing of radial and axial modes. This filter can be bypassed with ± 20 V DC bias, which is blocked at the series capacitor, only propagated the RF component to the trap electrodes. Other incoupling electrodes (E5 and E16) produce dipole fields for axial excitation in the respective trap. For E5, the modulation is implemented in the room-temperature filter and the AC part is bypassed over the filters by a damped capacitor.

Electrodes E2, E4.5 (pin 43), and E13 are employed as part of the detector LC circuit—these feature outcoupling RC high-pass filters directing of the AC current into the resonator, instead of the filter ground. The high capacitance in these branches does not disturb the LC resonator, but separates it from the DC supply (cf. Sec. 4.6). An additional item on the LV filter board is resistors at the input of each channel for identification of a line by their resistance versus GND. With values above 50 MΩ, they do not load the supplies too much, but are helpful for checking

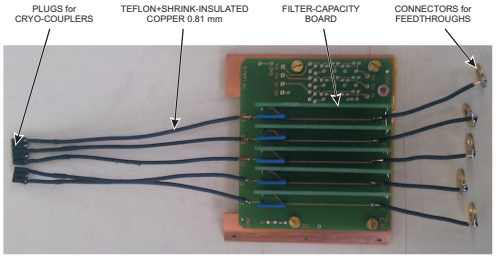

(a) Photograph of the HV filter.

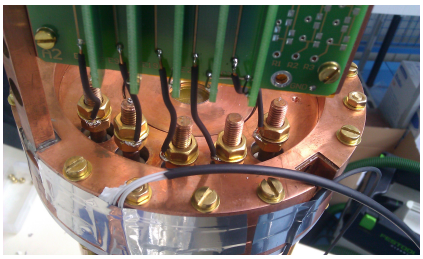

(b) Photograph of the HV feedthroughs.

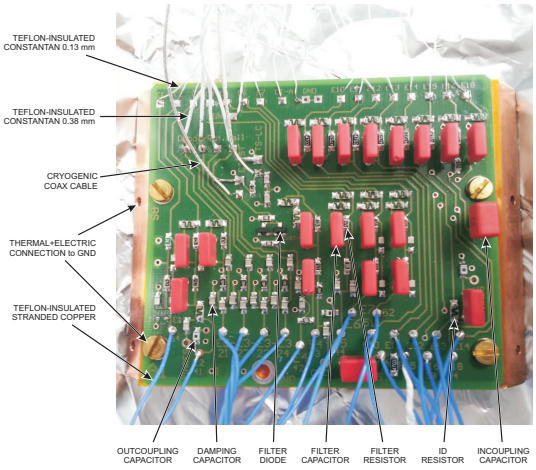

(c) Photograph of the LV filter.

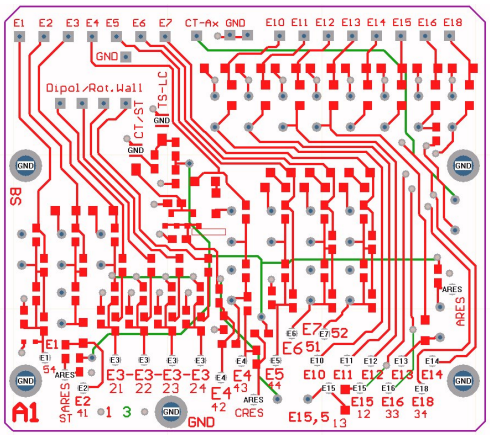

(d) Layout of the LV filter.

Figure 4.18: Images of the cryogenic filter boards.

the wiring once the magnet chamber is closed.

The connection to UMF is made with rather short cables, which are attached to the feedthrough pins after soldering to the board pads. This sequence is tedious, but still more feasible than the other way around. And as long as the optics are not in place, it works out. The LV lines are made with Teflon-insulated copper strands of a few cm length, soldered to the 1 mm thin pins. While soldering, we cooled the pins with isopropanol to avoid unsoldering the cable on inner side. The HV cables are thick single strands of copper, insulated with Teflon and an additional layer of shrink hose to decrease the field strength through the insulation in case a grounded conducting part comes near. We estimated that a cable with 0.81 mm diameter at 4 kV voltage should be covered with at least 0.26 mm insulation in order to limit the resulting maximum field strength to 20 kV/mm, bearable for most insulating materials. The cables are contacted to the feedthroughs via washers and two nuts (cf. Fig. 4.18(b)), because it is hard to solder anything to a 5 mm thick rod of copper.

The resonators are wired to the corresponding outputs on the LV filter board by the same thick copper cables, but without shrink hose. They are made as short as possible, but remote from other material to avoid crosstalk or additional capacitance. The board is equipped with a test input for LC circuits ('TS-LC'), which is coupled to all resonators via a small capacitor of 2 pF.

The DC inputs of the LV filter board are connected with thin constantan cables, which get pre-

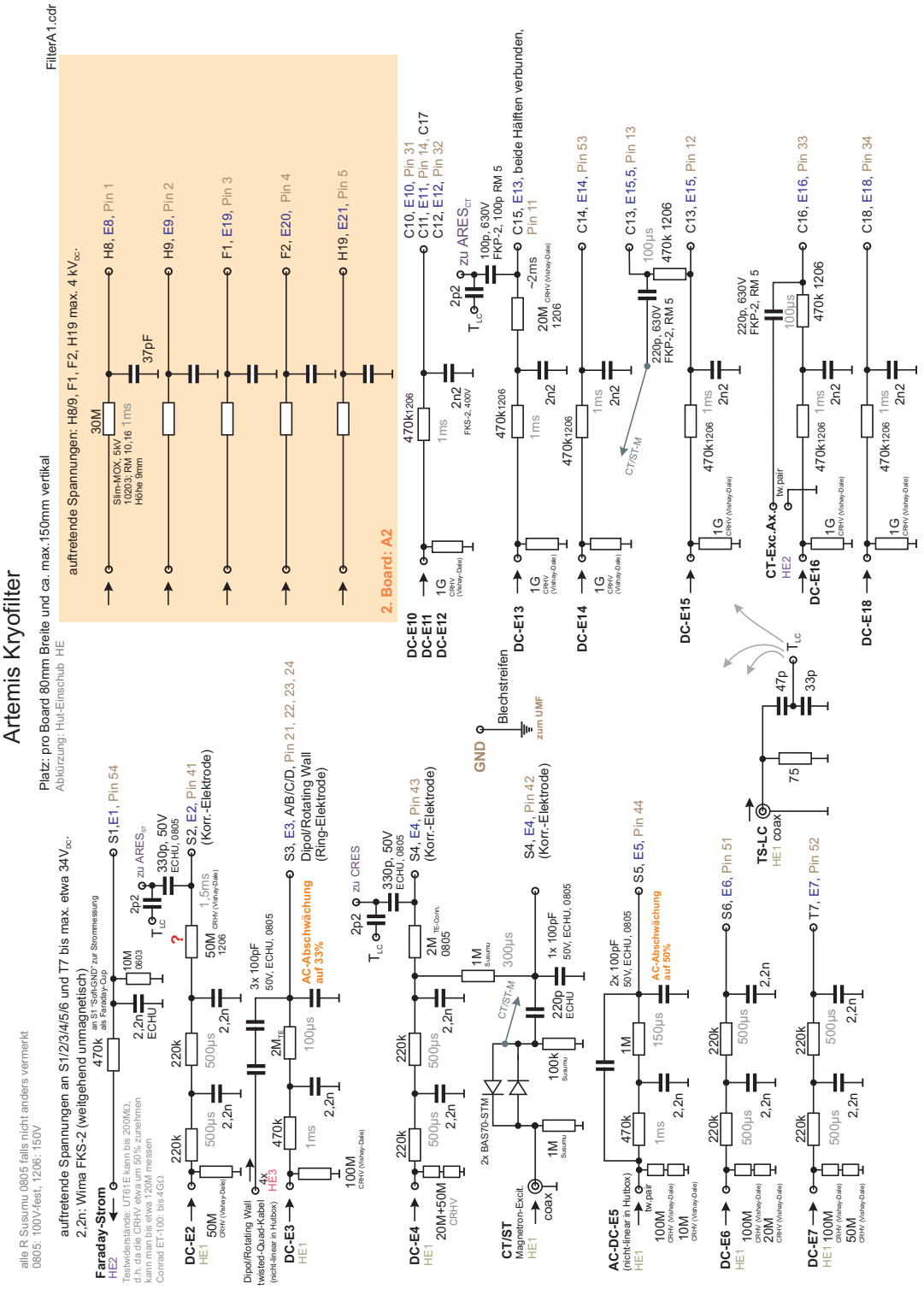

Figure 4.19: Wiring diagram of the cryogenic filter boards.

cooled only at the first stage. Frequencies as high as 35 MHz, namely the test-LC and magnetron-excitation lines are supplied through cryogenic coaxial cables—except for the cyclotron dipole / rotating wall drive, which due to the four-fold symmetry is guided by a twisted bundle of four thick constantan cables. The two remaining AC inputs are the axial excitation lines with a frequency below a MHz. Therefore these are implemented as twisted pairs of thin constantan wires, as well as the measuring line of the Faraday cup (E1), which is paired with its own reference ground.

Both boards are made from glass-fiber reinforced epoxy resin, with four copper layers. This material adds parallel capacitance to the LC resonators. We measured the capacities at the resonator-output solder pads to be 30 pF (ARES ST), 34 pF (ARES CT), and 77 pF (CRES), while the respective UMF feedthrough pins have 11 pF (E2), 13 pF (E13), and 5 pF (E4.5) capacitance vs. GND. The capacitive properties are deliberately used in case of the HV filter board, having five small boards soldered on top of the main board as filter capacitance, see figure 4.18(a).

4.7.2 Room-Temperature Filters

Outside the magnet vacuum chamber, four printed circuit boards are plugged in corresponding slots of the 'hat box' (seen in Fig. 4.20). This is a shielding stainless-steel cuboid, holding them next to the four D-sub 25 connectors of the LV feedthrough. The plug-in boards are called HE 1 through 4. The boards comprise low-noise amplifiers (noise density about $1.2\,\mathrm{nV}/\sqrt{\mathrm{Hz}}$) and frequency down-converters for all three resonators. Down-conversion is currently not in use, because we measure the 'Line Out' signals (outputs of room-temperature amplifiers) with a Rigol spectrum analyzer, capable of input frequencies up to 1.5 GHz. The signals are multiplexed with 2 external RF relays, controlled by PCI-card digital output channels, see the wiring diagram, section 4.8. Trap biases (DC) are low-pass filtered with 22 μs time constant. RF inputs are resistively attenuated for noise suppression, impedance-matched, and—in case of the axial excitation for ST (E5)—capacitively coupled to the DC bias line. If not otherwise specified, all ports on the hat-box front panel (air side) are SMA sockets. For the pin assignment of all channels confer to wiring diagram.

The four units are organized as follows: HE 1 filters all channels of the temperature sensors (10 μs RC time constant, not interfering with measurement) and heaters (rated for maximum current of 100 mA) 2-stage 5 kHz filter, adding each 10 Ω on both contacts to both heaters. The (male) D-sub socket is simply repeated on the front side.

HE 2 features filters of the LV trap biases supplied by UM and BS devices or HV 200, as well as of the tuning voltage for cyclotron-resonance matching, and of a DC offset to the magnetron excitation line for bypassing the diode filter. It also propagates the FC current from E1 and the 'sense GND' potential, measured at the UMF. The UM (if in use) is mounted on the side of the hat box and is connected to the board via banana plugs and cables of a few cm length. A (female) D-sub 9 socket is mounted on the front side for cabling from BS 1-8B. This unit also processes all RF inputs except for the E3 supplies: TS-LC, ST- and CT-Exc.Ax., CT/ST Magn.Exc, and combines the AC and DC components of E5 and the magnetron excitation, respectively.

HE 3 is made for filtering the cryo-amplifiers supply lines and for amplifying the ARES output signals. As mentioned before, we currently use the Line Out signals. However, this board optionally converts one selected signal down, if supplied with a local oscillator input of 2 Vpp (50 Ω) at

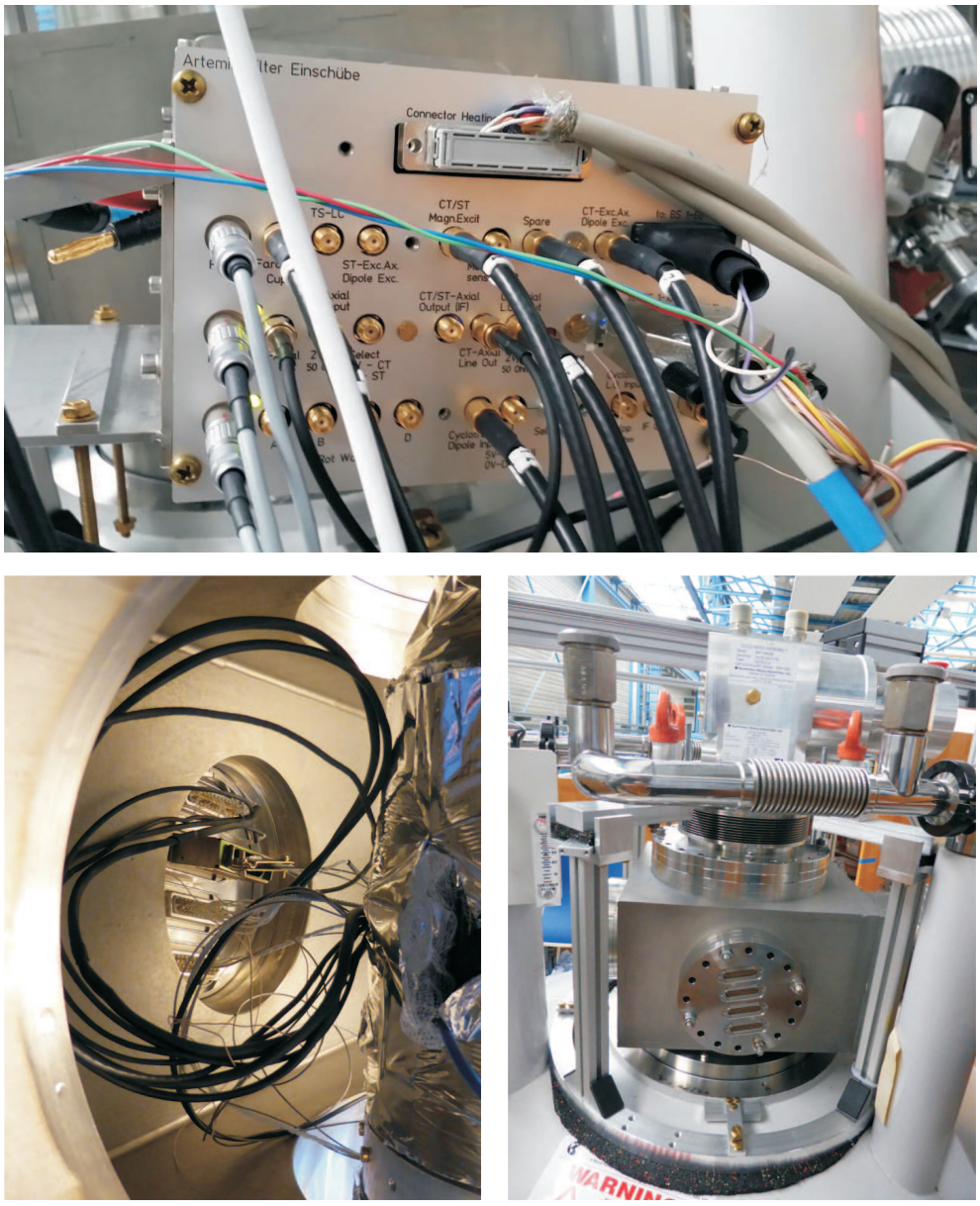

Figure 4.20: Photographs of the hat box front panel (upper part) and of the LV feedthrough flange, to which the box is mounted. The lower left shows the D-sub plugs on the vacuum side, the lower right shows the atmospheric side without further components

a reference frequency slightly below the respective resonator frequency. The cryo-amp biases are supplied via a (female) D-sub 15 socket. The preamplifiers feature a selector at the input from the vacuum feedthrough. It can be manually switched between low and high impedance. By low Z we match it to the cryo-coax cable, because otherwise the system starts oscillating.

HE 4 is the cyclotron board. It offers two options of radial signal on E3: Dipole excitation, supplied by a single coaxial cable, or rotating wall, coming on 4 coaxial cables. These can be selected by a manual switch or by a digital PCI-card line. Currently, it is always set to dipole excitation. In this case, two adjacent segments are supplied with one phase and the other two with the opposite. This unit has an amplifier and down-mixer for the CRES signal, in analogy to HE 3.

HE 2, 3, 4 supplied with $\pm 5\,\mathrm{V}$ and local GND from a dedicated transformer box in a rack with the other bias supplies (BS and HV devices).

The boards are bolted to the front panel of the stainless-steel hat-box. On top of the DC GND connection by the bolted stainless-steel walls, the front panel is connected to the LV flange via a dedicated copper strand for defining RF ground.

4.8 The Trap Wiring

The diagram of the trap wiring is divided in two parts: Figure 4.21 shows the trap electrodes, cryogenic filters, and resonator coils with amplifiers (symbolically), which have been discussed in previous sections. This section focuses on the remaining electrical circuitry, namely the connections between the aforementioned parts and the vacuum feedthroughs inside the magnet vacuum, as well as the instruments outside, as schematically depicted in figure 4.22. It is mainly restricted to the functionality as used for the measurements displayed in chapter 5.

Most lines are cooled at the first, or even the second stage of the cryocooler, by guiding them along a sapphire plate for electrical insulation and simultaneous thermal contact. The cooling units are named k1.n and k2.n Another measure for thermal insulation of the cold area from the warm feedthroughs is the choice of mostly thin constantan wire. Only the high-voltage, high-frequency, and current-bearing lines are partly exempt from these concepts. They are implemented by thicker constantan, the HV lines with extra insulation. The most sensitive RF lines are realized by cryo-coax cables. Only after the second cooling stage, the transition is made to copper for wire material.

We use three different GND wires, all connected to the 4-leg housing or UMF. Amp GND closes the circuits of the cryogenic amplifiers with the supply BS 1-10 cryo, loaded with several mA. The RF strand with the purpose to short-circuit all high-frequent signals connects the UMF with the LV flange and is continued to the hutbox front panel and hence to several electrical devices. Sense GND is used as offset for the floating voltage supplies of trap electrodes, such that their voltage is referenced to a well-defined GND potential. This GND potential is also applied to the endcap electrode S1 via a $10\,\mathrm{M}\Omega$ resistor ('soft GND'), such that the electrode can still be used as Faraday cup, the current of which is guided via a twisted cable and SMA port 1 (HE 2) to the Keithley 617 pico-ampere meter. Additionally, the twisted pairs have their local reference.

The LV lines are distributed to four (female) D-sub 25 plugs (d1 through d4 in Fig. 4.22), connected to the vacuum side of the LV feedthrough flange (Fig. 4.20). They are matched to

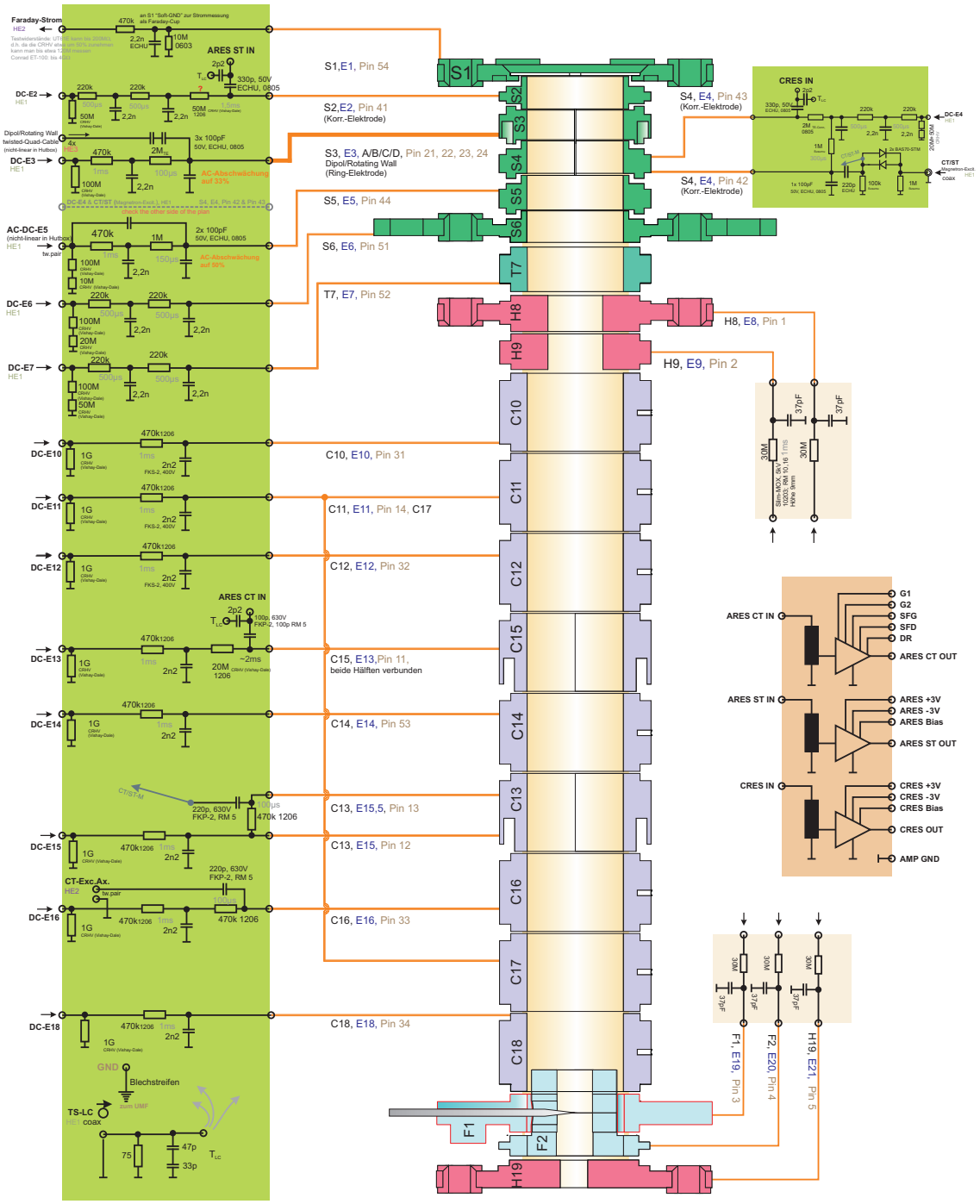

Figure 4.21: Wiring of the trap electrodes with the and cryo-filters and amplifiers.

the room-temperature filter boards HE 1 through 4 on the air side. The front side of these boards features D-sub sockets for shielded multicore cables to supply the trap, amplifiers, and the complex of temperature sensors and heaters. Additionally there are SMA sockets AC inputs and outputs. Axial excitations are supplied to SMA 3 and 7 (HE 2), radial ones to SMA 10 through 13 (rotating wall) or 14 (cyclotron dipole, HE 4), or 4 (magnetron side band, HE 2). The DC

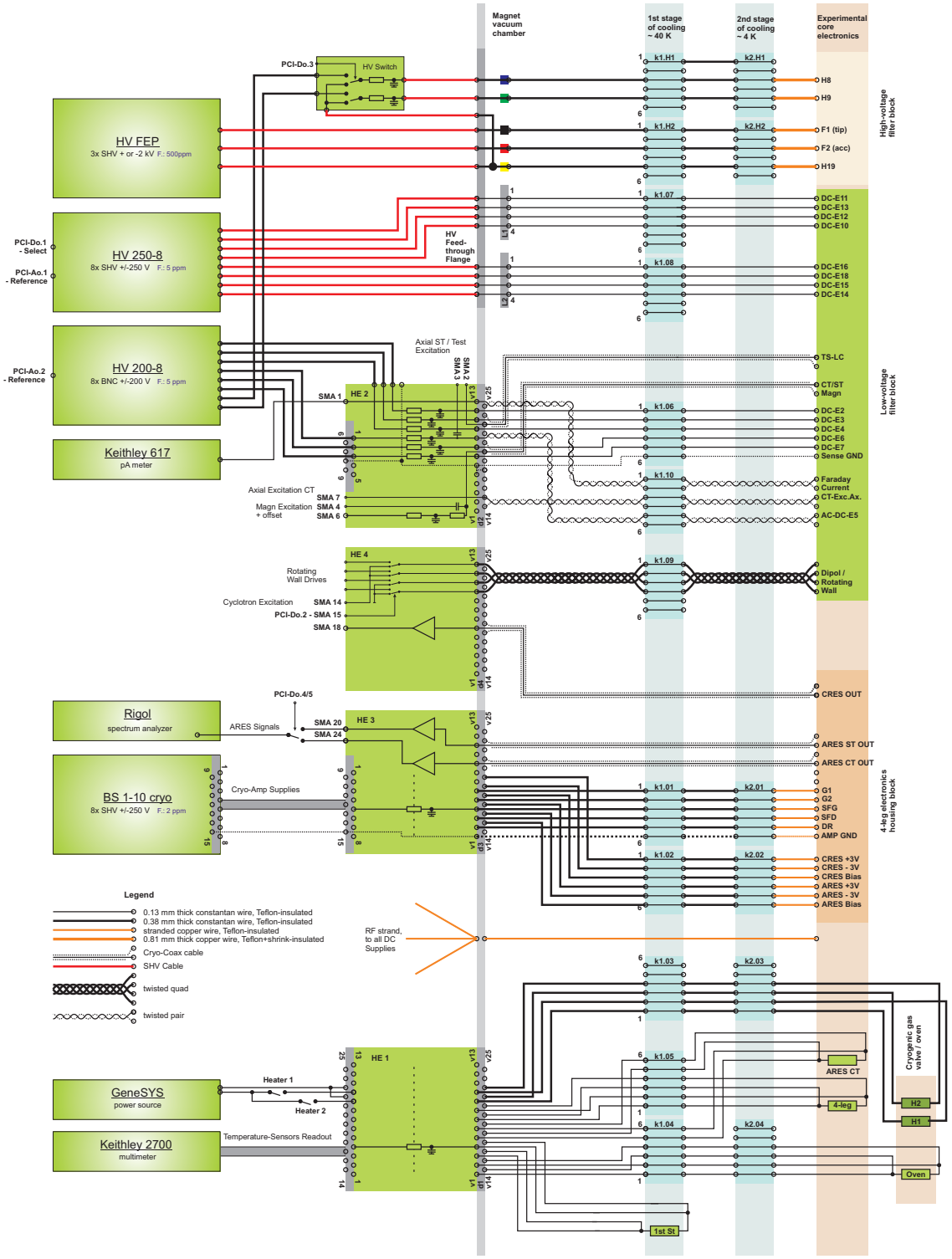

Figure 4.22: Wiring of the vacuum chamber and peripheral devices.

offset for magnetron excitation in ST / CT is supplied by chn. 5 of BS1-8 and connected to SMA 6 (HE 2). A value of ±20 V will raise the total signal over the threshold of the diode filter on the

Figure 4.23: Photographs of the HV feedthroughs, with Lemo and banana sockets at a Teflon flange on the vacuum side (left) and SHV connectors on the atmospheric side (right).

cryo-filter board.

The HV cables are connected to the second electrical feedthrough flange, depicted in figure 4.23. To that end, a set of banana and Lemo sockets are mounted to a Teflon disk on the inside, which is permanently connecting the pins to 16 welded SHV sockets for supply on the outside. The reflector channel is repeated inside the vacuum to a second SHV socket, from which the potential is guided to the two-channel HV switching box. This box multiplexes between the HV potential and individual LV supplies and propagates the selected voltage to the electrodes H8/9. Each channel of the switch operates with two relays and a low-pass filter at the output. The common HV input is shared with the lower reflector for the reflectron mode of the electron source. LV inputs are protected from HV with a low-pass filter 47V TVSB diodes. During transport and measurements in ST, H8/9 are switched to the LV input, defined by HV 200-8 or BS 1-8 (not depicted). The switch is controlled by one of the digital outputs of a PCI-DAS6034 card, namely channel 3 (PCI-Do.3, LO for LV, HI for HV).

The remaining sockets are supplied with 4 m long SHV cables from the HV 250-8 (for the CT) and HV-FEP (for the electron source) devices by Stahl electronics. HV 250-8 is switched to the ramp mode with another digital signal (PCI-Do.1, LO for internal, HI for external reference) and the external voltage is supplied with PCI-Ao.1, which is the analog output 1 of a PCI-DAC6703 card. PCI-Ao.2 is permanently used as reference for HV 200-8, the supply of the ST.

Further digital PCI channels are used for selecting the RF supply for the four-fold split ring electrode S3 (PCI-Do.2, LO for dipole, HI for rotating wall) and for multiplexing the amplified resonator signals to the input of Rigol (PCI-Do.5, LO for an ARES, HI for CRES, SMA 18, HE 4; PCI-Do.4, LO for ARES CT, SMA 24, HI for ARES ST, SMA 20, HE 3).

The Watchdog can close contacts for Heater 1 and 2, individually. A Keithley 2700 multimeter reads out resistance values of the temperature sensors by a four-wire measurement, refining them from the significant resistance of the connecting wires.

4.9 The Laser System

Once the ion cloud has been prepared in the ST, it is irradiated with laser light from a TOPTICA DL 100 external-cavity diode laser in Littrow design, as seen in the lower right corner of the photograph in figure 4.24(b). It is specified with 12 mW output power at around 441 nm, of which up to 4 mW can be coupled into a fiber for spectroscopy with trapped Ar^{13+} ions. 40 % of this power can be measured at the other end of the fiber and presumably a similar transmission factor has to be considered for the coupling and the way down to the spectroscopy trap (cf. Sec. 4.10). With attenuator plates, the power can be reduced to around 30 nW, if necessary. In total, the laser can be tuned over a range of 439.6 to 441.8 nm, which corresponds to 3.4 THz and is by far sufficient for the 325 GHz broad range of Zeeman-split lines. This system can either run freely or be stabilized in frequency by an external reference. In the free-running mode of operation, it has a linewidth of 0.1 to 1 MHz on a 5 μs timescale. This is by far narrow enough to resolve the Zeeman splitting of many GHz. The module also features a mode-hop-free scan over an interval of up to 30 GHz. We use a triangular scan of the laser frequency with a span of 0.1 to 2 GHz and a scanning rate around 200 Hz for searching the transitions in argon ions.

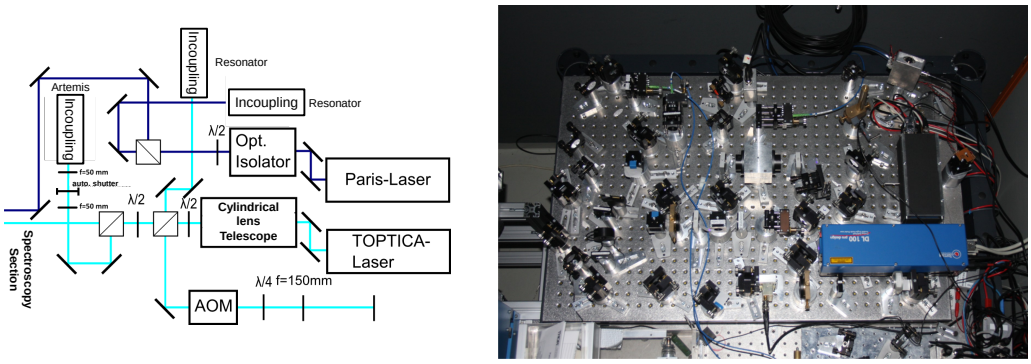

(a) Schematic of the stabilization chain.

(b) Optical table with master and spectroscopy laser.

Figure 4.24: Images of the laser stabilization system.

The group of Prof. G. Birkl at TU DA has implemented an external frequency-stabilization chain and set it up in a temperature-stabilized laser hut below the HITRAP platform, on which the magnet is standing. A home-made filter-stabilized external-cavity diode laser ('Paris configuration') runs at 453 nm and forms the 'master laser', the black rubber-foam box on the right of figure 4.24(b). It is stabilized with a LockIn-amp and a PI controller to an electronic transition of molecular tellurium ($^{130}Te_2$) by Doppler-free saturation spectroscopy in a heated vapor cell (not in the photograph). In the spectral region of our interest, this dimer has many transitions, on average 1 to 3 GHz apart, which have been measured to a very high precision and are listed in an atlas [SRHR05]. Part of the beam is coupled into a transfer cavity via an optical fiber—the couplers of master and slave laser to the fibers in blue coatings are depicted in the upper right corner of figure 4.24(b); the cavity cannot be seen. It has a rough length of 6.5 cm, resulting in a free spectral range (FSR, the spacing between longitudinal resonator modes) of 2.3 GHz. The precise cavity length is locked to the wavelength of the master laser, again with a LockIn-amp and a PI controller. For further details about the use of a transfer cavity for laser stabilization see,

e.g., [AAS+12].

The slave (i.e. spectroscopy) laser itself is divided into three branches with polarizing beam splitters. The largest fraction is guided to the optics flange of the magnet via a 27 m long single-mode fiber, the coupler is depicted in the upper middle of the photograph. The beam can be blocked by a mechanical shutter, seen in the lower left. Within the magnet, another fiber guides the wave towards the trap. This light path will be further discussed in the next section. Another part of the beam is sent into the tellurium spectroscopy cell for cross-checking the wavelength.

The third fraction is used for frequency stabilization to the transfer cavity, a Fabry-Pérot-Interferometer with the TOPTICA DigiLock110 system. The advantage of such an instrument is that master and slave laser can occupy different resonator modes and thus differ in frequency. In the present case, there are around 8000 FSR difference between the two frequencies. The influence of dispersion has been studied in [Alb14]. The largest effect in a temperature-stabilized lab comes from fluctuations in atmospheric pressure on the mbar scale and amounts to a few MHz scatter of the spectroscopy-laser frequency. The short-term stability is much better. A test measurement of a tellurium line could be reproduced with a precision of 0.2 MHz within a day [Vol14, p. 43] and 11 kHz systematic inaccuracy due to hysteresis. The same measurement revealed a day-to-day fluctuation of 4.8 MHz.

Before coupling the spectroscopy laser into the transfer cavity, it undergoes a frequency shift by passing twice through an acousto-optical modulator (AOM, double-pass configuration, shown below the TOPTICA laser in the photograph). This offers the possibility of 180 up to 320 MHz detuning between the spectroscopy-laser frequency and the frequency locked to a cavity fringe. For scanning of a broader range than these 140 MHz, the cavity arm can be stabilized to different longitudinal resonances. This extends the stabilization to the full tunable spectrum of the slave laser, however not continuously: the step size naturally given by the FSR is much larger than what can be bridged by the AOM.

In order to fill the gaps between adjacent fringes, the frequency of all modes can be varied in suitable steps: If the cavity is locked to the master laser with a different resonator mode, this slightly changes the FSR. The effect is multiplied by the high number of fringes between the two laser frequencies and results in a shift of 55 MHz in the region of 441 nm, if the cavity length is modified by one longitudinal resonator mode with respect to master laser frequency. The given setup allows a total range of about 10 μm variation in resonator length, corresponding to about 50 modes or 2.7 GHz. Now the stabilization covers the full spectrum of the spectroscopy laser, using a single tellurium line for stabilizing the master laser. This scheme has been established as a computer-controlled, reliable method in [Vol14].

A WAVEMASTER DS wavemeter from Coherent is used for rough manual adjustment. The accuracy of 8 GHz (1.5 GHz resolution) is insufficient for the actual wavelength determination. Calibration from interpolating between tellurium lines should be much better, at least the reference lines are specified with 1.1 MHz uncertainty in the atlas [SRHR05].

4.10 The Optics for Laser Spectroscopy

Light from the previously discussed spectroscopy laser is guided to the ions by optical fibers. Upon successful excitation, the upper state can decay spontaneously and emit fluorescence light.

This is transported out of the magnet vacuum chamber by an image guide and detected with a channel photomultiplier (CPM), attached to the optics flange. At this point, the magnetic field strength is below 50 G, which enables reliable operation of the multiplier (specified to 100 or 200 G). Illumination and observation are separated in time for the purpose of background suppression and in order to protect the sensitive detector from high intensity due to stray laser light (max. count rate is 10 MCt/s). The relatively long lifetime of 9.6 ms of the optical transition allows to implement such a scheme with mechanical shutters, electronic discrimination, signal lines of 27 m length, and HV switching.

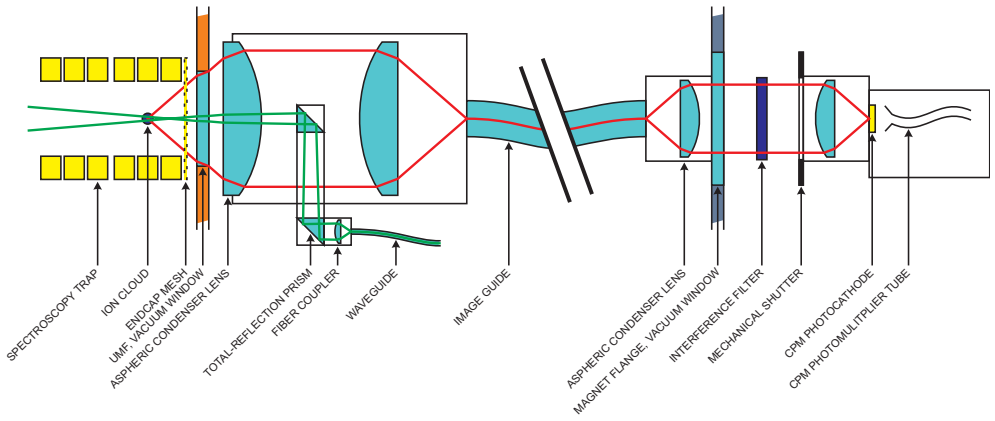

(a) Schematic drawing of the imaging system.

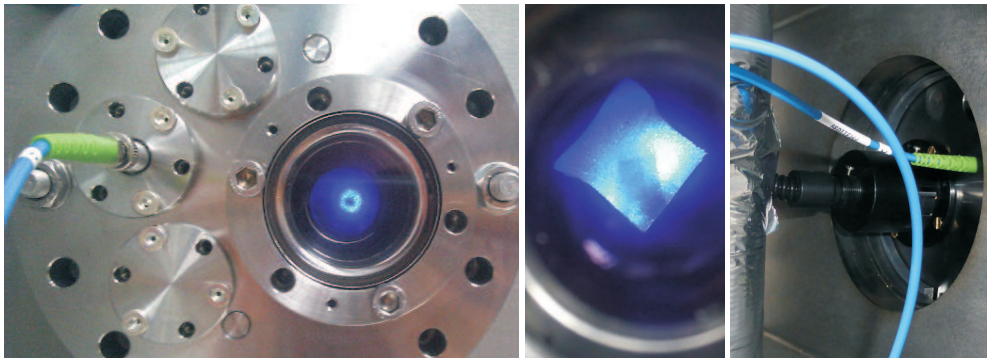

(b) Photographs of the optics flange. Left: from the outside, with the powered fiber from the laser lab. 2 CF16 flanges are foreseen for microwaves. Middle: zoomed and infinity-focused photograph of the open view port, with scattered light from the trap. Right: fiber and image guide with couplers inside the magnet chamber.

Figure 4.25: Images of the optical detection system.

The light path is depicted in figure 4.25(a). The fiber-optic waveguide is a continuation of the 27 m long fiber, connecting the setup in the laser lab (cf. Sec. 4.9) to the optics flange of the magnet (photograph in Fig. 4.25(b)). The beam (depicted in green) is coupled out of the fiber such that it converges and gets focused before arriving at the trap center by another collecting lens. At the place of the ions, the diverging beam has roughly 1 mm diameter. This should be sufficient for illuminating many ions. The beam is placed onto the symmetry axis by a pair of prisms (5 mm long edges). Their small size minimizes signal loss in the detection branch. Adjustment has been done in the warm and before completing the setup and cannot be corrected during the measurement.

This makes a rather large beam diameter at the place of ion cloud indispensable [Vol14].

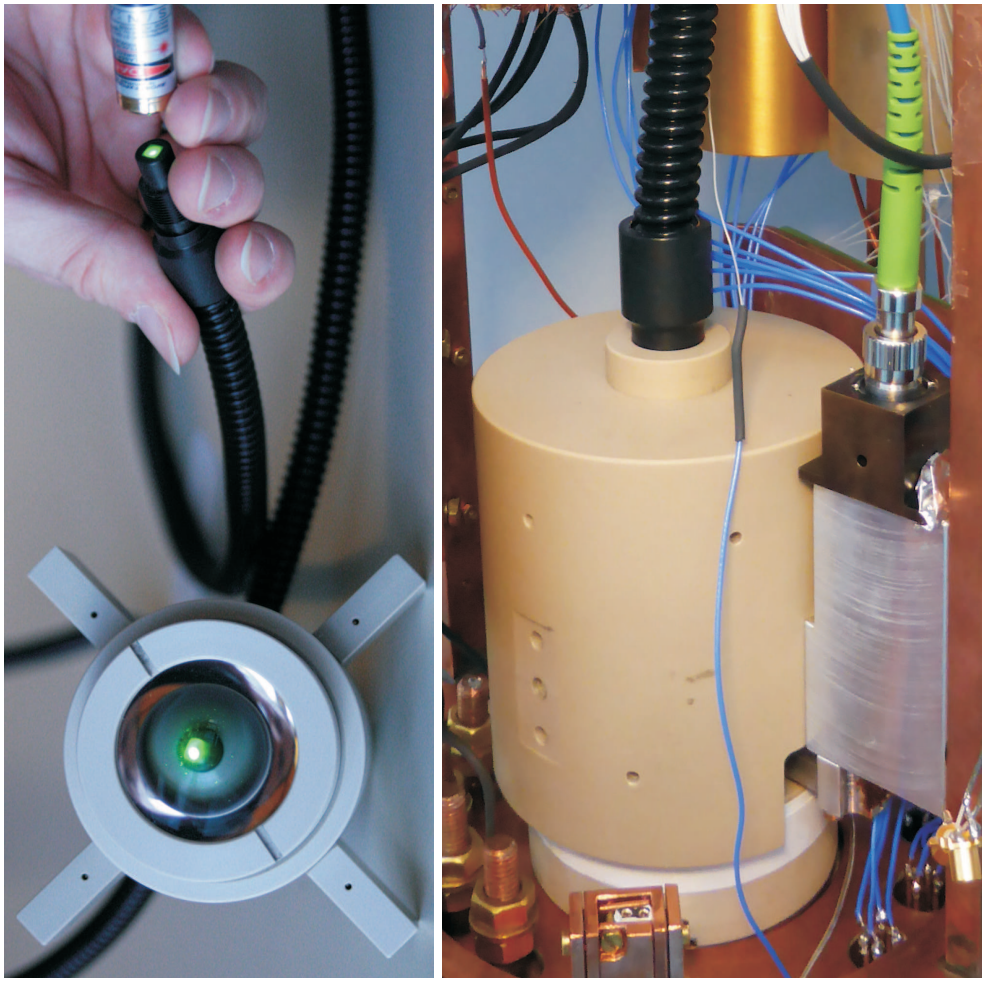

Figure 4.26: Lens holder with 2 condenser lenses and image guide mounted. Left: test with laser pointer. Right: additionally with fiber coupler and 2 prisms, mounted to 4-leg in final assembly (cf. Fig. 4.14(b)).

Ions in the trap center (their fluorescence light is drawn in red) are imaged onto the tip of a fiber bundle (image guide IG-154-72 by SCHOTT, Fig. 4.26) by a pair of aspheric condenser lenses (THORLABS ACL4532-A) with large numerical aperture (0.7), making use of the large solid angle of the trap (26.6° opening half-angle, cf. Sec. 4.3) and acceptance angle of the image guide (0.63 num. ap.). The choice for a pair of collimating lenses with a section of parallel beam in between is in favor of facilitating design and adjustment: The distance between lenses does not affect the image distance, and other components like the prism holder can be introduced in between. The image guide has 4 mm × 4 mm active area, again leaving some margin to compensate the lack of adjustability. It is 1.8 m long and ends in the focal plain of another aspheric condenser lens (THORLABS ACL2520-A) at the vacuum side of the optics flange. Hence the beam passes through the vacuum window with infinite focus, such that optical components can be placed into the path before refocusing the light to the detector. Currently we have an interference filter of 10 nm width about a center wavelength of 442 nm and another mechanical shutter. The device responds rather

slowly, namely with 9 ms delay and edge time, and a jitter of 0.1 ms.

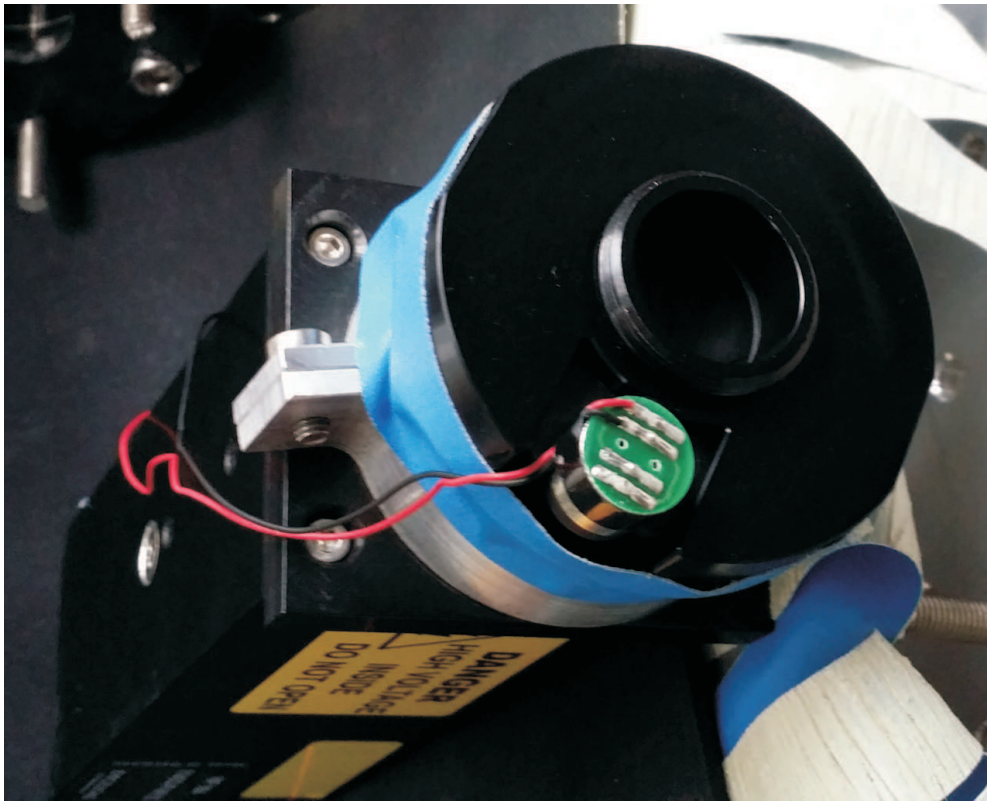

Figure 4.27: CPM module with lens and shutter mounted.

For photon detection we use an MP984 module by Excelitas (CPM, see Fig. 4.25(b)). This instrument contains a photomultiplier tube (PMT) with a 5 mm diameter borosilicate glass window, coated on the inside with a low-noise bialkali photocathode. The high voltages required for producing electron avalanches are generated inside the instrument depicted in figure 4.27. The counting module also comprises electronics for discriminating and shaping pulses. Thus it converts a detected photon into a TTL pulse (around 3 V high, 20 ns wide), with around 20 % quantum efficiency in the blue spectral range. The pulses are put out to a BNC socket and need to be terminated with 50 Ω. The module is supplied with 5 V (load is specified below 250 mA) via a (male) D-sub 9 socket, featuring further optional connections: A logic 'HV kill' input shuts down all high-voltage channels if actively grounded. This rather slow action can be used for safety, controlled by the interlock output of the WDG (cf. Sec. 4.5). A logic 'Gate' input blindfolds the CPM if supplied with a high signal. The cathode is set to +190 V within 100 ns. Reversion takes around 200 ns. An analog output signal ('Vmon') indicates the value of the high voltage (attenuated by 1000) and can be used for setting the multiplier gain.

Pulses are registered in a National Instruments PCI6602 counting card in 'CI (counter input) period' mode. An event is mapped to a timestamp relative to a trigger signal, marking the end of laser excitation. The scheme of excitation and detection introduced above is repeated several times ('bursts'). With the individual trigger, we can accumulate statistics and maintain the full timing information for later analysis.

Table 4.7: Optical excitation and detection efficiency and transmission of individual components.

Fract. of ions in spatial overlap with laser[3]	16 %
Fract. of ions in overlap with laser bandwidth[4]	≥ 2 %
Fract. of laser intensity in overlap with transition linewidth[5]	≥ 0.01 %
Fract. of ions in bright state	≥ 50 %
Total excitation efficiency (product)	$2 \cdot 10^{-7}$ to $3 \cdot 10^{-2}$
Weighted solid angle (fract. of 4π)	8 %
Transm. through mesh	60 %
Fract. of light not shaded by laser incoupling	80 %
Transm. through 2 windows	each 90 %
Transm. through 4 lenses	each 80 %
Fract. of light being focused to image guide	50 %
Transm. through image guide	50 %
Transm. through blue filter	75 %
Detector quantum efficiency	17 %
Total detection efficiency (product)	$4 \cdot 10^{-4}$

The CPM Gate input together with some outputs of a BNC Model 575 Delay / Pulse Generator are crucial for the timed measurement scheme. The signals are communicated between the laser lab and the magnet by three BNC lines, laid with the optical fiber. Two outputs control the mechanical laser shutter, causing it to turn on and off laser excitation on a timescale of 100 ms. Compared to the CPM shutter, the laser shutter is fast (4 ms delay, 0.02 ms edge time (with a focused laser beam), and 0.2 ms jitter), however by far not fast enough for our measurement. Therefore a feedback is needed for precise timing and detector protection. A small fraction of the beam is monitored by a photodiode (PD) and a discriminator circuit. Only if the shutter is intended to be closed and the PD measures sufficiently low intensity, a logic level is pulled down [Vol14]. A delay of 0.4 ms is added to the falling edge, then the signal is sent to the CPM Gate input for fast activation (and is high otherwise for protection of the PMT). And it serves as trigger for the beginning of a burst. Another output of the Delay / Pulse generator is used to close the mechanical shutter at the CPM. This signal is sent ahead of blocking the laser, in order to overcome the delayed shutter action and not to lose valuable time. It rather serves for protection against long-term exposure of the photocathode.

We estimate the sources of signal loss, expressed in terms of efficiency factors, in table 4.7. The first part discusses excitation—explanation is given in footnotes. These factors are however not fix: With a scanning measurement, fraction of Lamb-Dicke bands can be enhanced significantly; by matching the laser intensity to the loss due to natural linewidth, the third factor is overcome, as well; and by optical pumping, a much higher fraction of population can be transferred to the

[3] With an assumed ion cloud diameter of 2 mm and a measured laser beam diameter of around 1 mm. The cloud diameter can be sufficiently reduced by the rotating-wall technique [BVST12, BHM+93]

[4] With a Doppler width of around 60 MHz and 800 kHz band spacing, we expect around 2 % if all ions in one of the central Lamb-Dicke bands—and maybe the laser covers several bands with its spectral width Γ_L of around a MHz.

[5] This factor accounts for laser power wasted in the deep gaps between Lamb-Dicke bands, each only $\Gamma_I = 110$ Hz wide. An ion can absorb only a fraction of around Γ_I/Γ_L, unless the transition is saturated by driving Rabi oscillations with $\Omega_R \geq \Gamma_L$, which in the present case requires several mW/(mm)^2.

bright state. With these numbers we expect a total efficiency of up to $4 \cdot 10^{-4}$ for exciting an ion and detecting the emitted photon, depending on laser intensity. The narrow-band saturation intensity of a transition at 680 THz frequency and 110 Hz width is

$$h\nu \left(\frac{\nu}{c}\right)^2 \Gamma_I = 2.5 \cdot 10^{-4}\,\mathrm{W/m^2}.$$

Multiplied with the laser-width loss, we obtain an intensity of $2.5\,\mathrm{W/m^2}$ for a reasonable transition probability within the exited-state lifetime. This corresponds to around $2\,\mu$W laser power in a beam with 1 mm diameter.

Assuming that 10^5 ions are trapped and fluoresce with a time constant of 9.6 ms, the ion-signal count rate at the beginning of a burst (peak) would be $R_s = 1\,\mathrm{mCt/s}$ up to $0.1\,\mathrm{kCt/s}$. This count rate competes with other exponentially-decaying signals with time constants in the range of a few ms, as reported in section 5.8. This background signal responds proportionally to the illuminating laser power and could be reproduced even with the master laser. The blue interference filter suppressed this background level by a factor of around 15, rescaled with the laser power. Apparently there is something in our apparatus which delivers slow broad-band fluorescence upon irradiation with any blue light. At a laser power of 2.3 mW (before coupling into the fiber), the filtered background peak count rate is $R_b = 1.3\,\mathrm{kCt/s}$ on average and in most cases below $3\,\mathrm{kCt/s}$. With $70\,\mu$W, the exponentially decaying background is almost invisible, and only some constant background at a level of $0.8\,\mathrm{Ct/s}$ remains. Another filter with narrower bandwidth is being discussed to further reduce this source of background.

Signal counts should exceed 5 times the background noise, which is the square root of the mean amount, if the background follows Poisson statistics. With the given count rates, this can be satisfied by extending the observation time:

$$\begin{aligned} t \cdot R_s &\geq 5\sqrt{t \cdot R_b} \\ t \cdot 0.1\,\mathrm{kCt/s} &\geq 5\sqrt{t \cdot 1.3\,\mathrm{kCt/s}} \\ \Rightarrow t &\geq 3.3\,\mathrm{s} \end{aligned}$$

Assuming that only the first 10 ms of a burst yield useful signal, each wavelength should be measured with 330 bursts. Up to a certain level of saturation, also higher excitation intensity pays off—beyond this, the background strength is raised more than the ion signal.

Additional information could in principle be derived from the timing of events. For instance, a constant background is discriminated from the ion signal rather easily by fitting an exponential-plus-offset function to the data. (In addition, this signal could be reduced by shading the detector from stray daylight.) But the similarity in time constants of the two exponentials makes this very difficult. An improvement on the measured lifetime (table 2.4) cannot be expected.

Chapter 5

Experimental Procedure

– How we realize a measurement –

A successful measurement requires preparation of ions, as well as electronic detection and spectroscopy with them. The goal of preparation is to deliver a cold, dense, pure cloud of $^{40}Ar^{13+}$ ions in the spectroscopy trap. To be precise, we aim at 10^5 ions at 4 K, occupying a volume with 1 mm radius around the ST center and below 10^3 contaminants of other species. The methods of choice combine the components presented in chapter 4 and are symbolized in figure 5.1: electron-impact ionization of small amounts of injected gas (details in Sec. 5.1), resistive cooling (Sec. 5.5), cleaning, and transport (Sec. 5.6). The general procedure is symbolized in figure 5.1: In step *a*, negative high voltage produces and confines ions, while a weaker positive well (creation trap) traps ions. In *b*, some ions are kept in the harmonic potential of CT, where they can get cooled, while others are being transported (potential minimum between the traps) to ST, where they eventually get stored in a harmonic potential, seen in step *c*. To this end we can modify many parameters, such as gas

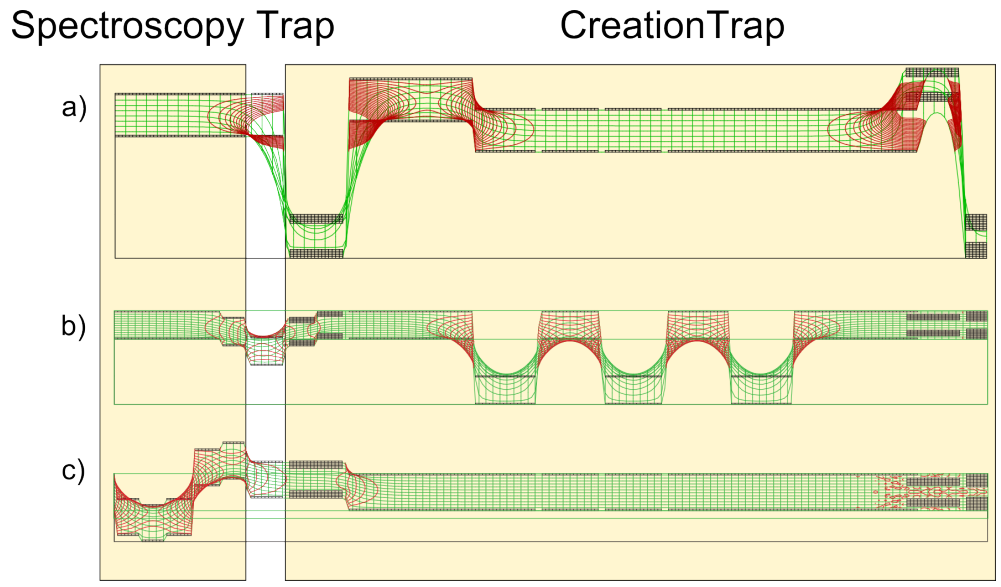

Figure 5.1: The procedure of ion preparation, shown as a sequence of sets of electrode biases. The resulting electrostatic potentials have been simulated with SIMION.

pressure and oven temperature (see explanations in the previous chapter and following sections), electron energy and current, cooling time and trap depth, RF power and application time, just to name the most important ones. The precise timing of detection and the sequences of transport procedures have also proven to be critical.

Once a cloud of $^{40}Ar^{13+}$ ions has been prepared adequately in the spectroscopy trap, the actual measurement can be performed. As outlined in chapter 3, two ingredients are required for the determination of magnetic properties: One is the energy shifts according to equation 2.6, as represented in linear combinations of optical frequencies (see Eqns. 3.3, 3.7, and 3.9). In a later stage, the transitions between Zeeman sub-levels of different M_J are directly driven by microwave radiation, in order to measure the B-field-dependent splittings with sub-Hz resolution. As a second ingredient, the magnetic field is calibrated by measuring the motional frequencies (Eqns. 3.13, 3.14 and 3.20).

This chapter is dedicated to the experimental implementation. We have conceived working principles for all steps of ion preparation. These will be presented in the following sections, alongside with results of the steps achieved so far.

5.1 A Miniature EBIT

Ar^{13+} ions are produced by electron-impact ionization above an electron energy of 0.7 keV, which and can be done inside our trap chamber, by a miniature electron-beam ion source (EBIT). The setup, working principle, and tests shall be briefly explained here and in the following sections. The underlying processes of field emission and impact ionization have been discussed in great detail in the PhD thesis of J. Alonso Otamendi [Alo07], who built and operated a very similar ion source for another cryogenic Penning trap. Main differences are the internal target and thus better vacuum and the type of electron source. The sources of electrons and atoms, used for ARTEMIS,

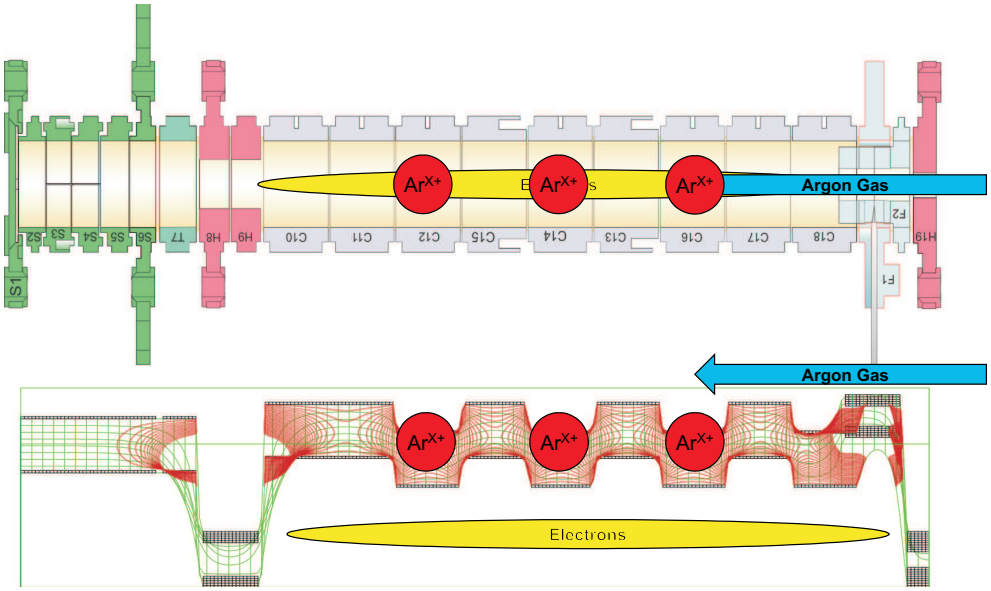

Figure 5.2: The procedure of ion creation, indicated by the set of electrode biases. The resulting electrostatic potential has been simulated with SIMION.

have been presented in sections 4.4 and 4.5. Their design and further considerations of operation are reported in [Lin10].

Argon gas is injected into the creation trap (cf. Sec. 4.3) through the cryogenic gas valve, while electrons from the FEP are moving at high energy inside the well, formed by the reflectors, as indicated in figure 5.2. In colliding with these electrons, atoms get ionized. As charged particles, they are now confined by the electric and magnetic fields of the capture trap. Ongoing electron impact further ionizes the particles (charge breeding), until an equilibrium of ionization, recombination and several other loss mechanisms is reached, see [Alo07] and references therein. Section 5.4 will present some charge-state distributions that could be obtained with our setup.

The final ion-species spectrum after breeding depends on the settings of the electron source. Each element has a sequence of energy thresholds for the degree of ionization (ionization potentials). Values for the most relevant atmospheric elements, as well as our candidate argon are plotted in figure 5.3. Many of the measured spectra can be interpreted, if only oxygen and hydrogen are included besides argon. Hydrogen is not depicted, because with the low potential of 13.6 eV it is always ionized. The 1s-shell of argon is opened only with 4.1 keV, which is not in the plot, either.

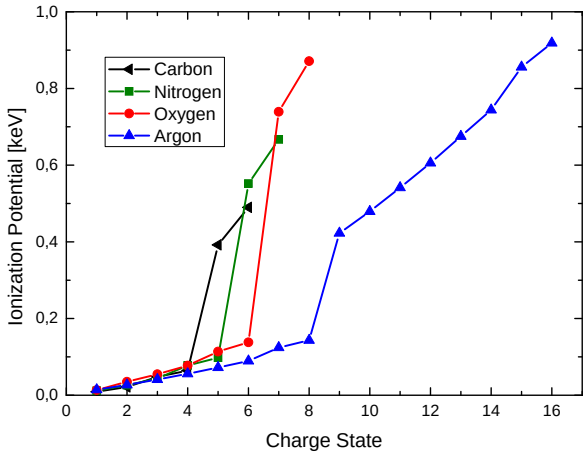

Figure 5.3: Ionization potentials of carbon, nitrogen, oxygen, and argon, from the DITHER database [Cre10].

For creating Ar^{13+}, the energy of incident electrons needs to be at least around 0.69 keV, while 0.76 keV allows production of Ar^{14+}. Production close to the threshold is rather slow: With 0.75 keV, the rate is $5 \cdot 10^{-3}\,s^{-1}$ (with an assumed electron density of $10^9\,cm^{-3}$); the maximum of $0.3\,s^{-1}$ is reached at 3.3 keV. While the electron beam is turned on, the distribution evolves toward the theoretical maximum—the higher the current, the faster the evolution. In the simplest case (without recombination with electrons and charge exchange with residual-gas atoms), this process is continued until all particles have reached the threshold charge state. Only the product of current density (j) and duration (τ) would determine how far the population climbs towards the maximum, as depicted in an example figure 5.4, calculated by CBSIM [Mar10].

This means that we can either apply a high current density for a few minutes shortly below the

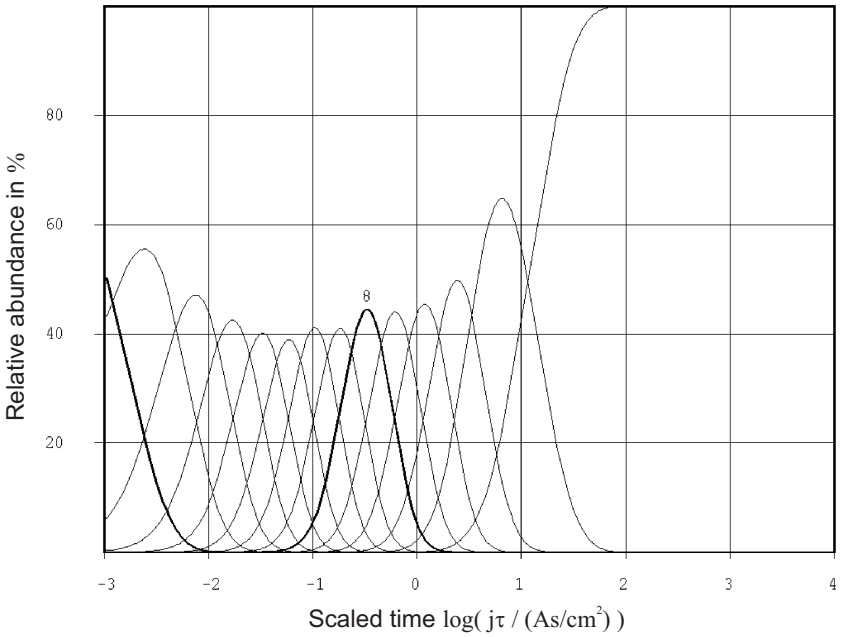

Figure 5.4: Charge breeding of argon at 750 eV impact energy, simulated with CBSIM: While for early (scaled) times, we obtain a rich distribution of charge states, it later converges to a almost pure cloud of Ar^{13+}.

threshold of Ar^{14+}, or attempt faster production with higher energy, at the price of a rich charge-state spectrum, which must be cleaned afterwards. The CBSIM [BKS06] calculations indicate a value of 1.855 keV for minimum production time of Ar^{13+} [Mar10]. As mentioned before, the electron energy cannot be accurately identified with the FEP voltage. The alternating CT potential modifies the energy, and ions, especially when hot, are not only trapped in the minima. Charge density of electrons and ions further modifies the potential considerably. For instance, we observed the FEP emission breaking down in some cases, and confinement in the reflectron being lost in other conditions, both due to space-charge potential. However, values around −1 kV FEP voltage should be reasonable.

5.2 Verification Methods of Ion Production

Performance of the procedures introduced in this chapter is measured by three detection schemes: The Faraday cup (FC), mentioned in section 4.3, the CPM detector from section 4.10, and the ARES CT, as introduced in section 4.6. Their operation is explained in this part. The CPM and FC acquire time-resolved production data and are very useful for first tests of injection. They can however not distinguish between the large variety of signal sources. The axial-resonance method is rather complementary: the trap content can be analyzed specifically, but the measurement takes at least some minutes subsequent to production.

5.2.1 Faraday Cup Current

The meshed endcap electrode S1 is connected to a KEITHLEY 617 multimeter in charge-measuring mode with sub-pC resolution. A trace of around a hundred samples, measured every 0.3 s (maximum rate) is recorded. In this Faraday-cup (FC) configuration, it monitors the integrated current impinging on the mesh—may it consist of electrons or ions. The arising currents resp. charges are very low (sub-nA / -nC scale), such that they are often covered by leakage currents and the charging up of finite resistances and capacities, respectively, in the trap wiring. We investigated these effects in an earlier stage of the experiment, when the trap was not yet filtered: Switching electrodes of the CT by several hundreds of volts results in a reversible charge pulse of 30 pC within a second, which corresponds to around 0.1 pF capacitance—a very reasonable number. Besides the charge pulse, a constant current of 11 pA arises from the changed trap biasing, equivalent to an insulation of 25 GΩ between distant electrodes. This is not surprising, either, and together with the aforementioned capacitance reproduces the charge-up time constant of a second. Now, with filters in place, all electrodes (except for the HV ones) are connected with each other by identifying resistances (cf. Sec. 4.7) versus GND, which have values of 1 GΩ or below, permitting even higher offset currents.

These effects must be avoided or compensated for any FC measurement. The amount of channels for switching should be kept as low as possible and the timing must be reproducible. The current directly before switching is monitored by starting a charge measurement a few seconds before the actual procedure. The observed slope (nowadays in the range of 0.3 nA) is subtracted from the data. This so-called 'slope correction' is sufficient if no charging-up of capacities is to be expected, and was successfully employed in the injection measurements reported below.

If capacities are involved, the switching needs to be undone after the measurement and the total measured charge pulse to be corrected by the observed switching pulse. The modified offset current in the time while the alternative biasing is applied can either be accounted for by a reference measurement, or by leaving the settings for another few seconds, determining the asymptote, and integrating the additional current over time. This method would in principle allow us to analyze the integral charge of stored ions by dumping the cloud into the endcap. However, it did not produce conclusive results when we first tried it in 2013, therefore it was not implemented in the current phase.

5.2.2 Photon Yield

The optical single-photon detector (CPM, channel photomultiplier) records any light coming from the trap chamber through the image guide to the optics flange of the magnet vacuum chamber. Signal can originate from the decay of atomic levels, excited by electron impact, as well as from recombination of ions with electrons from other particles or trap walls. Another source of light is bremsstrahlung from electrons hitting the FC. This instrument is used simultaneously with the FC during ion creation. The data acquisition is set to count all pulses. Every 0.3 s, the accumulated number is requested and converted to a count rate in software.

5.2.3 Axial Resonance

Trapped ions are selectively brought in 'contact' (i.e. resonance) with the axial resonator attached to the creation trap (ARES CT), by matching the trap voltage to the ion mass-to-charge ratio, according to equation 3.13. This relation can expressed in terms of voltage,

$$U_{\mathrm{res}} = \frac{(2\pi\,\nu_{LC}\,d)^2}{2\,c_2}\,\frac{M}{Q}, \tag{5.1}$$

which is then proportional to the mass-to-charge ratio—or, more precisely, to the 'apparent M/Q', modified by frequency shifts, as discussed in section 3.3. c_2 is the quadratic Taylor coefficient and d the characteristic dimension of the trap (cf. Sec. 4.3). If the resonance condition is satisfied, motional energy of the ions is transferred to the tuned circuit (Sec. 4.6) and thus raises the signal level in the detection system, see section 3.4. The recorded signal strength is a measure for energy dissipated into the resonator and thus for the amount and energy of ions of a particular M/Q.

We use the ramping technique to complete this scan in a minimum amount of time: The trap voltage supply (HV 250-8) is either set to alternating voltages or with a superimposed deep well (cf. Sec. 4.3), and controlled by an external reference voltage for fast proportional ramping of all channels. After the RIGOL spectrum analyzer is set to zero-span mode at the peak frequency of the respective resonator (with a reasonable resolution / video bandwidth—currently we mostly use 1 kHz for axial resonators), a loop is started for the individual voltages of the scan. The set of voltages is given by first and last voltage (always starting with a deep trap, high absolute value) and a step size. We specify a voltage-step size equivalent with the dimension of a frequency. It is the amount by which the oscillation frequency of a resonant ion would shift in one step and is usually chosen smaller than the bandwidth to make sure no ion is missed. As mentioned several times, the voltage required for resonance depends quadratically on the frequency, therefore the absolute voltage step size is calculated as

$$\Delta U = 2U\frac{\Delta\nu}{\nu_{LC}}$$

and subtracted from the previous value.

If this set is executed with uniform timing, this leads to an exponential curve with equal contact times for all ions. The voltage array is then given to the inner measurement loop. In each step, the value for the reference is requested and the trace of RIGOL spectrum analyzer is retrieved, containing 600 samples of the most recent 100 ms. We store the mean value and standard deviation of the amplified signal level together with the voltage (nominal reference in case of CT, which is the ring voltage divided by −50; ring voltage in case of ST).

5.3 Gas Injection

As the first step of optimizing ion production, we need to find working parameters of the gas source, using electron-impact ionization and the on-line CPM and FC data as benchmark. To this end, we prepare the CT in a trapping state and the electron source in reflectron mode (HV Switch On), with −0.35 kV FEP and +1.00 kV relative accelerator voltage (the reflector is always

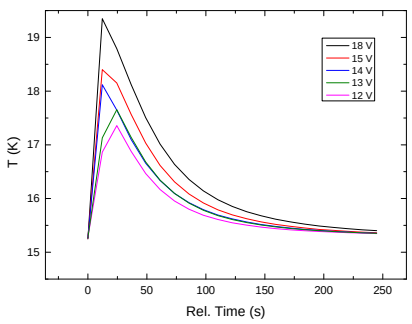

(a) Temperature rise and fall over 4 min upon heating.

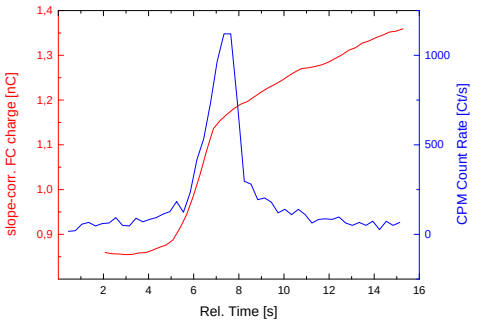

(b) Charge and CPM count within a few seconds around heating with 12 V.

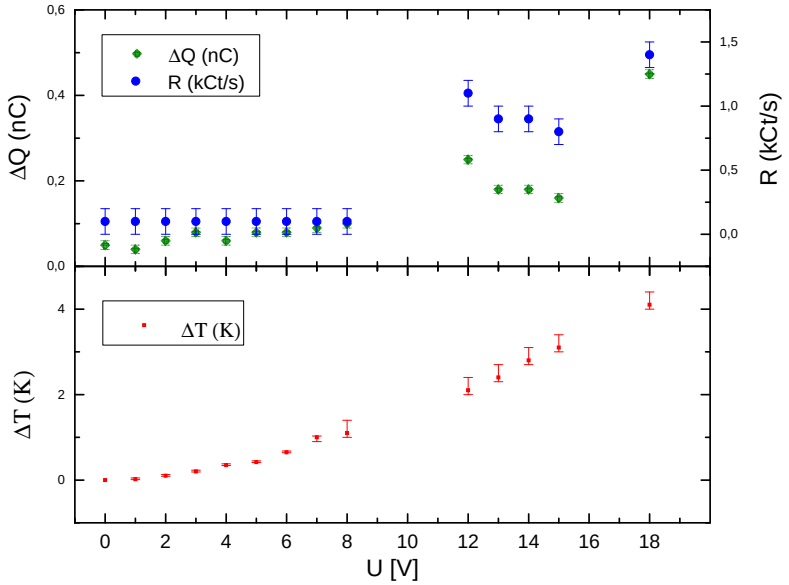

(c) Peak values of temperature, charge pulse and CPM count rate for all voltages.

Figure 5.5: Records from heating the gas source with different voltages for 3 s.

requested 0.4 kV more negative than FEP to ensure electron confinement. Earlier tests had shown that a reflector voltage far below −2 kV is not desirable, because the trapping condition (Eqn. 3.18) can locally be violated for low charge states. With these settings, we don't expect charge states higher than O^{6+}, N^{5+}, bare carbon (C^{6+}), and Ar^{11+}. But initial ionization is more efficient with lower impact energy. Then we trigger the on-line monitors to measure for around 15 s and after 5 s request injection from the gas source. The electron source is turned off 60 s after the pulse, ions are concentrated to the center electrode E14, and a ramp scan is taken with axial resonance in the creation trap.

In spite of the tests reported in section 4.5, we found that no detectable amount of ions was produced with analogous settings. After trying a lot with short pressure pulses through the cryogenic valve at low temperature, we raised the heating voltage in steps of 1 V up to 18 V at

the backup (secondary) heater, applied for 3 s. Repetition time of the temperature measurement is too slow to resolve the maximum value (Fig. 5.5(a)), but we see that the oven temperature rose from an equilibrium of 15.3 K at least to 19.4 K in case of 18 V heater voltage. In these measurements we left out the pressure pulse, because we wanted to change one parameter at a time in order not to flood the complete trap chamber. And after many gas pulses there must have been a lot of frozen argon in the oven—this would be the 'gas source' mode of operation. The CT state for the earlier measurements (0 to 9 V, of which the last two failed) was a large potential well ($+-------+250\,\mathrm{V}$, i.e. $U_{\mathrm{E10}} = +250\,\mathrm{V}$, $U_{\mathrm{E11}} = -250\,\mathrm{V}$, ..., $U_{\mathrm{E18}} = +250\,\mathrm{V}$). We continued the measurement a few hours later up to 18 V, repeating 8 and 9 V, with a harmonic potential in CT ($++-+-+-++250\,\mathrm{V}$).

In case of lower temperature, the count rate hardly exceeds the background of around 0.1 kCt/s due to bremsstrahlung and stray light. The offset FC current is determined from the first 5 s (values around $3.2 \cdot 10^{-10}$ C per time step of 0.3 s) and subtracted from the raw data in the evaluation. In this case, not much electric switching is required, which could affect the FC measurement. The pressurized air is guided to the apparatus from the solenoid valve by an insulating hose, so the solenoid only has contact via the WDG crate. The insulation of the secondary heater is very fragile and sometimes there is ohmic contact with the trap chamber, but this is well grounded. Other than that, the insulated wires between the magnet feedthrough and experimental core might enable crosstalk—but that should be lower than the capacitive coupling via a common filter GND for trap electrodes.

Figure 5.5(b) shows the time-resolved data of FC and CPM from the iteration with 12 V. The FC trace is already corrected by a slope of $-3.17 \cdot 10^{-10}$ (Coulomb per time step), and we observe a charge pulse of 0.25(1) nC height within 2 s plus a changed current with ca. 0.25 nC for the following 10 s. The CPM count rate can be read more directly and we note 1.1(1) kCt/s peak count rate. The estimated temperature increase ΔT, charge pulse ΔQ, and peak count rate R from the entire series are plotted against the heater voltage U in fig 5.5(c). Sometimes the heater relay doesn't get closed, or the CPM doesn't count in the first 5 s, which is correlated with a giant jump in current. This is explained by the WDG having fired and thus turned CPM and HV off. The command for the heater relay retriggers the WDG and the CPM starts measuring. Likewise, the electron source is instantly set to high voltage, which leads to the charge pulse in the FC. In the successful turns, the temperature gain scales roughly quadratically with the voltage applied to the 0.3 kΩ heater. From an extrapolated value of 2.8 K at 14 V (2.0 J) we can derive a heat capacity of 0.7 J/K. The decay time constant around 100 s suggests an effective thermal conductivity of 7 mW/K. Charge pulse and count rate consistently feature a falling slope between 12 and 15 V, which could be an aging effect due to depletion of the source. The significantly higher temperature at 18 V might have lead to a more efficient gas release, perhaps also of other gas types. Such a baking should be done from time to time, otherwise the oven may be clogged. From then on, heating (with 13 V at the primary or secondary heater for 6 s) is immediately followed by an argon-gas pulse (of 54 ms duration and between 0.1 and 2 mbar prechamber pressure, adjusted manually as explained in Sec 4.5).

The CT is set to a harmonic potential (nowadays the outermost electrodes are also set to the design values, resulting in the biasing $-+-+-+-+-250\,\mathrm{V}$) and the electron source is run with around 1 kV accelerator voltage for 2 to 5 min in reflectron mode. This long duration is

chosen to make sure that ions are bred to high charge states and are not charged down by neutral atoms coming from the oven before it thermalizes. In later studies we mostly varied the FEP voltage between −0.3 and −1.7 kV, while the reflector is still 0.4 kV more negative. These settings are applied uniformly during injection and breeding (cf. Sec. 5.4). Creation efficiency could be enhanced by setting the FEP voltage in two steps: A low value around one hundred volts results in a rate of roughly $30\,\mathrm{s}^{-1}$ for initial ionization (with 0.75 keV impact energy, efficiency is a factor 3 lower [Lin10, p. 36]). With the trap in harmonic mode (±0.2 kV on axis), the actual FEP voltage only needs to be slightly below −0.2 kV in order to overcome the CT minima—in the maxima, the kinetic energy will be more than sufficient. After enough singly charged ions are trapped, the electron source could be set to more negative voltage in order to reach the desired charge state.

After turning off the electron source, ions are concentrated to E14. This sequence is considered useful and we found it to produce a good amount of ions. We also noticed that for several weeks after gas injection, we could produce ions just by turning on the electron source. We interpret this as sputtering from covered electrode surfaces. This might be a hint that we inject too much gas. Also the observation of fast clogging quests for further systematic studies. A replacement of the gas injection system (prechamber) is under way, offering remote control beyond the pulse duration of the shutoff valve. Together with a more stable version of the watchdog, the creation settings will be optimized in future.

5.4 Charge Breeding

The next step of optimization was varying the settings of the electron source for charge breeding. Since the FEP starts firing several 100 nA current shortly below 1 kV accelerator voltage (Sec. 4.4), we chose values in the range of 0.8 to 1.1 kV, with the FEP at −1.0 kV. Every iteration starts with dumping the trap and injects gas with the above found settings 13 V at the secondary heater for 6 s, followed by a 54 ms long pulse of 0.9 mbar argon into the harmonic CT with electron source running in reflectron mode. Ions are bred for 3 min, concentrated to E14 and measured with a ramp from 1 to 0.26 V reference voltage with 300 Hz step size equivalent. Figure 5.6 shows the resulting voltage spectra, mapping the average signal strength against the applied external reference ('Ramp Voltage'). Signal starts rising at 0.825 kV. At 0.925 and 0.950 kV we can discern multiple peaks, which can be identified as Ar^{8+} through Ar^{14+}, with a high signal for Ar^{13+}, and highly charged atmospheric ions ($M/Q \approx 2$, assigned with oxygen, but it could also be other light elements). Ar^{13+} should appear at 0.403 V reference voltage and the others at voltages proportional to their M/Q. The pattern seems however shifted by 75 mV to higher voltages, which is in agreement with the cloud-size-dependent negative frequency shift, determined in section 3.3. A lower frequency can be compensated by higher voltage. Around 1.000 kV, a single hump is dominant, which might be Ar^{15+}, according to the ionization potentials and extrapolation from lower voltages. It gets pronounced more with higher voltage and shifts a little.

At this point I want to remark that the charge-state identifications presented in this chapter in most cases assume a uniform shift in voltage for all simultaneously stored species, even over large distances. This is often consistently possible and is roughly in agreement with the prediction based on the ionization threshold. To our knowledge, there is, however, no reliable theoretical justification for this method, and in the trace for −1.4 kV in figure 5.7(b), for instance, where we

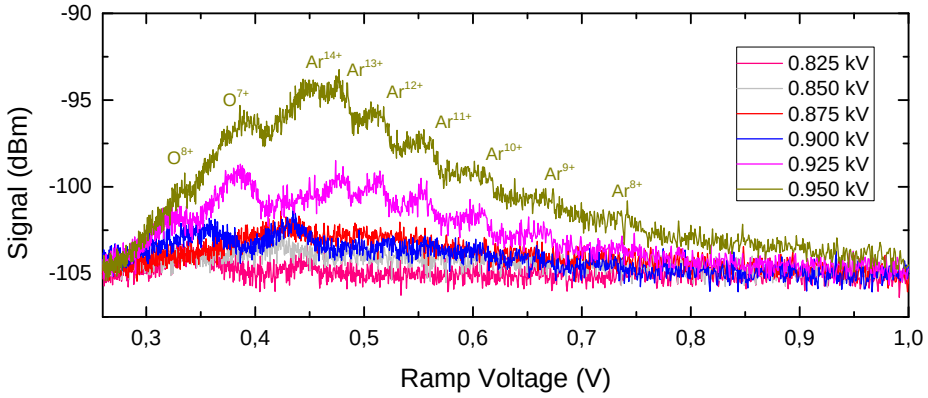

(a) Low electron current.

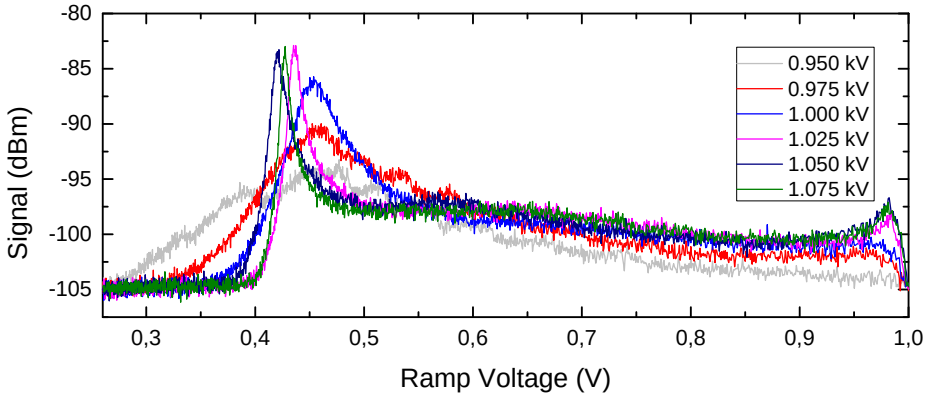

(b) High electron current.

Figure 5.6: CT ramps after production with different accelerator voltages.

suppose the highest possible argon charge states (up to heliumlike Ar^{16+}, according to Fig. 5.3). This would violate the constant-spacing argument. Shifts due to space-charge potential of other species are also not included in this reasoning. Much more precise and accurate identification would be possible with the ion-cyclotron-resonance (ICR) method, see e.g. [Alo07]. We tried several times to excite radial motion with resonant RF radiation, and to detect an increase in axial signal. But this could so far not be achieved.

Motivated by the outcome of the test with different accelerator voltages, we used 1.0 kV for investigating the effect of FEP voltage in the range of -0.5 through -1.5 kV. The procedure was the same as before, except that we used the primary heater instead of the bake-out heater. The results are shown in figure 5.7.

With increasingly negative ('high') voltage (but still in the lower regime, Fig. 5.7(a)), we observe two remote groups that approach each other, until they unite at -0.9 kV (or the left one disappeared). The average signal strength tends to rise, which can be due to more ions or higher temperature or both. Based on the spacing and threshold arguments, we identify the group at higher ramp voltage as argon charge states, the degree of ionization increasing with electron energy. This is also confirmed by repeated measurements with the same ion clouds, see section 5.5. The

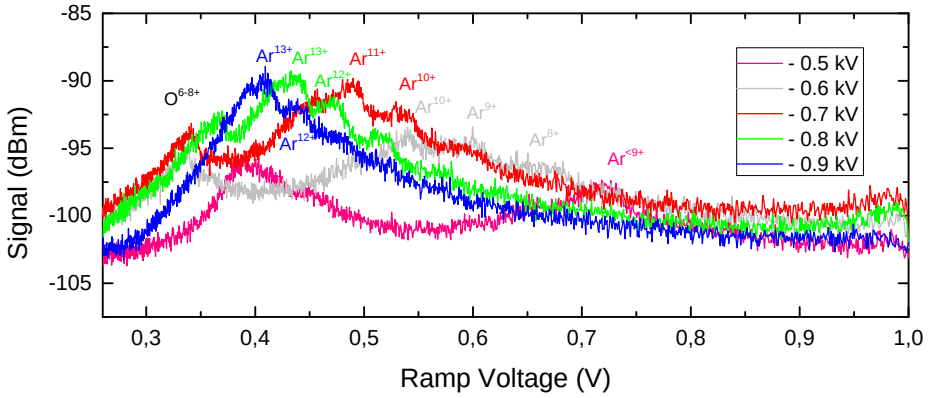

(a) Low electron energy.

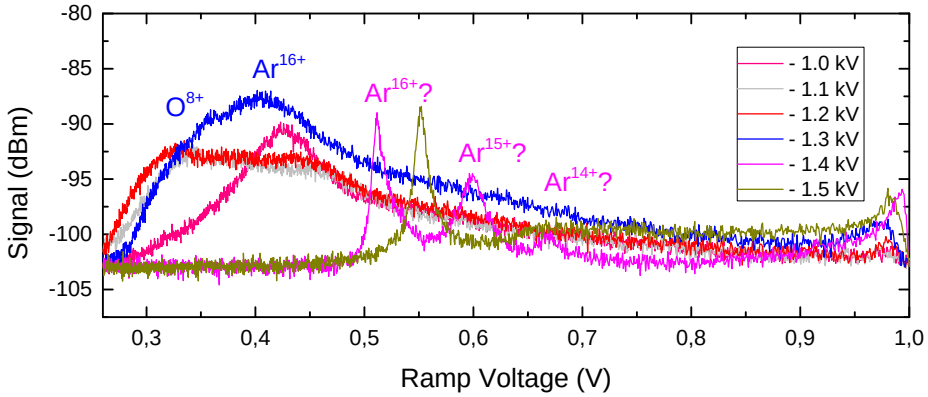

(b) High electron energy.

Figure 5.7: CT ramps after production with different FEP voltages.

signal at lower ramp voltage is interpreted as atmospheric elements (nitrogen, oxygen, or carbon, which might also come from oil in the RV pump), abbreviated with O^{6-8+}.

In the higher regime (Fig. 5.7(b)), the atmospheric feature occurs again (except at $-1.0\,\mathrm{kV}$) and blurs out the hump assigned to Ar^{16+}. Voltages of -1.4 and $-1.5\,\mathrm{kV}$ produce a very different situation: rather narrow, remote peaks, which are probably strongly shifted, but not with uniform spacing. As mentioned above, these peaks are hard to identify by the ramp voltage (apparent M/Q), but could be interpreted as highly charged argon.

From these measurements we conclude that the distribution of argon charge states reaches the desired degree of 13+ around $-0.8(1)\,\mathrm{kV}$ FEP voltage, in perfect agreement with the prediction from the ionization potentials. The current density produced by $1.0\,\mathrm{kV}$ (relative) accelerator voltage in reflectron mode (with reflectors $0.4\,\mathrm{kV}$ more negative than the FEP) is sufficient to create considerable amounts of highly charged ions within a few minutes.

In further tests we still often varied the FEP voltage and still saw many surprises. Weather creation results in smeared-out humps (as for FEP voltages around $-1.2\,\mathrm{kV}$), or narrower single (above $1.025\,\mathrm{kV}$ accelerator voltage in Fig. 5.6(b)) or multiple ($-1.4\,\mathrm{keV}$ FEP voltage and more negative in Fig. 5.7(b)) peaks depends rather critically on some parameters, especially the ac-

celerator voltage, even though the presented measurements at 0.950 and 1.05 kV could be very closely reproduced on the next day. When the FEP got a little degraded, we changed it to 1.1 kV. The setting for this channel should be revised every now and then, because eventually not the accelerator voltage but the FEP current is the relevant parameter for production time, and the current depends critically on the set voltage and the shape of the tip.

5.5 Ion Cooling

More light is shed on the question how to produce a dense, pure cloud by repeated observation of the ions over time, with different methods of cooling. After electron bombardment at around 1 keV kinetic energy per electron, the ion cloud is very hot. During creation in a harmonic trap, the temperature is limited by the confinement of around 0.3 kV, which is equivalent to 4.2 keV for Ar^{13+}. As a rule of thumb, one third of this well depth can be assumed as upper bound of the thermal energy,

$$k_B T \leq \frac{1}{3} |c_0 \, Q \, U_r|. \tag{5.2}$$

c_0 is again the Taylor coefficient relating the applied voltage to the potential on axis. In case of the CT, it needs to be redefined another time: Now it is doubled to 1.2, because the anti-traps are biased with the opposite of the ring voltage (cf. Sec. 4.3). One third, 1.4 keV, is roughly the electron energy, so we can assume that most of the created Ar^{13+} is confined. Still, this thermal energy would correspond to a temperature of $1.6 \cdot 10^7$ K and the Doppler width of 130 GHz would strongly blur the optical resonance, as in case of the Heidelberg EBIT, before ions cool down [MKB+11].

With our CT ramp technique, we have observed three signatures of cooling with a large variety of time constants: Off-resonant cooling of very hot ions within some 10 s, sweeping over resonance with effective energy dissipation for up to 10 min, depending on the ramping rate, and adaptive cooling with residual effects even after many hours. All of these methods use the mechanism of resistive or 'bolometric' cooling, where energy is transferred from ion motion into the resonant circuit, as discussed in section 3.4.

Other options would be sympathetic cooling by other trapped charged particles. The most relevant choices would be electrons, cooled by synchrotron radiation [Mae08], or laser-cooled singly charged Mg or Be ions. Of course, there is also sympathetic cooling among co-trapped resistively cooled ions, which might be a reason why we did not so far manage to clean our cloud. The excitation must be faster than the energy transfer in the cloud. Another mechanism is evaporative cooling. This by definition goes along with particle loss, and the electronic signal from the ions depends on both the number and temperature. Therefore we cannot clearly distinguish between cooling and losing ions in a bolometric measurement. Still a few statements can be made with some generality: The area under a peak (in linear representation) corresponds to the total of ion number times ion energy. This can be due to few hot ions, which would rather broaden the structure; or a high number of relatively cold, still making up high signal strength in a narrow band. But we have also observed a series of ion peaks rising in height, but shifting to lower frequency, at constant width, upon repeated RF heating. Hence, some of this remains speculative until we have an independent measure of the ion number. However, in the regime of very high densities, when intra-cloud coupling is stronger than the trap properties, this does no longer hold.

The plasma frequency exceeds axial frequencies, so it is impossible to address ions specifically by RF excitation. In this case a high, broad peak with effective M and Q is formed, as seen in some of the production measurements (Figs. 5.6 and 5.7). The precise peak height depends on M and Q, as well as the cooling time constant, which is an important quantity in the studies of ramping rates, which is discussed below.

Cooling is essential not only because of Doppler broadening. A cold cloud is potentially smaller in size and thus has higher overlap with the laser beam. Also the shifts of motional frequencies is reduced, as explained in section 3.3 (unless different species influence each other), which minimizes uncertainty in the B-field determination. Furthermore, a cold, dense could is less susceptible to particle loss, caused by charge exchange with neutral residual-gas atoms, or by collisions with the walls. The latter is particularly relevant, since the trap cannot always be kept as deep as during production, but needs to be lowered for axial resonance and for transport.

Ar^{13+} ions should at least be confined until they are in resonance with the tuned circuit and can be resistively cooled. This condition relates various properties of the ion cloud and trap with each other, by the equation for axial resonance (Eqn. 5.1) and the relation between temperature and trap depth (Rel. 5.2). Storage can be enhanced by applying attenuation of the central CT electrodes with respect to the outer ones: Individual programming of channels includes the option to form a long deep potential well around a harmonic trap in the center. This has the purpose of not losing too many ions during a ramp, when they are still very hot shortly after creation. To this end, we have implemented an 'attenuated' mode of ramps, in which the outermost electrodes, E10/18, are always programmed with 250 V and the reference voltage starts with 5 V. If the ramp is intended to start with a ring voltage $|U_r|$ of less than 250 V, say 100 V, than this can be achieved by programming ±100 V to the individual electrodes E11 through E16 (C17 is wired to C11 = E11). For the potential in the center this is equivalent to $U_{\mathrm{prog}} = \pm 100\,\mathrm{V}$ and $U_{\mathrm{ref}} = 2\,\mathrm{V}$ (mind Eqn. 4.2). In the unattenuated case, this would be the faster way to realize the situation, and we assign a 'nominal reference voltage' U_{nom} of 2 V to this case—even though the physical reference (U_{phys}) is of course 5 V. For bookkeeping, we remember the 'attenuation',

$$\begin{aligned} T_A &\equiv U_{\mathrm{E11}}/U_{\mathrm{E10}} \\ &= U_{\mathrm{E11,start}}/250\,\mathrm{V} \\ &= U_{\mathrm{nom}}/U_{\mathrm{phys}}. \end{aligned} \tag{5.3}$$

This results in an effective $c_{0,\mathrm{att}} = c_{0,\mathrm{closed}}(1+1/T_A)$. The voltage at which ions get lost should be lower (in terms of absolute value) then the setting required for resonance. From this postulation and the parameters of the traps (Sec. 4.3) and resonators (Sec. 4.6) we derive a term for the maximum allowed temperature,

$$\begin{aligned} T &\leq \frac{(2\pi\,\nu_{LC}\,d)^2 M\,c_0}{6\,|c_2|\,k_B} \\ &= \frac{M}{k_B\,M_p} \times \begin{cases} 2.7\,\mathrm{eV}/T_A & \text{for CT} \\ 4.3\,\mathrm{eV} & \text{for ST,} \end{cases} \end{aligned}$$

with the mass given in atomic units and the temperature in terms of thermal energy. Ar^{13+}, for

instance, must be cooled from the above given energy of around 4 keV down to 0.1 keV (without attenuation), or at least to 0.5 keV in case of an attenuated ramp, starting with 1 V reference voltage, before it gets in contact with ARES CT. If this doesn't happen by other mechanisms, it will be satisfied by evaporative cooling, i.e. particle loss. Furthermore, if the initial ramp is too fast to cool ions significantly down while they are resonant, more will be lost at lower voltages. Anharmonicity of the potential in the CT helps in this case, because hot ions are shifted to lower frequency (i.e. higher voltage) and will remain resonant for an extended time, while ramping the voltage down (to lower absolute value).

While the discussion so far relates storage and resonance of a single species and depends on the mass only, equation 5.2 implies an option for purification from unwanted species with lower charge than Ar^{13+}—primarily the easily produced protons and bare light ions, which are otherwise hard to get rid of, due to their high charge-to-mass ratio and thus enhanced sensitivity to electromagnetic trapping fields. In thermal equilibrium, the less highly charged ions, even the lower charge states of argon, require a deeper potential well (in terms of voltage) than Ar^{13+} and are thus evaporated first. For optimization of the trapped-species spectrum, the electron energy for creation and the starting point of an unattenuated ramp should be carefully matched. However, for the purpose of keeping as many ions as possible of Ar^{13+}, we start the cooling procedure with a slow and attenuated ramp.

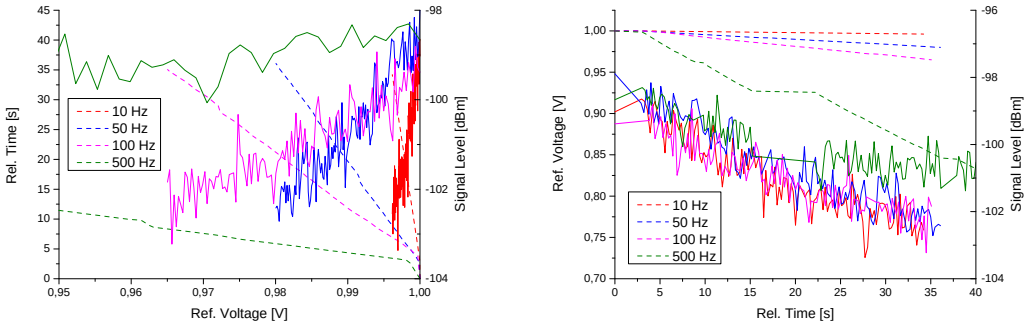

(a) Signal strength (and time, dashed lines) versus ramp voltage.

(b) Signal strength (and voltage, dashed lines) versus time.

Figure 5.8: Signal strength, ramp voltage, and timing of the initial broad-band cooling signature related to each other.

The following paragraphs present examples of the different cooling signatures: Figure 5.8 depicts measurements of initial broad-band cooling. Ions were sputtered from electrode surfaces with the electron source at −0.75 kV FEP and 1.0 kV accelerator voltage and subsequently bred for 3 min. After a concentration procedure, the CT was ramped from 1.0 to 0.3 V nominal external reference, hence with an attenuation of 0.2. The ramps differ by step size (equivalent cf. Sec. 5.2.3; values between 10 and 500 Hz are assigned to the plots in the legend) and thus ramp timing—which can be read from the dashed lines in figure 5.8(a). The ramping rate is roughly inversely proportional to the step size, since one iteration of applying a voltage and retrieving data takes a fixed time[1] of around 0.28 s.

[1]Some exceptions are seen as kinks in the time graphs and are explained by the control PC running at full

All of the ramps start with a high signal level of −99 dBm at 1 V, decreasing while the reference voltage is lowered. The faster the ramp, the larger voltage range is covered with strong signal, demonstrating that this mechanism is not governed by the trap voltage. In figure 5.8(b), the same data are drawn as a function of time, now with the ramp voltage additionally shown by the dashed lines. In this plot, the curves of signal strength look very similar, except for the 500 Hz measurement, which is saturated at −101 dBm. A common time constant (time for a drop by −4 dB) of roughly 30 s can be read from the plot, independent of the ramp timing. This long time cannot be explained by energy stored in the resonator, because with a resonator width of 0.3 kHz, the excitation lasts only for 3 ms. It must be far off-resonant cooling of an initially very hot ion cloud. The strong shifts due to high oscillation amplitudes that go along with temperature could be an explanation of this effect.

When this period of unspecific cooling is over, different species can be cooled if the set voltage matches the resonance condition for the (potentially shifted) ion oscillation frequency. We set up a series of measurements to probe the effects of ramping rate and evaporation to ion cooling or loss. To this end, ions were sputtered with the FEP at values between −1.7 and −0.3 kV and the accelerator at 1.0 kV for 3 min. After concentration, a sequence of CT ramps were conducted, all starting at 1.2 V reference voltage, but ending with increasingly flat trap settings. The initial ramp ends with 1.0 V, successive ramp ends are lowered by 0.1 V, down to a ramp ending with 0.1 V. This is made such that one ramp measures the trap content after cooling and the final voltage of the previous ramp have been applied. The entire program is conducted several times, with unattenuated ramps of 1000, 300, and 100 Hz step size, as well as attenuated ramps ($T_A = 0.24$) of 300, and 100 Hz step size. The step size $\mathrm{d}\nu$ plays a crucial role for cooling efficiency, because it defines the duration Δt of thermal contact between ions and resonator. With the period of each step $\mathrm{d}t \approx 0.28\,\mathrm{s}$, and an effective width $\Gamma_{\mathrm{eff}} \approx 10\,\mathrm{kHz}$ (width of the convoluted curves of ion cloud and resonator), the contact time is

$$\begin{aligned} \Delta t &= \frac{\mathrm{d}t}{\mathrm{d}\nu} \cdot \Gamma_{\mathrm{eff}} \\ &\overset{!}{>} \tau_{\mathrm{eff}}, \end{aligned} \tag{5.4}$$

which should be larger than the effective cooling time τ_{eff} of the ions, see section 3.4. With the applied step sizes, we obtain contact times of 3 up to 30 s, which is of the same order as the predicted initial value of the self collision time τ_T (Eqn. 3.22).

From the large amount of data, figures 5.9 and 5.10 show a few examples, all measured after production with −1.0 kV FEP voltage, which is among the most relevant settings. We observe a general tendency that in slower ramps the signal level is lower and width is smaller than in faster ramps, especially in repeated measurements with the same cloud. Shifts are however stronger in slower ramps. This confirms the principle that slow ramping rather cools a cloud and keeps many ions, forming a dense large cloud in the end, which is particularly observable in case of the 100 Hz version (Fig. 5.9(c)). With 1000 Hz step size (Fig. 5.9(a)), we observe signal only between 0.6 and 0.3 V ramp voltage, which corresponds to highly charged argon ions. After a ramp first enters this region (ending with 0.5 V), subsequent ramps measure less signal. Once 0.3 V have been reached,

capacity. The initial time step is however due to instrument communication, since at this point the CT is switched to non-unitary attenuation, therefore new values are requested at most channels of HV 250-8.

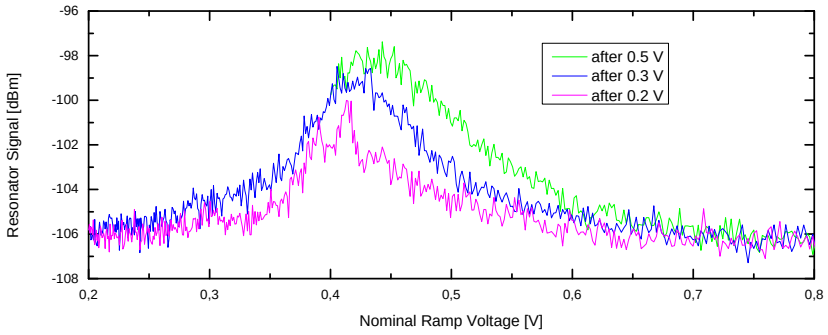

(a) 1000 Hz, zoomed.

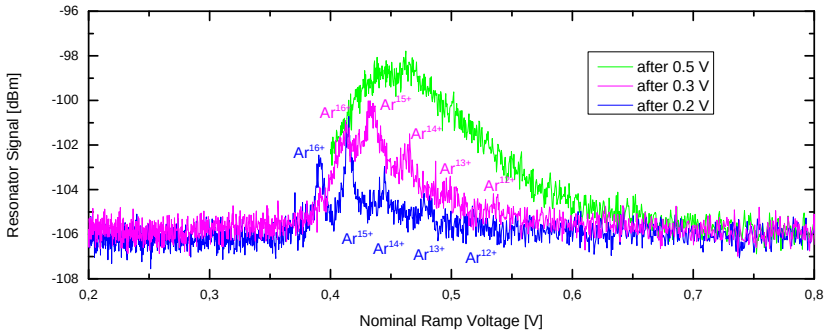

(b) 300 Hz, zoomed.

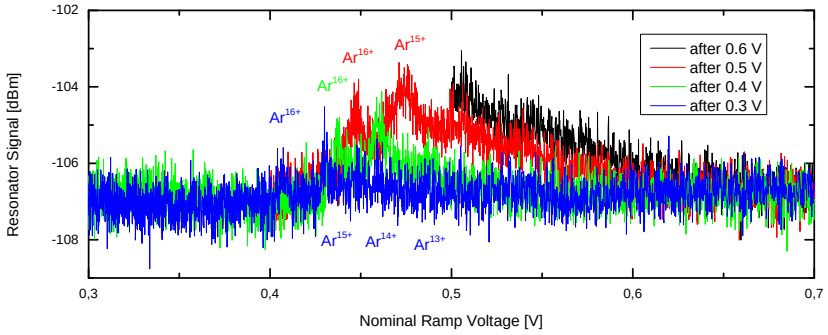

(c) 100 Hz, zoomed more closely.

Figure 5.9: Ion signal in repeated unattenuated ramps, lowering the trap voltage in every iteration, and with different ramping rates (step-size-equivalent frequency). Argon charge states up to 15 or 16+ can be identified.

the trace can be divided into discrete peaks. The ramps with 300 Hz step size (Fig. 5.9(b)) look similar, with a few differences: The width of all structures is narrower, such that in the end, we can quite clearly resolve charge states up to Ar^{16+}. The shift is reduced in between the last two ramps, but the spacing is unchanged, supporting the uniform-shift interpretation. The decreased absolute shift in the last ramp, together with low width and still considerable signal strength suggests a higher cooling efficiency than in the 1000 Hz ramp. This behavior also contrasts other cases, where the signal doesn't shift but only drops in repeated ramps. However, also particle loss must be considered at 0.2 V, which is a crucial threshold in most measurements of the series.

The ramps with 100 Hz step size are supposed to cool ions very efficiently (i.e. with little particle loss). This is reflected in the first depicted ramps ('after 0.6 V' and 'after 0.5 V') of figure 5.9(c): Signal is rising very slowly between 0.6 and around 0.5 V, until the slope intensifies towards a maximum, after which the signal suddenly drops. This is the aforementioned effect of an extended cooling, if the ions shift down in voltage, while the voltage decreases. From the observed shifts of around 20 % in terms of voltage (10 % frequency shift)—by which peaks move during cooling and where they appear in the final position—we can estimate cloud sizes of many millimeters radius, according to section 3.3. If a cloud retains this size still after cooling, then equation 3.21 implies an ion number up to a million.

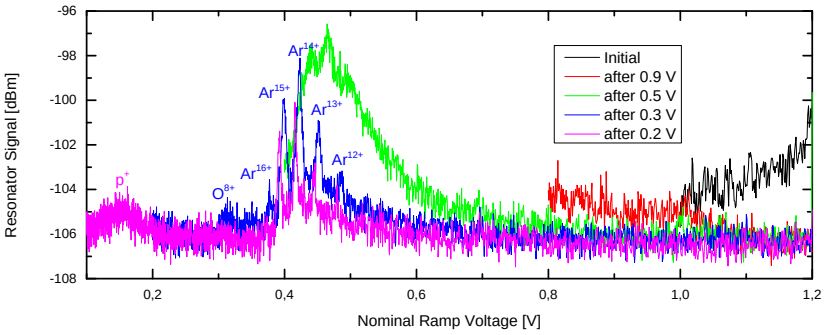

(a) 300 Hz.

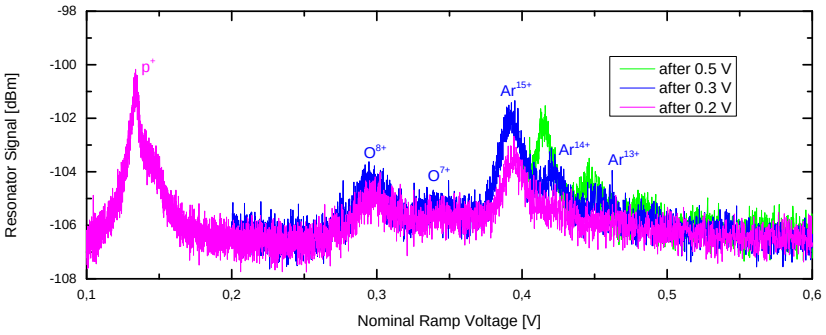

(b) 100 Hz, zoomed.

Figure 5.10: Ion signal in repeated attenuated (0.24) ramps, lowering the trap voltage in every iteration, and with different rates (step-size-equivalent frequency).

Comparison of attenuated and unattenuated ramps is a remarkable confirmation of the reasoning about confinement of ions with low absolute charge, equation 5.2: In both cases with 0.24 attenuation, presented in figure 5.10, ions with lower M/Q than Ar^{16+} can be detected at ramp voltages below roughly 0.38 V. The most reasonable candidates around 0.30 and 0.35 V are bare and hydrogenlike ions of carbon, nitrogen, and oxygen, and H_2^+, all with $Q \leq 8e$. The peak at 0.14 V must be from protons (predicted voltage 0.131 V), of which we have never observed signal above −104 dBm without slow attenuated ramps. In the slower ramps (100 Hz step size, Fig. 5.10(b)) the signal of these light ions is very strong, while in the faster ramps (300 Hz step size, Fig. 5.10(a)) argon ions dominate. In the more highly resolved ramps, we can even observe a shoulder to the proton peak, indicating that some protons have escaped into the neighboring traps E12 and E16. Ions in E12 are equally close to the pickup electrode (E13), but the trap has slightly different properties, due to the −4.2-fold bias of E10 (attenuation), rendering ions at different frequency than in E14. Escape to E12 is another clear sign that protons would have been lost without the potential well of E10 and E18 (i.e. non-unitary attenuation).

Other than that, the peaks around 0.4 V in the slow ramps do not shift, but only lose intensity after ramp voltages first reach the signal—which according to the introductory words of this section would indicate ion loss—even though the bare-ion peak at 0.3 V remains constant. We assign the peaks to Ar^{15+} and lower charge states, but also note that the signal is already rather weak when the resonator first detects ions (in the slow ramps). On top of this, the strong initial signature with around 30 s time constant is only observed in the fast ramps (Fig. 5.10(a)), along with slopes as in the red curve ('after 0.9 V'), that successively climb and meanwhile consume the broad signal. This broad peak is first fully seen in the green curve, between 0.6 and 0.4 V. The signature of a slope being lowered from one iteration to the other is again interpreted as extended cooling of very hot ions while they are shifting down. After the fast ramps have reached 0.3 V, the broad signal decomposes into sharp, strong peaks of Ar^{16+} to Ar^{12+} with original spacing, but shifting down and narrowing in each iteration. These signals do not not lose much peak height, but more intensity is left over in last ramp, compared to the slow ramp, which indicates efficient cooling.

The discrepancy in initial signal between slow and fast attenuated ramps may either be caused by different production conditions, such that before the slow ramps start less argon ions were created—even though the settings were the same. An alternative explanation would be evaporative cooling by protons, taking away more heat and appearing more strongly in the slow ramps.

When we observed the strongly varying shifts in motion frequencies (resonant voltages), we started adaptive (peak-following) cooling: In regular time intervals a rather fast ramp is measured and after that the trap is supplied with the voltage that maximized the signal. Strong signal is caused by much dissipation, so this is the setting for optimal cooling, at least until the ions have shifted away by cooling. But then the voltage is adapted again. The effect is shown with two different visualizations in figure 5.11. After sputtering and breeding ions with −1.1 kV FEP and 1.0 kV for 3 min, we requested repeated attenuated ramps with 300 Hz step size. A few iterations were done with the interval from 1 to 0.3 V ramp voltage and a repetition time of 30 min. Then we changed the lower bound to 0.1 V. Immediately the (double) proton signal dominates, as in figure 5.10(b). But after around 9 h of being resonant with the detector it is cooled below the hump at 0.37 V, which contains several ion species as can be seen after many hours of cooling.

This happens between traces 1 and 2 of figure 5.11(a), depicting zoomed images of 4 successive ramps. Then the algorithm selects 0.36 V for further cooling and within one iteration the situation

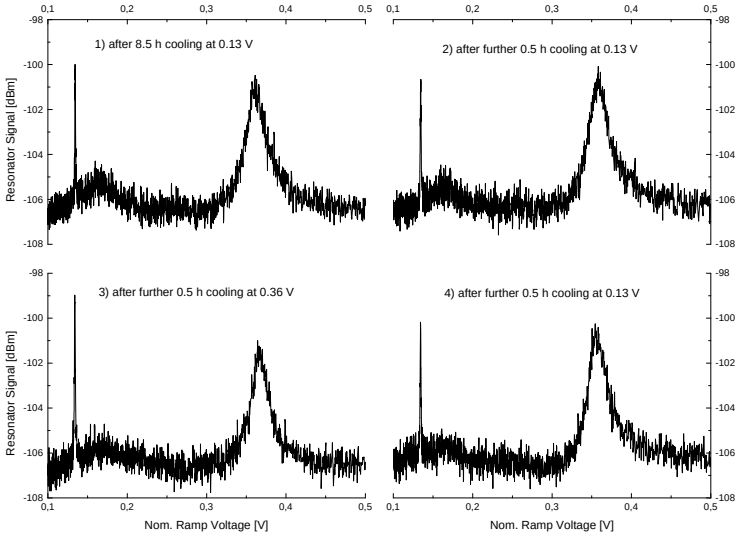

(a) Selective cooling.

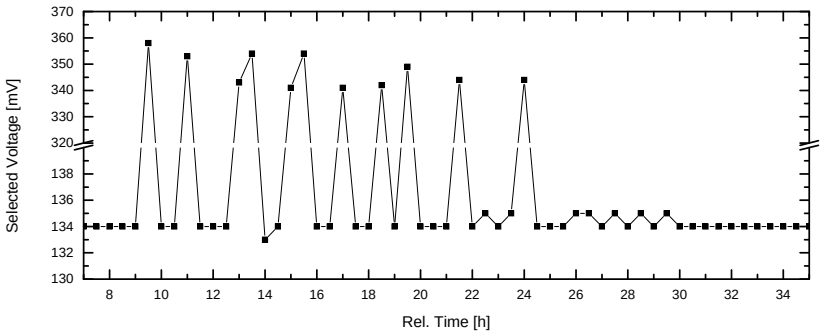

(b) Hopping between peaks.

Figure 5.11: Peak-following cooling of competing ion species over 42 h.

flips back. But the following 30 minutes bring the proton signal back down, almost to the level of the other structure. We have recorded the voltages chosen for cooling and they are plotted in figure 5.11(b). This shows that hopping is continued for several hours, before the ion structure differentiates into two lower humps. These can no longer compete with the protons, although even the protons lose a lot of signal. The two new humps can be identified with bare atmospheric ions (around $M/Q = 2$), which soon die away, and a bunch of argon ions, which eventually develops into a clear comb with charges between 14+ and 8+. This happens only after 44 h, when we had done various other procedures with the cloud.

We recall from section 3.4 the chain of heat reservoirs formed by radial and axial, internal and external degrees of freedom, and the resonator, coupled by time constants with strongly varying

values. The measured 30 s decay time of initial noise is in agreement with the observation that the contact time of 30 s (at 100 Hz step size) has a strongly enhanced effect compared to faster ramps. It can be identified with the self-collision time τ_T, which in the beginning is rather long, but with falling temperature and increasing density speeds up. The ongoing effect after hours of cooling cannot be explained in this model. The observation that peaks in figure 5.11(a) rather grow and return to their earlier shifted position in the voltage spectrum (cf. Fig. 5.11(b)) if they have not been cooled indicates that we have to consider heating mechanisms.

We conclude that in this case resonant cooling of selected (groups of) ions was dominant over thermalization by sympathetic cooling. This is a crucial prerequisite for cleaning, where Ar^{13+} should be kept and all others be heated out of the trap. Concerning this matter, we could so far only demonstrate heating of the cloud as a whole by RF excitation on different CT electrodes. In general, the measurements of this chapters pave the way for optimized production of Ar^{13+} by breeding close to the threshold and evaporating lowly charged ions in a slow unattenuated ramp. This might be sufficient for the time being.

5.6 Transport to the Spectroscopy Trap

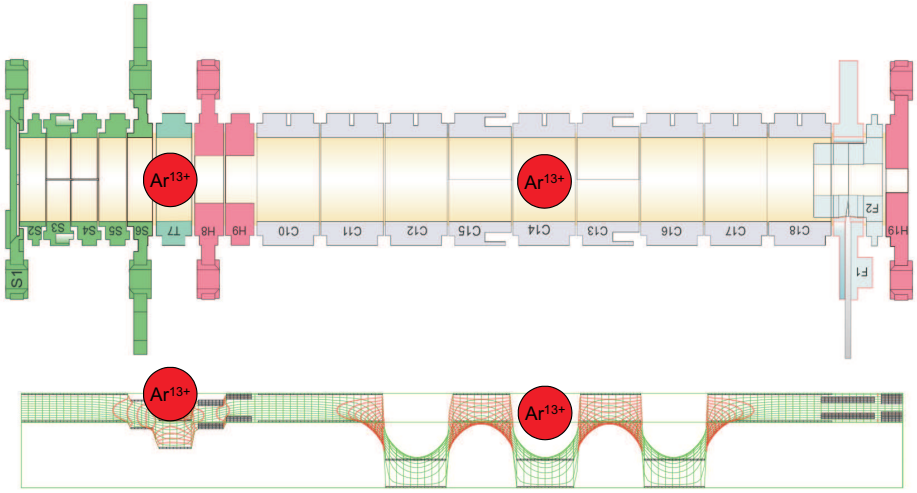

Figure 5.12: The procedure of ion transport, indicated by an example set of electrode biases. The resulting electrostatic potential has been simulated with SIMION.

After a pure cold cloud of Ar^{13+} has been prepared in the CT, it is transported to the ST. This is done with a moving potential well, as depicted in figure 5.12. This image shows the option of keeping a fraction of the cloud in the CT, serving as reservoir. This will be relevant for isolating single ions and performing a B-field calibration via motional frequencies—as discussed in the sections of chapter 3, the axial-frequency shift and width with a large cloud are too high to for the desired resolution. The reservoir would save the time of preparing a new cloud over and over for repeated measurements. A routine for separating a low number of ions from a cloud is yet to be implemented.

Depending on the proportions of transport electrodes, a number of N rings is supplied with negative voltage, while the rest is grounded. In the CT and HV electrodes, N is 1, while the ST have a rather low length-to-diameter ratio and thus the transport well is formed with 2 electrodes. Every step consists of lowering a new electrode ahead in the direction of transport and then grounding the electrode behind, such that the well is extended (and not shortened) intermediately. We currently use $-60\,\mathrm{V}$ as transport potential, which needs to be modified for a precision measurement with the UM and BS supplies.

The concept discussed so far is currently not feasible due to an unwanted contact between two electrodes needed for transport (E11 and E13). Therefore the transport well is exceptionally extended from E13 to E10 and with a depth as low as $-250\,\mathrm{V}$, while E14 is set to $250\,\mathrm{V}$. Thus, the ions is pushed as far as possible into E11—but with a low electric field and hence low magnetron frequency, therefore ions are easily affected (unwantedly) by RF signals, passing the RC filters (edge frequency around $1\,\mathrm{kHz}$). For further transport, E12 is raised to $250\,\mathrm{V}$. Then the procedure is continued in the usual way. Success of this modified step has been confirmed by transporting ions to E10 and back to E14 in the same way.

Transport of cooled ions to the ST could however not be demonstrated yet. But this is probably caused by the low quality factor of ARES ST, which is not suitable to detect cold ions. For this reason we omitted the cooling procedure and transported hot ions. We have also implemented a 'stacking transport' procedure, which keeps ions at $-60\,\mathrm{V}$ in E3 (ring electrode of ST, while adjacent compensators are at $-50\,\mathrm{V}$), while new ions are being created in the CT. These new ions are transported in a well of $-45\,\mathrm{V}$ and added to the old ones. The simple transporting procedure dump old ions into the endcap E1. In measuring the content of the ST by voltage ramps, we observed that signal is increased up to a saturation after three iterations, as seen in figure 5.13. It demonstrates a large enhancement after the first step of stacking and another weak improvement up to the third iteration. Five more stackings do not further change the signal.

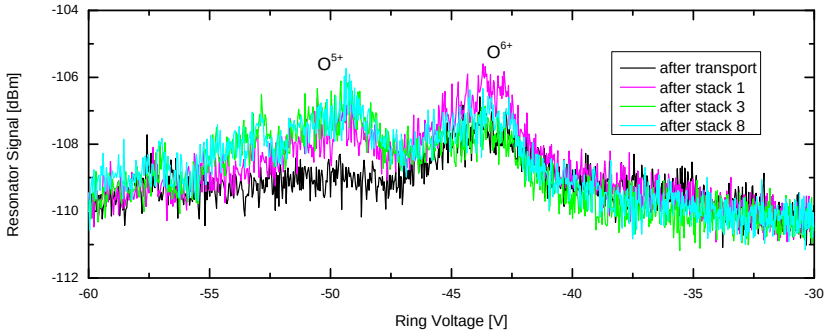

Figure 5.13: Ion signal in the ST after transport, 1, 3, and 8 stackings.

These measurements have been conducted with ions produced by charge breeding for 2 min at $-0.9\,\mathrm{kV}$ FEP voltage and $1.0\,\mathrm{kV}$ at the accelerator from gas pulses with 0.6 mbar pressure and 54 ms duration after applying $13\,\mathrm{V}$ to heater 1 for 3 s. The observed peaks are best explained by oxygen ions with untouched $1s$ shell. In a reference measurement without repeated creation we have excluded that the signal enhancement through stacking is caused by the mere transport

procedure: It can only be reproduced with creation prior to transport.

5.7 Storage Time

With almost the same creation settings (but 0.7 instead of 0.6 mbar gas pressure), we have measured the time ions remain stored, before they are charged down by reactions with neutral atoms. Figure 5.14(a) shows traces recorded directly, 1, and 8 h after the last stacking iteration. In this case, we stacked twice on top of a non-stacking transport. For matters of reproducibility, we created ions every time anew—otherwise the signal could have been modified or even lost by cooling. The ramps find the same species of oxygen again. After a eight hours the amount of O^{6+} is re-

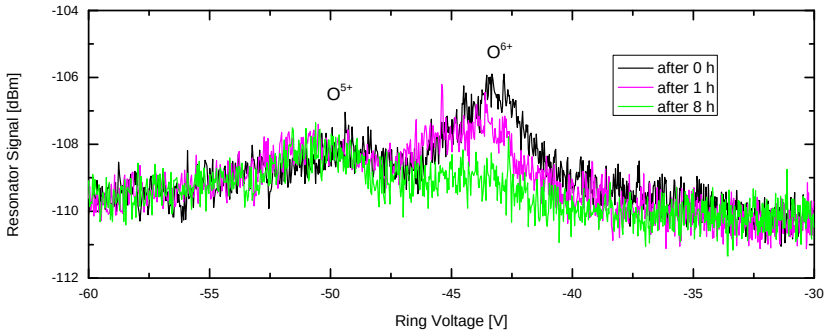

(a) In the spectroscopy trap.

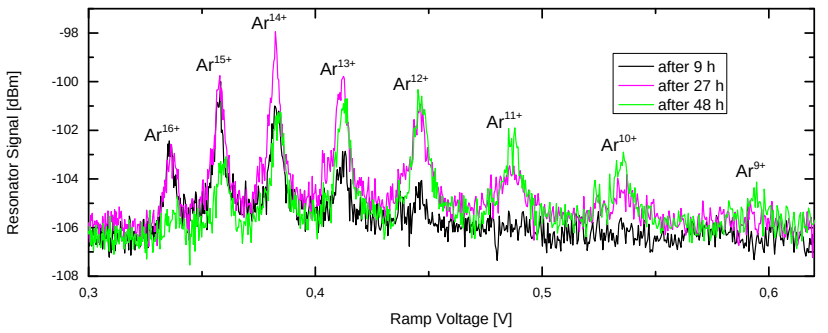

(b) In the creation trap.

Figure 5.14: Ion signal after different storage times.

duced, almost to the detection threshold, while the peak height for O^{5+} remains roughly constant. O^{4+} is expected at −64.5 V, which is not within range of the trap electronics. We deduce that the lifetime of O^{6+} versus charge exchange is a little below 8 h.

A similar measurement has been performed in the CT after production with 3 min of charge breeding at −1.5 kV FEP and 1.0 kV accelerator voltage upon a gas pulse with around 1.4 mbar pressure and 54 ms duration through the valve, heated with 13 V at heater 1 for 6 s. After a single concentration, we started a series of ramps from 1 to 0.26 V, with a step size of 300 Hz. Five ramps were requested immediately in a row, the next five ramps followed after an hour—later

we extended the repetition interval to 3 hours. In this case, reproducibility is obtained by a thermal equilibrium after so many cooling ramps. Figure 5.14(b) shows a selection of three ramps, recorded 9, 27, and 48 h after production. In all cases we chose the earliest of the five repeated ramps, but the other ones are similar. In these measurements the ions appear with relatively low shift of 10 mV and width, but considerable signal strength. Temperature fluctuations have the Ar^{16+} signal appear almost identical in the two first curves—but normalized to the intensity in the Ar^{14+} peak, the earlier ramp has much more signal of the highest charge state than the later ramps. After 48 h there is hardly any signal from Ar^{16+} left, while some has built up at Ar^{9+}.

From the plots we estimate a lifetime of around 20 h for Ar^{16+}. Considering a cross-section for charge exchange with helium gas of $3 \cdot 10^{-15}\,\mathrm{cm}^2$, which is more or less valid for all present argon species [Man86], we can calculate a residual gas pressure of around $4 \cdot 10^{-13}\,\mathrm{mbar}$. Reactions with hydrogen molecules obey cross-sections about 2 to 3 times as high and would restrict the pressure estimation by that factor if hydrogen was assumed to be relevant. Cross sections for charge exchange of O^{6+} have very similar values—although there are velocity-dependent tendencies, but with opposite sign, for collisions with H (2.5 to $4.2 \cdot 10^{-15}\,\mathrm{cm}^2$) and H_2 (5.5 to $3.7 \cdot 10^{-15}\,\mathrm{cm}^2$) in the range of 1.3 to $14 \cdot 10^7\,\mathrm{cm/s}$ [PAMC82]. Even the lower end of this scale is not likely to be reached in our trap, therefore we cannot directly apply these values. Also the intuitive argument of comparing ionization potentials is not always valid. So the shorter lifetime does not necessarily imply a higher pressure.

In general, the long storage time for highly charged argon is a valuable finding in two senses: It is sufficient for performing precise measurements after some steps of preparing an ion cloud; and it implies the most significant benchmark test for our cryogenic gas valve, after the measurements in section 4.5 could only state a pressure below $5 \cdot 10^{-9}\,\mathrm{mbar}$.

5.8 Laser Spectroscopy

We have attempted laser spectroscopy both with hot ions after detecting them with ARES ST and with ions that had been cooled in the CT and hence were not visible with electronic detection in the ST. We scanned the spectroscopy laser in the free-running mode (cf. Sec. 4.9) in order to excite fluorescence in Ar^{13+} ions and gated the CPM detector (cf. Sec. 4.10) for delayed observation. Figure 5.15 depicts the principle of irradiation and light collection through the meshed endcap S1.

An example signal is shown in figure 5.16, recorded with the spectroscopy laser scanning over the expected resonance frequency ν_6 (from Eqn. 3.1) with a depth of around 1.7 GHz and a rate of 200 Hz and with relatively high power of $323\,\mu\mathrm{W}$ at the fiber incoupler. Ions had been produced with −0.95 kV FEP and 1.1 kV accelerator voltage, breeding for 2 min on a 0.7 mbar gas pulse. After roughly 2 h of cooling (slow initial plus peak-following, both repeated after concentration), transport to the ST was requested. Then the spectroscopy measurement was started, performing almost $3 \cdot 10^5$ cycles of 100 ms irradiation, followed by 100 ms observation. For evaluation the arrival times are separated to bins with 0.1 ms width and normalized and a sum of four exponential decays (free amplitude and time constant) plus offset is fitted to the data in the interval from 2 to 110 ms after trigger (beginning of observation). The result is time constants of 0.17(2) ms, 0.70(5) ms, 7.5(6) ms, and 14.7(1.0) ms and a background of 0.84(3) Ct/s. The fit seems to explain the data

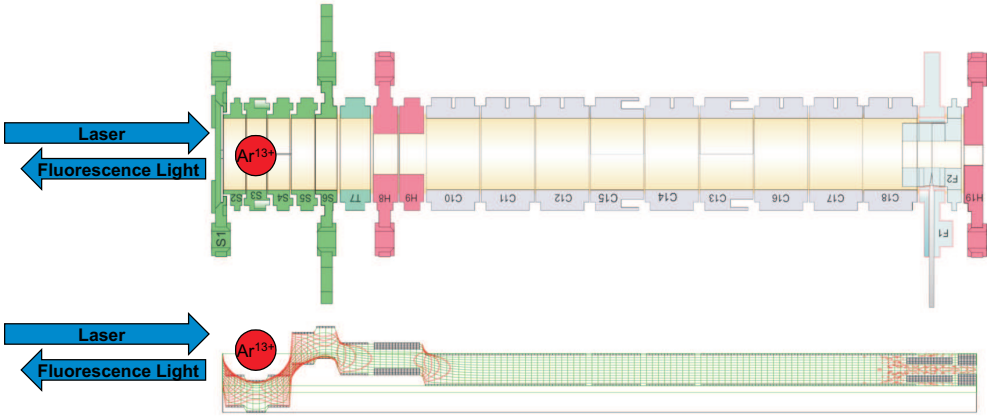

Figure 5.15: Laser spectroscopy with ions in the ST. The applied electrostatic potential has been simulated with SIMION.

well.

In reference measurements, either detuned by 23 GHz in any direction or with a deliberately empty trap we repeatedly found a time constant even closer to the expected 9.6 ms of Ar^{13+}, namely 10.4(2) ms. But precise values of these time constants often change with the choice of the fit interval. In a few cases of on-resonant excitation there was even a weak component with 9.6(4) ms, which could however not be resolved from the other signal nor reliably reproduced. We will have to wait for the filter mentioned in section 4.10 with a narrower acceptance band or find out what causes the fluorescent background and how it can be completely avoided.

Based on the references listed in chapter 2, we can however exclude that the resonance was missed, because both g factor and B field are known within 10^{-4} or better and the laser scan is rather 10^{-2} wide. Also the uncertainty from the fine-structure interval should be covered by this. The scan could rather be chosen a little narrower and would thus increase excitation efficiency.

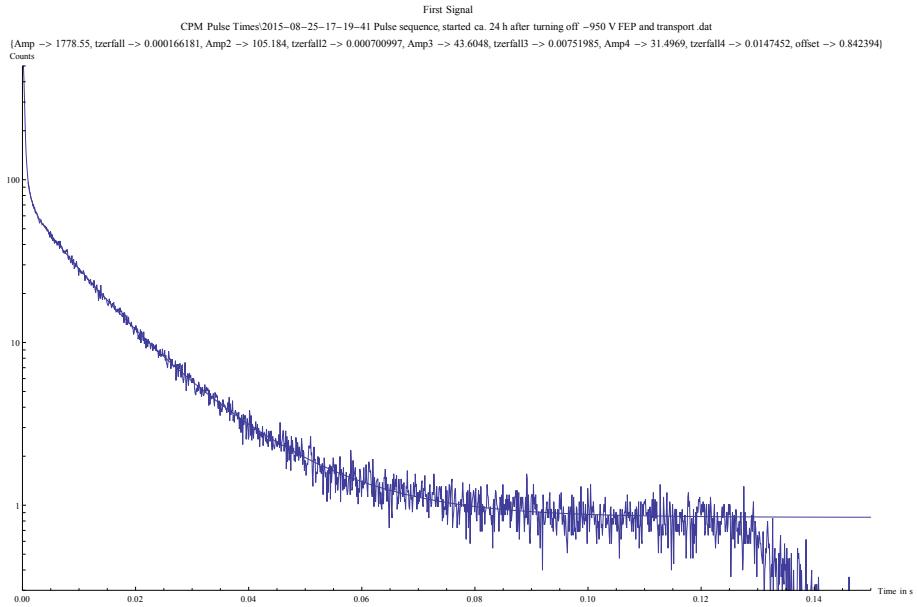

Figure 5.16: Time-resolved fluorescence measurement with constant and decaying background.

Chapter 6

Summary and Outlook

– What has been achieved and what needs to be done –

This thesis presents the ARTEMIS experiment in the stage of laser-spectroscopic g-factor measurements. After motivating investigations with highly charged ions, I have given an overview of relevant literature about the fine-structure transition in Ar^{13+}, namely the Zeeman effect, which arises from the external magnetic field of the Penning trap setup and is characterized by linear g factors 0.663 647 7(7) and 1.332 282(3) [SGV$^+$15] and higher orders [LWG$^+$13] and [Gla15] (cf. Tab. 2.1), furthermore the air wavelength 441.255 68(26) nm [MKB$^+$11], and the lifetime 9.573(4)(5) ms [LJC$^+$05]. Attention is drawn to the quadratic Zeeman effect due to the high magnetic field strength, which we anticipate having experimental access to. This is again the focus of chapter 3 about experimental feasibility with the currently available methods of laser spectroscopy and bolometric ion-cloud detection. The study of disentangling the contributions of fine-structure splitting, linear, and quadratic Zeeman effect from optical resonance frequencies is meant to supplement a corresponding examination about the microwave (Zeeman) transition frequencies, presented in [LWG$^+$13].

The following chapter 4 is an inventory of the experimental equipment required for this kind of measurement, which we have been setting up in the past years. Special emphasis is laid on the design of a dedicated half-open Penning trap, which combines efficient light collection and a highly harmonic storage potential for precision laser spectroscopy. Further aspects are home-made cryogenic sources for high-energy electrons and for argon gas, which are the central elements of a miniature EBIT for in-trap ion creation. I have included settings we have found for efficient operation, by which the electron source delivers up to 500 nA of current into a reflectron at an energy which can be chosen in a range from around 0.3 to 2 keV. For the gas valve we have found the influence of temperature and input pressure, while the performance of pulses of around 50 ms duration has only been assessed in chapter 5 about measurements with the complete apparatus. Chapter 4 concludes with a presentation of the laser system, assembled within our collaboration with TU DA, and of the detection optics, used both for laser spectroscopy as well as for the double-resonance method.

In chapter 5 I have reported the key achievements in ion preparation up to the present day. We have four working points for production of large clouds (estimated many thousands up to a million) with argon ions up to heliumlike argon (Ar^{16+}), in agreement with predictions based

on the ionization potentials. Parameters can be tuned to optimize the fraction of the desired boronlike charge state. Different mechanisms of cooling have been realized and we have observed a positive effect, extending storage time up to many hours. A proof of principle is supplied for transporting ions to the spectroscopy trap within a few seconds, and we could increase the amount of ions there by a stacking procedure. First fluorescence signal from the spectroscopy trap has been observed. These results are the reward for overcoming the tremendous challenges which result from the high degree of complexity in this experiment. It features almost a hundred electric supplies entering the outer vacuum chamber, spanning from a few kV, restricted to a μA current, to low-voltage channels with required stability in the μV range; in terms of frequency covering the low-fluctuation DC range as well as excitations at kHz, MHz, GHz, and up to PHz frequencies with resolutions ($\nu/\delta\nu$) of 10^9 or above; in a cryogenic, highly magnetic, and evacuated setting; with each ion manipulation procedure coordinating multiple external devices.

The immediate next steps should be transport of a cold cloud into—or cooling inside—the spectroscopy trap, systematic application of laser spectroscopy, and refinement of the fluorescence signal from the strong background. With a repaired resonator and resolved short circuit in the electrode wiring, transport will be much easier to achieve and detect. The inclusion of microwave excitation and the transfer of the bolometric detection technique to single ions will be milestones for the further future. These methods shall allow a determination of g factors with ppb accuracy, as well as of the quadratic Zeeman effect on the level of around 10^{-5}. In both cases this is four to five orders of magnitude more precise than the expectations of a pure laser-spectroscopic measurement and enables us to test theoretically predicted contributions of relativistic electron correlation and quantum electrodynamics.

When these steps have been established, the experiment will be connected to the HITRAP facility for injection of hydrogenlike ions like bismuth ($^{209}Bi^{82+}$) ions. The application of laser-microwave double-resonance spectroscopy to the hyperfine-structure transition of this atomic system promises a stringent test of QED in the strong-field regime as well as a measurement of the nuclear magnetic moment without the need to correct for diamagnetic shielding.

Appendix A

External Field of the Magnet

Here (Fig. A.1) is a drawing of the magnetic field outside our cryostat, mentioned in section 4.1. Most devices withstand 50 G, so the upper side is uncritical. Close by the lower flange there are however tremendous field strengths and—what is also very important—gradients.

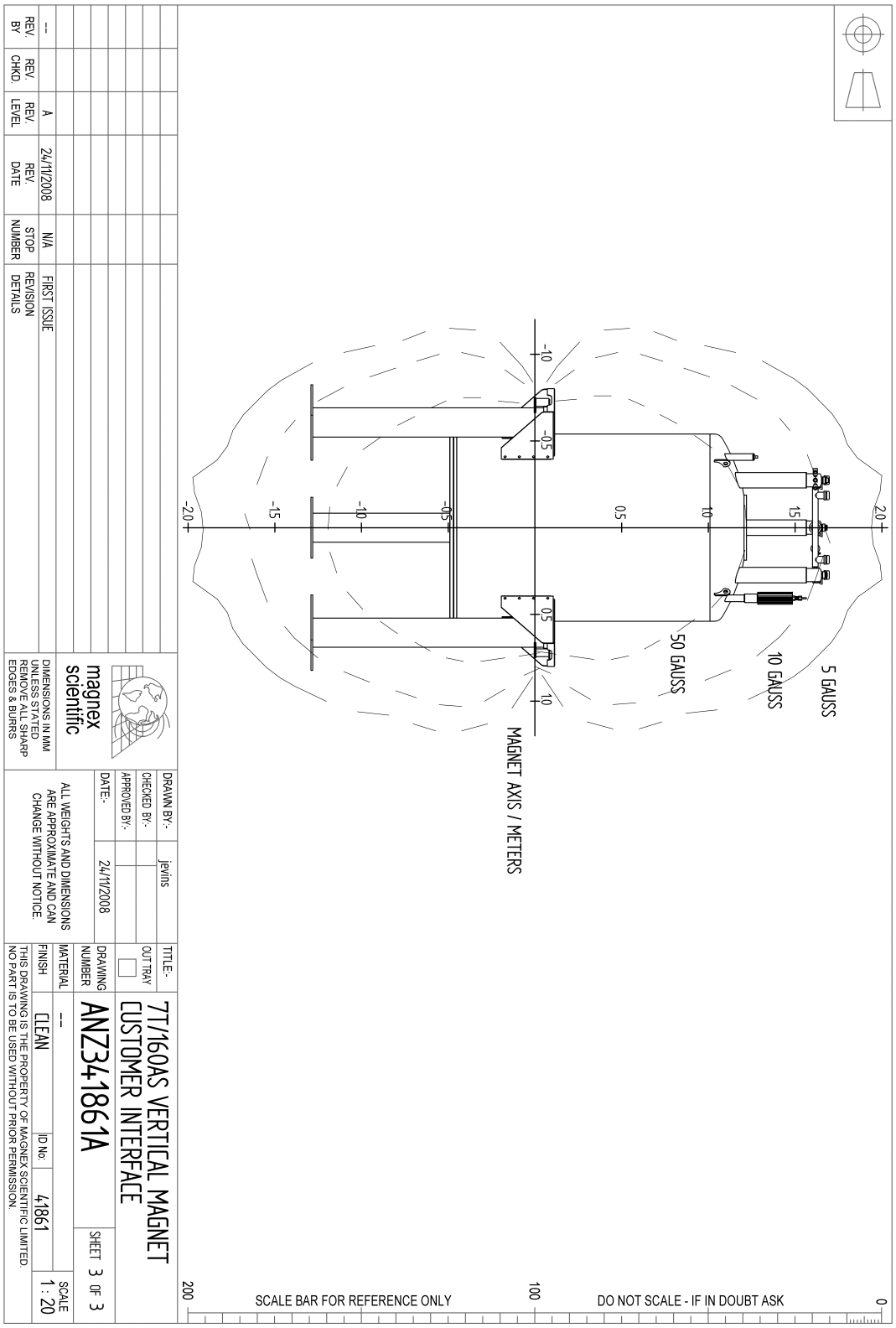

Figure A.1: External Field of the Magnet [Mag08].

Appendix B

Proposals for Double-Resonance Spectroscopy

B.1 Procedures

Here is a list of measurement concepts of laser-microwave double-resonance spectroscopy, focusing on the disentanglement of different contributions to the Zeeman effect, including higher orders. It is a supplement to the proposals given in [LWG+13] and an extension to the calculations done in the appendix of [Lin10].

We start with Fermi's golden rule for transition rates:

$$R = \frac{2\pi}{\hbar^2} \left|\langle i| H_{\text{int}} |f\rangle\right|^2 \delta(\omega_0 - \omega), \tag{B.1}$$

where ω_0 is the transition frequency and ω the frequency of the external field. The Hamiltonian operator of the magnetic dipole interaction is:

$$H_{\text{int}} = g_J \mu_B \frac{\vec{J}}{\hbar} \cdot \vec{B} \approx \frac{\mu_B}{\hbar} \left[\vec{L} + 2\vec{S}\right] \cdot \vec{B}, \tag{B.2}$$

where the convenient approximation $g_S = 2$ has been used. While the static magnetic field $\vec{B}_0 = (0, 0, B_0)$ defines the coordinate system, the interaction of the decaying electron is with the field $\vec{B}_\omega$ of the emitted photon[1].

We give the transition matrix elements $\langle i| \left[\vec{L} + 2\vec{S}\right] |f\rangle$, which contain the main information about the relative rates and also about the emission characteristic. These are

$$\left\langle \frac{3}{2}, +\frac{3}{2} \right| \left[\vec{L} + 2\vec{S}\right] \left| \frac{1}{2}, +\frac{1}{2} \right\rangle = \sqrt{\frac{1}{6}} \hbar \left[\vec{e}_x - i\vec{e}_y\right]$$

[1] Intermediate steps of the calculation are given in Sec. B.4

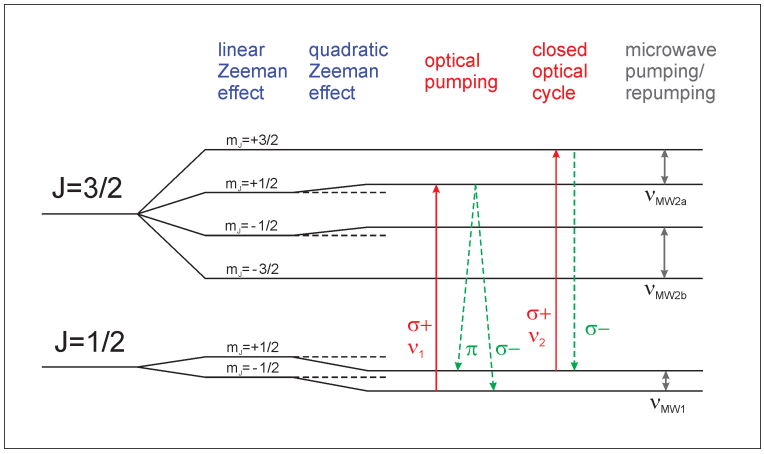

Figure B.1: Spectroscopy of the $2\,^2P_{1/2}$—$2\,^2P_{3/2}$ fine-structure transition, as in a boronlike argon ion, with Zeeman effect. The level scheme (not true to scale), some magnetic dipole transitions are shown. Solid arrows indicate excitation by laser photons, while dotted arrows are spontaneous decays. Gray double arrows represent microwave transitions.

for the decay emitting frequency ν_6, which changes M_J (Eqn. B.4, σ-polarization, different notation from [MKB+11]), and

$$\left\langle \frac{3}{2}, +\frac{1}{2} \middle| \left[\vec{L} + 2\vec{S}\right] \middle| \frac{1}{2}, +\frac{1}{2} \right\rangle = -\sqrt{\frac{2}{9}}\hbar\vec{e}_z$$

for the π wave at frequency ν_4 (Eqn. B.5). The σ-transition of the $|3/2,\, 1/2\rangle$ state comes with the frequency ν_5 and the dipole moment (Eqn. B.6):

$$\left\langle \frac{3}{2}, +\frac{1}{2} \middle| \left[\vec{L} + 2\vec{S}\right] \middle| \frac{1}{2}, -\frac{1}{2} \right\rangle = \sqrt{\frac{1}{18}}\hbar\left[\vec{e}_x - i\vec{e}_y\right].$$

For the derivation of the partial decay rates we assume an equal distribution of $\vec{B}_\omega$ components in the vacuum fluctuations causing the spontaneous decay (again, cf. Sec. B.4). The partial rate for a σ-decay is then $R_{3/2\to 1/2} = c\cdot 1/3$ and $R_{1/2\to -1/2} = c\cdot 1/9$ from the respective initial state. There is only one type of a π decay, namely $R_{1/2\to 1/2} = c\cdot 2/9$, where c defines the absolute scale of the transition rate. Independent of this value, we see two important points:

- All Zeeman sub-levels have the same lifetime, namely $3/c$.
- The $|3/2,\, +1/2\rangle$ decays preferably to the $|1/2,\, +1/2\rangle$, namely twice as often as to $|1/2,\, -1/2\rangle$ ('branching 2:1')

Let us apply this to the options of experimental procedures, based on the level scheme (Fig. B.1):

Visible Probe, MW1 Pump A variation of the scheme mentioned in [LWG+13] relies on saturated population distributions. Initially, the lower state sub-levels should each be represented at 50 %. If we saturate the optical probe transition, the distribution among $|3/2,\, +3/2\rangle$, $|1/2,\, +1/2\rangle$,

and $|1/2, -1/2\rangle$ should be $\frac{1}{4} : \frac{1}{4} : \frac{1}{2}$. We can then also saturate the lower state microwave transition and end up with $\frac{1}{3} : \frac{1}{3} : \frac{1}{3}$. For the initial broadband search of the microwave frequency we could even apply a Landau-Zener sweep. If the Larmor frequency is within the sweep interval, the final distribution will be $\frac{3}{8} : \frac{3}{8} : \frac{1}{4}$. This goes along with an enhancement of the fluorescence intensity by a factor of $\frac{4}{3}$ or even $\frac{3}{2}$.

This method requires high intensities of the EM fields and sufficient temporal control of them. It is again restricted to the lower level g-factor. And it encompasses quite a sensitive intensity measurement. We will see, if the signal to noise ratio allows for that. But it can easily be extended to following concept, to which it would serve as first step.

Visible Probe, MW2 Pump, MW1 Repump Instead of the lower state Larmor frequency, we apply the upper state one together with the probe laser. This eventually pumps all ions to the dark $|1/2, -1/2\rangle$ sub-level. It is the same idea as in b), but without initial pumping to $|1/2, +1/2\rangle$. Therefore the fluorescence signal is at first weaker than in the other case. However, now the 65 GHz microwave can efficiently sweep all ions into the upper sub-level, and the cycle can start over with a stronger signal. Subsequent irradiation of the two microwaves will turn the fluorescence on and off. It would be good to check, if 2 MW frequencies can be irradiated simultaneously.

This gives again access to the quadratic effect. However, the unfavorable line shape arguments are the same as in b). And again, the upper level microwave transition must be driven in the right moment. Again we face the problem that fluorescence may be off for two reasons: All ions are dark or the laser frequency is detuned.

For any method that determines one of the Larmor frequencies in the excited level (MW2a or MW2b), we can obtain the partner and thus disentangle the linear and the quadratic effect: The whole procedure must be repeated with opposite signs - meaning that the laser must then probe the $|3/2, -3/2\rangle$ — $|1/2, -1/2\rangle$ transition, 325 GHz apart from the other frequency. Or in the case of the pump frequency, the shift to the $|3/2, -1/2\rangle$ — $|1/2, -1/2\rangle$ system is 195 GHz.

This method is interesting because there is a visible signature for laser resonance, in contrast to other methods. If the normal situation is that there is no fluorescence, then you don't know why you see nothing. Is it because the laser is off-resonant or because the microwave is on-resonant?

Visible Pump, Probe We start with the pump laser, as well. Then, the $|1/2, +1/2\rangle$ population is probed by a laser beam at a slightly higher frequency. This drives the closed transition to the $|3/2, +3/2\rangle$ sub-level. When we bring in a microwave field at either Larmor frequency, the cycle will be disturbed. The fluorescence signal reduced by ab amount that depends on the respective intensities and temporal overlap of the exciting waves. The upper state resonance will only take effect, if the two EM fields are applied sufficiently shortly after each other. Of course the ions must be able to absorb the microwave. This method is interesting because there is a visible signature for laser resonance. However, it requires repumping and therefore it is hard to determine a proper line shape. Once the microwave gets close to the resonance, it is just a matter of time that the new equilibrium population distribution is established. A continuous repump beam could help with this. However, then still the 2 / 3 D map of fluorescence intensity would have a saddle point at the double-resonance condition, which is not so convenient to detect.

Furthermore, this originally favored method it is currently infeasible, because the pump and

probe frequencies are detuned by 65 GHz. There are no modulators producing such far sidebands. We would then need a second light source. A weaker B field or smaller g-factor would bring this method back into play. The question arises if the Larmor transition would be saturated or fully population-exchanged. With the very long lifetime, I would say we are always in the regime of Rabi-oscillations.

B.2 Emission Characteristic

The probability to find an emitted photon with a particular magnetic field (amplitude) $\vec{B}_\omega$ can be derived from Fermi's golden rule, if this field vector is inserted in equation B.1. It follows that the probability distribution is proportional to the square of the scalar product of $\vec{B}_\omega$ and the term B.4 for the decay with σ polarization, which we are going to detect. Then the intensity is $I(\theta') \propto \left|[\vec{e}_x - i\vec{e}_y] \cdot \vec{B}_\omega\right|^2 \propto \sin^2\theta'$, where θ' is the angle between $\vec{B}_\omega$ and $\vec{e}_z$.

For an electromagnetic wave, the wave vector $\vec{k}$, indicating the direction of propagation, is perpendicular to the local magnetic field. We decompose

$$\vec{k} = k\,[\sin\theta\cos\phi\ \vec{e}_x + \sin\theta\sin\phi\ \vec{e}_y + \cos\theta\ \vec{e}_z]$$

and assume an equal distribution of $\vec{B}_\omega$ in the plane perpendicular to $\vec{k}$. It could be perpendicular to $\vec{B}_0$ or in the remaining direction, having a radial component of $B_\omega \cos\theta$. Then the characteristic has the form

$$I(\theta) \propto 1 + \cos^2\theta, \tag{B.3}$$

which is equal to the directional characteristic assumed in section 4.3.

B.3 Proposal for Different Ion Species

As g_J factors with a finite L can have values different from 2, I thought that the situation gets really interesting for systems where the g-factor according to the Landé formula is zero: Here, the known offset by a rational number (in single-electron cases some value between 2/3 and 2) vanishes. An experiment will automatically be sensitive to the relativistic and quantum-electrodynamical shift on the accuracy level of the magnetic field measurement. However, such systems involve at least three valence electrons (a total spin of 3/2 or higher is required), which is a substantial challenge for theoretical predictions to meet the experimental accuracy.

B.4 Relative Transition Probabilities

Here is the omitted calculation, continuing the discussion after Eqn. B.2: There I gave the transition matrix elements $\langle i|\left[\vec{L} + 2\vec{S}\right]|f\rangle$, which contain the main information about the relative rates and also about the emission characteristic. Since the field $\vec{B}_\omega$ of the emitted photon does not act in the electron Hilbert space, we can calculate $\langle i|\,H_{\text{int}}\,|f\rangle \propto \langle i|\left[\vec{L} + 2\vec{S}\right] \cdot \vec{B}_\omega\,|f\rangle = \langle i|\left[\vec{L} + 2\vec{S}\right]|f\rangle \cdot \vec{B}_\omega$ independently and apply the scalar product afterwards .

Note the abbreviations for angular momentum states $|J, m_J\rangle$ as composed momenta from $L = 1$ and $S = 1/2$ with the Clebsch-Gordan coefficients:

$$\begin{aligned}
\left|\frac{3}{2}, +\frac{3}{2}\right\rangle &= \left|1\,\frac{1}{2}; 1\,\frac{1}{2}\right\rangle \equiv |1\rangle\,|\uparrow\rangle \equiv |1\uparrow\rangle \\
\left|\frac{3}{2}, +\frac{1}{2}\right\rangle &= \sqrt{\frac{1}{3}}\,|1\downarrow\rangle + \sqrt{\frac{2}{3}}\,|0\uparrow\rangle \\
\left|\frac{1}{2}, +\frac{1}{2}\right\rangle &= \sqrt{\frac{2}{3}}\,|1\downarrow\rangle - \sqrt{\frac{1}{3}}\,|0\uparrow\rangle \\
\left|\frac{1}{2}, -\frac{1}{2}\right\rangle &= -\sqrt{\frac{2}{3}}\,|-1\uparrow\rangle + \sqrt{\frac{1}{3}}\,|0\downarrow\rangle\,.
\end{aligned}$$

The equation $\vec{J} = \frac{1}{2}\vec{e}_x(J_+ + J_-) + \frac{1}{2i}\vec{e}_y(J_+ - J_-) + \vec{e}_z J_z$, where J_+ and J_- are rising and lowering operators for the z-component, holds for any angular momentum $\vec{J}$. We need the following relations for ladder operators:

$$\begin{aligned}
L_-\,|1\rangle &= \hbar\sqrt{2}\,|0\rangle & \qquad S_-\,|\uparrow\rangle &= \hbar\,|\downarrow\rangle \\
L_+\,|0\rangle &= \hbar\sqrt{2}\,|1\rangle & \qquad S_+\,|\downarrow\rangle &= \hbar\,|\uparrow\rangle \\
L_+\,|-1\rangle &= \hbar\sqrt{2}\,|0\rangle\,. & &
\end{aligned}$$

Now we can calculate the matrix elements

$$\begin{aligned}
&\left\langle\frac{3}{2}, \frac{3}{2}\right|\left[\vec{L} + 2\vec{S}\right]\left|\frac{1}{2}, \frac{1}{2}\right\rangle \\
&= \langle 1\uparrow|\left[\vec{L} + 2\vec{S}\right]\left[\sqrt{\frac{2}{3}}\,|1\downarrow\rangle - \sqrt{\frac{1}{3}}\,|0\uparrow\rangle\right] \\
&= \langle 1\uparrow|\left[\sqrt{\frac{2}{3}}\,|\downarrow\rangle\,\vec{L}\,|1\rangle - \sqrt{\frac{1}{3}}\,|\uparrow\rangle\,\vec{L}\,|0\rangle + \sqrt{\frac{2}{3}}\,|1\rangle\,2\vec{S}\,|\downarrow\rangle - \sqrt{\frac{1}{3}}\,|0\rangle\,2\vec{S}\,|\uparrow\rangle\right] \\
&= -\sqrt{\frac{1}{3}}\,\langle 1|\,\vec{L}\,|0\rangle + \sqrt{\frac{2}{3}}\,\langle\uparrow|\,2\vec{S}\,|\downarrow\rangle \\
&= -\sqrt{\frac{1}{3}}\left[\frac{1}{2}\vec{e}_x\hbar\sqrt{2} + \frac{1}{2i}\vec{e}_y\hbar\sqrt{2}\right] + 2\sqrt{\frac{2}{3}}\left[\frac{1}{2}\vec{e}_x\hbar + \frac{1}{2i}\vec{e}_y\hbar\right] \\
&= \sqrt{\frac{1}{6}}\hbar\left[\vec{e}_x - i\vec{e}_y\right] \qquad \text{(B.4)}
\end{aligned}$$

for the decay connected to frequency ν_6, which changes m_J (σ-polarization), and

$$\begin{aligned}
&\left\langle \frac{3}{2},\, \frac{1}{2}\right| \left[\vec{L}+2\vec{S}\right] \left|\frac{1}{2},\, \frac{1}{2}\right\rangle \\
&= \left[\sqrt{\frac{1}{3}}\left\langle 1\downarrow\right| + \sqrt{\frac{2}{3}}\left\langle 0\uparrow\right|\right] \left[\vec{L}+2\vec{S}\right] \left[\sqrt{\frac{2}{3}}\left|1\downarrow\right\rangle - \sqrt{\frac{1}{3}}\left|0\uparrow\right\rangle\right] \\
&= \left[\sqrt{\frac{1}{3}}\left\langle 1\downarrow\right| + \sqrt{\frac{2}{3}}\left\langle 0\uparrow\right|\right] \left[\sqrt{\frac{2}{3}}\left|\downarrow\right\rangle \vec{L}\left|1\right\rangle - \sqrt{\frac{1}{3}}\left|\uparrow\right\rangle \vec{L}\left|0\right\rangle + \sqrt{\frac{2}{3}}\left|1\right\rangle 2\vec{S}\left|\downarrow\right\rangle - \sqrt{\frac{1}{3}}\left|0\right\rangle 2\vec{S}\left|\uparrow\right\rangle\right] \\
&= \sqrt{\frac{2}{9}}\left\langle 1\right| \vec{L}\left|1\right\rangle + \sqrt{\frac{2}{9}}\left\langle\downarrow\right| 2\vec{S}\left|\downarrow\right\rangle - \sqrt{\frac{2}{9}}\left\langle 0\right| \vec{L}\left|0\right\rangle - \sqrt{\frac{2}{9}}\left\langle\uparrow\right| 2\vec{S}\left|\uparrow\right\rangle \\
&= \sqrt{\frac{2}{9}}\hbar\vec{e}_z - \sqrt{\frac{2}{9}}\hbar\vec{e}_z - \sqrt{\frac{2}{9}}\hbar\vec{e}_z = -\sqrt{\frac{2}{9}}\hbar\vec{e}_z
\end{aligned} \tag{B.5}$$

for the π wave at frequency ν_4. The σ transition of the $|3/2,\, 1/2\rangle$ state comes with the frequency ν_5 and the dipole moment:

$$\begin{aligned}
&\left\langle \frac{3}{2},\, +\frac{1}{2}\right| \left[\vec{L}+2\vec{S}\right] \left|\frac{1}{2},\, -\frac{1}{2}\right\rangle \\
&= \left[\sqrt{\frac{1}{3}}\left\langle 1\downarrow\right| + \sqrt{\frac{2}{3}}\left\langle 0\uparrow\right|\right] \left[\vec{L}+2\vec{S}\right] \left[-\sqrt{\frac{2}{3}}\left|-1\uparrow\right\rangle + \sqrt{\frac{1}{3}}\left|0\downarrow\right\rangle\right] \\
&= \left[\sqrt{\frac{1}{3}}\left\langle 1\downarrow\right| + \sqrt{\frac{2}{3}}\left\langle 0\uparrow\right|\right] \left[-\sqrt{\frac{2}{3}}\left|\uparrow\right\rangle \vec{L}\left|-1\right\rangle + \sqrt{\frac{1}{3}}\left|\downarrow\right\rangle \vec{L}\left|0\right\rangle - \sqrt{\frac{2}{3}}\left|-1\right\rangle 2\vec{S}\left|\uparrow\right\rangle + \sqrt{\frac{1}{3}}\left|0\right\rangle 2\vec{S}\left|\downarrow\right\rangle\right] \\
&= \frac{1}{3}\left\langle 1\right| \vec{L}\left|0\right\rangle - \frac{2}{3}\left\langle 0\right| \vec{L}\left|-1\right\rangle + \sqrt{\frac{2}{9}}\left\langle\uparrow\right| 2\vec{S}\left|\downarrow\right\rangle \\
&= \frac{1}{3}\left[\frac{1}{2}\vec{e}_x\hbar\sqrt{2} + \frac{1}{2i}\vec{e}_y\hbar\sqrt{2}\right] - \frac{2}{3}\left[\frac{1}{2}\vec{e}_x\hbar\sqrt{2} + \frac{1}{2i}\vec{e}_y\hbar\sqrt{2}\right] + 2\sqrt{\frac{2}{9}}\left[\frac{1}{2}\vec{e}_x\hbar + \frac{1}{2i}\vec{e}_y\hbar\right] \\
&= \sqrt{\frac{1}{18}}\hbar\left[\vec{e}_x - i\vec{e}_y\right].
\end{aligned} \tag{B.6}$$

For the derivation of the partial decay rates we assume an equal distribution of $\vec{B}_\omega$ components in the vacuum fluctuations causing the spontaneous decay. The partial rate for a σ decay is then

$$\begin{aligned}
R_{3/2\to 1/2} &= R(B_\omega\vec{e}_x) + R(B_\omega\vec{e}_y) + R(B_\omega\vec{e}_z) \\
&= c\cdot\left[\left|\sqrt{\frac{1}{6}}\right|^2 + \left|\sqrt{\frac{1}{6}}\right|^2 + 0\right] = c\cdot\frac{1}{3}
\end{aligned}$$

and

$$\begin{aligned}
R_{1/2\to -1/2} &= R(B_\omega\vec{e}_x) + R(B_\omega\vec{e}_y) + R(B_\omega\vec{e}_z) \\
&= c\cdot\left[\left|\sqrt{\frac{1}{18}}\right|^2 + \left|\sqrt{\frac{1}{18}}\right|^2 + 0\right] = c\cdot\frac{1}{9},
\end{aligned}$$

from the respective initial state. There is only one type of a π decay:

$$\begin{aligned} R_{1/2\to 1/2} &= R(B_\omega \vec{e}_x) + R(B_\omega \vec{e}_y) + R(B_\omega \vec{e}_z) \\ &= c \cdot \left[0 + 0 + \left| \sqrt{\frac{2}{9}} \right|^2 \right] = c \cdot \frac{2}{9}. \end{aligned}$$

We have defined $c = \frac{2\pi}{\hbar^2} \left[\frac{\mu_B}{\hbar} B_\omega \right]^2$, where B_ω is the amplitude of one component in the quantum electrodynamical magnetic field fluctuation at the transition frequency $\omega = 2\pi \cdot 6.8 \cdot 10^{14}\,\mathrm{Hz}$.

Appendix C

List of Abbreviations

AC alternating current

AOM acousto-optical modulator

ARES axial resonator

Chn channel

CI counter input

CPM channel photomultiplier

CRES cyclotron resonator

CT creation trap

DC direct current

FC Faraday cup

FEP field-emission point

FSR free spectral range

FWHM full width of half maximum

GND ground

HE Hut-Einheit = hat unit

HITRAP decelerator for heavy highly charged ions produced at GSI

HV high voltage

LN low noise

LV low voltage

OFHC oxygen-free high thermal conductivity

PD photodiode

PEEK polyether ether ketone

PMT photomultiplier tube

ppm, ppb parts per million (10^{-6}), parts per billion (10^{-9})

QED quantum electrodynamics

RF radio frequency

RV rotary vane

ST spectroscopy trap

TTL transistor-to-transistor logic

UMF Unterer Montage-Flansch = lower mounting flange

WGD watchdog

Bibliography

[AAS+12] Albrecht, S. ; Altenburg, S. ; Siegel, C. ; Herschbach, N. ; Birkl, G.: A laser system for the spectroscopy of highly charged bismuth ions. In: *Appl. Phys. B* 107 (2012), Nr. 4, S. 1069–1074. DOI: 10.1007/s00340-011-4732-8

[AHKN15] Aoyama, Tatsumi ; Hayakawa, Masashi ; Kinoshita, Toichiro ; Nio, Makiko: Tenth-order electron anomalous magnetic moment: Contribution of diagrams without closed lepton loops. In: *Phys. Rev. D* 91 (2015), Feb, 033006. DOI: 10.1103/PhysRevD.91.033006

[Alb14] Albrecht, S.: *Ein Lasersystem zur Spektroskopie von hochgeladenen Ionen, Tellurmoleklen und Rubidium-Rydberg-Zustnden*, Technische Universität Darmstadt, PhD thesis, 2014. – (Engl. translation: A laser system for spectroscopy of highly charged ions, tellurium molecules, and Rydberg states in rubidium)

[Alo07] Alonso Otamendi, J.: *Development of an Experiment for Ultrahigh-Precision g-Factor Measurements in a Penning-Trap Setup*, Johannes-Gutenberg-Universität Mainz, PhD thesis, 2007

[AST+07] Artemyev, A.N. ; Shabaev, V.M. ; Tupitsyn, I.I. ; Plunien, G. ; Yerokhin, V.A.: QED Calculation of the $2p_{3/2} - 2p_{1/2}$ Transition Energy in Boronlike Argon. In: *Phys. Rev. Lett.* 98 (2007), Nr. 173004. DOI: 10.1103/PhysRevLett.98.173004

[AST+13] Artemyev, A.N. ; Shabaev, V.M. ; Tupitsyn, I.I. ; Plunien, G. ; Surzhykov, A. ; Fritzsche, S.: *Ab initio* calculations of the $2p_{3/2} - 2p_{1/2}$ fine-structure splitting in boronlike ions. In: *Phys. Rev. A* 88 (2013), 032518. DOI: 10.1103/PhysRevA.88.032518

[BCG+11] Bouchendira, R. ; Cladé, P. ; Guellati-Khélifa, S. ; Nez, F. ; Biraben, F.: New Determination of the Fine Structure Constant and Test of the Quantum Electrodynamics. In: *Phys. Rev. Lett.* 106 (2011), Feb, 080801. DOI: 10.1103/PhysRevLett.106.080801

[BG82] Brown, Lowell S. ; Gabrielse, Gerald: Precision spectroscopy of a charged particle in an imperfect Penning trap. In: *Phys. Rev. A* 25 (1982), 2423–2425. DOI: 10.1103/PhysRevA.25.2423

[BHM+93] Bollinger, J.J. ; Heinzen, D.J. ; Moore, F.L. ; Itano, W.M. ; Wineland, D.J. ; Dubin, D.H.E.: Electrostatic modes of ion-trap plasmas. In: *Phys. Rev. A* 48 (1993), S. 525–545. DOI: 10.1103/PhysRevA.48.525

[BKS06] Becker, R. ; Kester, O. ; Stöhlker, Th.: Simulation of Charge Breeding for Trapped Ions. In: *HCI*, 2006

[BPB+88] Brewer, L.R. ; Prestage, J.D. ; Bollinger, J.J. ; Itano, Wayne M. ; Larson, D.J. ; Wineland, D.J.: Static properties of a non-neutral $^9Be^+$-ion plasma. In: *Phys. Rev. A* 38 (1988), 859–873. DOI: 10.1103/PhysRevA.38.859

[Bre28] Breit, G.: The Magnetic Moment of the Electron. In: *Nature* 122 (1928), Nr. 649. http://www.nature.com/nature/journal/v122/n3078/pdf/122649a0.pdf

[BVST12] Bharadia, S. ; Vogel, M. ; Segal, D.M. ; Thompson, R.C.: Dynamics of laser-cooled Ca^+ ions in a Penning trap with a rotating wall. In: *Applied Physics B* 107 (2012), Nr. 4, 1105-1115. DOI: 10.1007/s00340-012-4871-6. – ISSN 0946–2171

[Cre10] Crespo López-Urrutia, J.R.: *DITHER simulation software of charge breeding.* Private communication, 2010

[DCD+03] Draganić, I. ; Crespo López-Urrutia, J.R. ; DuBois, R. ; Fritzsche, S. ; Shabaev, V.M. ; Orts, R. S. ; Tupitsyn, I.I. ; Zou, Y. ; Ullrich, J.: High PrecisionWavelength Measurements of QED-Sensitive Forbidden Transitions in Highly Charged Argon Ions. In: *Phys. Rev. Lett.* 91 (2003), Nr. 183001. DOI: 10.1103/PhysRevLett.91.183001

[DDD+09] Donets, D.E. ; Donets, E.D. ; Donets, E.E. ; Salnikov, V.V. ; Shutov, V.B. ; Syresin, E.M.: Production and ion-ion cooling of highly charged ions in electron string ion source. In: *Rev. Sci. Instrum.* 80 (2009), Nr. 063304. DOI: 10.1063/1.3152336

[Dem93] Demtröder, W.: *Laserspektroskopie.* Berlin : Springer, 1993

[Dir28] Dirac, P.A.M.: The Quantum Theory of the Electron. In: *Proc. Roy. Soc. London A* 117 (1928), Nr. 610. DOI: 10.1098/rspa.1928.0023

[DO99] Dubin, D.H.E. ; O'Neil, T.M.: Trapped nonneutral plasmas, liquids, and crystals (the thermal equilibrium states). In: *Rev. Mod. Phys.* 71 (1999), 87–172. DOI: 10.1103/RevModPhys.71.87

[Ein05] Einstein, A.: Über einen die Erzeugung und Verwandlung des Lichtes betreffenden heuristischen Gesichtspunkt. In: *Annalen der Physik* 322 (1905), Nr. 6, S. 132–148. DOI: 10.1002/andp.19053220607

[Fey49] Feynman, R. P.: Space-Time Approach to Quantum Electrodynamics. In: *Phys. Rev.* 76 (1949), Sep, 769–789. DOI: 10.1103/PhysRev.76.769

[GHR89] Gabrielse, G. ; Haarsma, L. ; Rolston, S.L.: Open-endcap Penning traps for high precision experiments. In: *Int. J. of Mass Spectrom. and Ion Processes* 88 (1989), Nr. 23, 319 - 332. DOI: 10.1016/0168-1176(89)85027-X. – ISSN 0168–1176

[Gla15] Glazov, D.A.: *Significant progress in quadratic effect.* Private communication, 2015

[GM84] Gabrielse, G. ; Mackintosh, F.C.: Cylindrical Penning traps with orthogonalized anharmonicity compensation. 57 (1984), Nr. 1, 1 - 17. DOI: 10.1016/0168-1176(84)85061-2. – ISSN 0168–1176

[GVS+13] Glazov, D.A. ; Volotka, A.V. ; Schepetnov, A.A. ; Sokolov, M.M. ; Shabaev, V.M. ; Tupitsyn, I.I. ; Plunien, G.: g factor of boron-like ions: ground and excited states. In: *Phys. Scr.* 2013 (2013), Nr. T156, 014014. DOI: 10.1088/0031-8949/2013/T156/014014

[HBH+00] Häffner, H. ; Beier, T. ; Hermanspahn, N. ; Kluge, H.-J. ; Quint, W. ; Stahl, S. ; Verdú, J. ; Werth, G.: High-Accuracy Measurement of the Magnetic Moment Anomaly of the Electron Bound in Hydrogenlike Carbon. In: *Phys. Rev. Lett.* 85 (2000), 5308–5311. DOI: 10.1103/PhysRevLett.85.5308

[HFG08] Hanneke, D. ; Fogwell, S. ; Gabrielse, G.: New Measurement of the Electron Magnetic Moment and the Fine Structure Constant. In: *Phys. Rev. Lett.* 100 (2008), Mar, 120801. DOI: 10.1103/PhysRevLett.100.120801

[Hül11] Hüllen, M.: *Entwicklung und Test eines elektronischen Nachweissystems für hoch geladene Ionen in einer Penning-Falle*, Hochschule Karlsruhe, Bachelor thesis, 2011. – (Engl. translation: Development and test of an electronic detection system for highly charged ions in a Penning trap)

[Jac75] Jackson, J.D.: *Classical Electrodynamics*. New York : Wiley, 1975

[KF47] Kusch, P. ; Foley, H. M.: Precision Measurement of the Ratio of the Atomic 'g Values' in the ${}^2P_{\frac{3}{2}}$ and ${}^2P_{\frac{1}{2}}$ States of Gallium. In: *Phys. Rev.* 72 (1947), S. 1256–1257. DOI: 10.1103/PhysRev.72.1256.2

[KF48] Kusch, P. ; Foley, H. M.: The Magnetic Moment of the Electron. In: *Phys. Rev.* 74 (1948), S. 250–263. DOI: 10.1103/PhysRev.74.250

[KL49] Kroll, N.M. ; Lamb, W.E.: On the Self-Energy of a Bound Electron. In: *Phys. Rev.* 75 (1949), S. 388–398. DOI: 10.1103/PhysRev.75.388

[Koc09] Koc, K.: Relativistic multireference configuration interaction calculations of lifetime of $2s^2 2p\ {}^2P_{3/2}$ level along boron isoelectronic sequence. In: *Eur. Phys. J. D* 53 (2009), Nr. 9. DOI: 10.1140/epjd/e2009-00086-8

[LBB+11] Lindenfels, D. v. ; Brantjes, N.P.M. ; Birkl, G. ; Quint, W. ; Shabaev, V.M. ; Vogel, M.: Bound Electron g-Factor Measurement by Double-Resonance Spectroscopy on a Fine-Structure Transition. In: *Can. J. Phys.* 89 (2011), Nr. 79. DOI: 10.1139/P10-071

[LGW+13] Lindenfels*, D. von ; Glässel, J. ; Wiesel, M. ; Birkl, G. ; Quint*, W. ; Vogel*, M.: Characterization of a croygenic adsorption valve for inert gases. Version: 2013. `http://repository.gsi.de/record/52266`. In: Grosse, K. (Ed.): *Scientific Report 2012* Bd. 2013-1. Darmstadt : GSI Helmholtzzentrum für Schwerionenforschung, 2013. – ISSN 0171–4546, 373 p.

[Lin10] Lindenfels, D. v.: *Development of an Ion Trap Experiment for the Measurement of the Electron Magnetic Moment by Double-Resonance Spectroscopy*, University of Heidelberg, Diploma thesis, 2010. "http://www.gsi.de/documents/DOC-2011-Feb-63-1.pdf"

[LJC+05] Lapierre, A. ; Jentschura, U.D. ; Crespo López-Urrutia, J.R. ; Braun, J. ; Brenner, G. ; Bruhns, H. ; Fischer, D. ; González Martínez, A.J. ; Harman, Z. ; Johnson, W.R. ; Keitel, C.H. ; Mironov, V. ; Osborne, C.J. ; Sikler, G. ; Soria Orts, R. ; Shabaev, V. ; Tawara, H. ; Tupitsyn, I.I. ; Ullrich, J. ; Volotka, A.: Relativistic Electron Correlation, Quantum Electrodynamics, and the Lifetime of the $1s^2 2s^2 2p\,^2P^o_{3/2}$ Level in Boronlike Argon. In: *Phys. Rev. Lett.* 95 (2005), Nr. 183001. DOI: 10.1103/PhysRevLett.95.183001

[LR47] Lamb, W.E. ; Retherford, R.C.: Fine Structure of the Hydrogen Atom by a Microwave Method. In: *Phys. Rev.* 72 (1947), S. 241–243. DOI: 10.1103/PhysRev.72.241

[LVQ+14] Lindenfels, D. v. ; Vogel, M. ; Quint, W. ; Birkl, G. ; Wiesel, M.: Half-open Penning trap with efficient light collection for precision laser spectroscopy of highly charged ions. In: *Hyp. Int.* 227 (2014), Nr. 197-207. DOI: 10.1007/s10751-013-0961-z

[LWG+13] Lindenfels, D. v. ; Wiesel, M. ; Glazov, D.A. ; Volotka, A.V. ; Sokolov, M.M. ; Shabaev, V.M. ; Plunien, G. ; Quint, W. ; Birkl, G. ; Martin, A. ; Vogel, M.: Experimental access to higher-order Zeeman effects by precision spectroscopy of highly charged ions in a Penning trap. In: *Phys. Rev. A* 87 (2013), S. 023412. DOI: 10.1103/PhysRevA.87.023412

[Mae08] Maero, G.: *Cooling of highly charged ions in a Penning trap for HITRAP*, Ruprecht-Karls-Universität Heidelberg, PhD thesis, 2008

[Mag08] Magnex Scientific / Varian Inc / Agilent Technologies: *7T/160AS Vertical Magnet Customer Interface ANZ341861A*. Oxford, UK : Unpublished, Nov 2008

[Man86] Mann, R.: Total one-electron capture cross sections for Ar^{q+} and I^{q+} ions in slow collisions on H_2 and He. In: *Zeitschrift fr Physik D Atoms, Molecules and Clusters* 3 (1986), Nr. 1, 85-90. DOI: 10.1007/BF01442351. – ISSN 0178–7683

[Mar10] Marzini, C.: *Simulations with CBSIM and Molflow*. Private communication, 2010

[MGW05] Major, F.G. ; Gheorghe, V.N. ; Werth, G.: *Charged Particle Traps*. Heidelberg : Springer, 2005

[MIP12] Marques, J.P. ; Indelicato, P. ; Parente, F.: Relativistic multiconfiguration calculations of the $2s^2 2p\ ^2P_{3/2}$ level lifetime along the boron isoelectronic sequence. In: *Eur. Phys. J. D* 66 (2012), Nr. 324. DOI: 10.1140/epjd/e2012-30338-3

[MKB+11] Mäckel, V. ; Klawitter, R. ; Brenner, G. ; Crespo López-Urrutia, J.R. ; Ullrich, J.: Laser Spectroscopy on Forbidden Transitions in Trapped Highly Charged Ar^{13+} Ions. In: *Phys. Rev. Lett.* 107 (2011), Nr. 143002. DOI: 10.1103/PhysRevLett.107.143002

[MS08] Malyshev, O. ; Sharipov, F.: *Software for Modelling of Free Molecular Flows.* 2008

[Nat14] Natarajan, L.: *Fully relativistic calculations on the life time of $^2P_{3/2}$ state of B-like Ar.* Private communication, 2014

[PAMC82] Phaneuf, R. A. ; Alvarez, I. ; Meyer, F. W. ; Crandall, D. H.: Electron capture in low-energy collisions of C^{q+} and O^{q+} with H and H_2. In: *Phys. Rev. A* 26 (1982), S. 1892–1906. DOI: 10.1103/PhysRevA.26.1892

[Pla00] Planck, M.: *Zur Theorie des Gesetzes der Energieverteilung im Normalspectrum.* `http://www.christoph.mettenheim.de/planck-energieverteilung.pdf`. Version: 1900. – In: Verhandlungen der Deutschen physikalischen Gesellschaft. 2, No. 17, p. 245, Berlin

[QMSV08] Quint, W. ; Moskovkhin, D.L. ; Shabaev, V.M. ; Vogel, M.: Laser-microwave double-resonance technique for g-factor measurements in highly charged ions. In: *Phys. Rev. A* 78 (2008), Sep, 032517. DOI: 10.1103/PhysRevA.78.032517

[RKRN11] Ralchenko, Y. ; Kramida, A.E. ; Reader, J. ; N.A.S.D. Team: *NIST Atomic Spectra Database.* `http://physics.nist.gov/asd`. Version: 2011. – National Institute of Standards and Technology, Gaithersburg

[San15] Santos, J.P.: *Calculation of g-factors for boron-like argon.* Private communication, 2015

[SCB+07] Soria Orts, R. ; Crespo López-Urrutia, J.R. ; Bruhns, H. ; González Martínez, A.J. ; Harman, Z. ; Jentschura, U.D. ; Keitel, C.H. ; Lapierre, A. ; Tawara, H. ; Tupitsyn, I.I. ; Ullrich, J. ; Volotka, A.V.: Zeeman splitting and g factor of the $1s^22s^22p\ ^2P_{3/2}$ and $^2P_{1/2}$ levels in Ar^{13+}. In: *Phys. Rev. A* 76 (2007), Nr. 052501. DOI: 10.1103/PhysRevA.76.052501

[Sch26] Schrödinger, E.: Quantisierung als Eigenwertproblem. In: *Annalen der Physik* 384 (1926), Nr. 4, S. 361–376. DOI: 10.1002/andp.19263840404

[Sch48] Schwinger, Julian: On Quantum-Electrodynamics and the Magnetic Moment of the Electron. In: *Phys. Rev.* 73 (1948), Feb, 416–417. DOI: 10.1103/PhysRev.73.416

[SGO+06] Shabaev, V. M. ; Glazov, D. A. ; Oreshkina, N. S. ; Volotka, A. V. ; Plunien, G. ; Kluge, H.-J. ; Quint, W.: g-Factor of Heavy Ions: A New Access to the Fine Structure Constant. In: *Phys. Rev. Lett.* 96 (2006), 253002. DOI: 10.1103/PhysRevLett.96.253002

[SGV+15] Shchepetnov, A.A. ; Glazov, D.A. ; Volotka, A.V. ; Shabaev, V.M. ; Tupitsyn, I.I. ; Plunien, G.: Nuclear recoil correction to the g factor of boron-like argon. In: *J. Phys.: Conf. Ser.* 583 (2015), Nr. 012001. DOI: 10.1088/1742-6596/583/1/012001

[Sha15] Shabaev, V.M.: *Independence of g-factor uncertainties.* Private communication, 2015

[SKZ+14] Sturm, S. ; Köhler, F. ; Zatorski, J. ; Wagner, A. ; Harman, Z. ; Werth, G. ; Quint, W. ; Keitel, C. H. ; Blaum, K.: High-precision measurement of the atomic mass of the electron. In: *Nature* 506 (2014), Februar, Nr. 7489, 467–470. DOI: 10.1038/nature13026. – ISSN 0028–0836, 1476–4687

[SRHR05] Scholl, T.J. ; Rehse, S.J. ; Holt, R.A. ; Rosner, S.D.: Absolute wave-number measurements in $^{130}Te_2$: reference lines spanning the 420.9-464.6-nm region. In: *J. Opt. Soc. Am. B* 22 (2005), Nr. 5, S. 1128–1133. DOI: 10.1364/JOSAB.22.001128

[Sta13] Stahl, S.: *Quotes for experimental electronics.* Mettenheim, Germany : Private communication, 2013

[Ste15] Steinmann, J: *Modeling and numerical investigation of the resistive cooling technique applied to ion clouds*, Universität Erlangen, PhD thesis, 2015

[SWS+11] Sturm, S. ; Wagner, A. ; Schabinger, B. ; Zatorski, J. ; Harman, Z. ; Quint, W. ; Werth, G. ; Keitel, C. H. ; Blaum, K.: g Factor of Hydrogenlike $^{28}Si^{13+}$. In: *Phys. Rev. Lett.* 107 (2011), Jul, 023002. DOI: 10.1103/PhysRevLett.107.023002

[Tin86] Tingwei Xu and J-M. Laurent and O. Gröbner: Monte Carlo Simulation of the Pressure and of the Effective Pumping Speed in the Large Electron Positron Collider (LEP) / CERN. 1986 (LEP-VA/86-02). – Forschungsbericht

[Ulm11] Ulmer, S.: *First Observation of Spin Flips with a Single Proton Stored in a Cryogenic Penning Trap*, Ruprecht-Karls-Universität Heidelberg, PhD thesis, 2011

[VDS+04] Verdú, J. ; Djekić, S. ; Stahl, S. ; Valenzuela, T. ; Vogel, M. ; Werth, G. ; Beier, T. ; Kluge, H.-J. ; Quint, W.: Electronic g Factor of Hydrogenlike Oxygen $^{16}O^{7+}$. In: *Phys. Rev. Lett.* 92 (2004), Mar, S. 093002. DOI: 10.1103/PhysRevLett.92.093002

[VHH+14] Vogel, M. ; Häffner, H. ; Hermanspahn, K. ; Stahl, S. ; Steinmann, J. ; Quint, W.: Resistive and sympathetic cooling of highly-charged-ion clouds in a Penning trap. In: *Phys. Rev. A* 90 (2014), S. 043412. DOI: 10.1103/PhysRevA.90.043412

[Vog14] Vogel, Chr., Technische Universität Darmstadt, Bachelor thesis, 2014

[Vol14] Vollrath, F.: *Aufbau eines Lasersystems zum Spektroskopieren der Feinstrukturaufspaltung von Ar^{13+}-Ionen bei 441 nm*, Technische Universität Darmstadt, Master thesis, 2014. – (Engl. translation: Installation of a laser system for spectroscopy of Ar^{13+} ions at 441 nm)

[VQN10] Vogel, Manuel ; Quint, Wolfgang ; Nörtershäuser, Wilfried: Trapped Ion Oscillation Frequencies as Sensors for Spectroscopy. In: *Sensors* 10 (2010), Nr. 3, 2169. DOI: 10.3390/s100302169. – ISSN 1424–8220

[WD75] Wineland, D.J. ; Dehmelt, H.G.: Principles of the stored ion calorimeter. In: *Journal of Applied Physics* 46 (1975), Nr. 2, S. 919–930. DOI: 10.1063/1.321602

[Wie12] Wiesel, M.: *Cryotechnical Setup of ARTEMIS - an Experiment for Precision Spectroscopy on Highly Charged Ions in a Penning Trap*, University of Heidelberg, Diploma thesis, 2012

[WVST06] Winters, D.F.A. ; Vogel, M. ; Segal, D.M. ; Thompson, R.C.: Electronic detection of charged particle effects in a Penning trap. In: *Journal of Physics B: Atomic, Molecular and Optical Physics* 39 (2006), Nr. 14, 3131. DOI: 10.1088/0953-4075/39/14/019

[YDP89] Yu, J. ; Desaintfuscien, M. ; Plumelle, F.: Ion density limitation in a Penning trap due to the combined effect of asymmetry and space charge. In: *Applied Physics B* 48 (1989), Nr. 1, 51-54. DOI: 10.1007/BF00694417. – ISSN 0946–2171

Danksagung

Allen voran danke ich Wolfgang Quint für die Möglichkeit, nach der Diplomarbeit auch meine Dissertation an dem ARTEMIS-Projekt anzufertigen, das mich so fasziniert. Danke für den Rahmen, die Betreuung, den vielen Austausch, den Einsatz für Vertragsverlängerungen und vieles mehr. Danke auch an Chr. Keitel, A. Di Piazza und S. Babacan von der IMRPS-QD in Heidelberg, dass Sie mich so lange beschäftigt haben, und an Th. Stöhlker, S. Lüttges und T. Litvinova von der Atomphysik bei GSI für die Abfederung nach dem Ablauf meines Vertrags. Danke M. DeKieviet und K. Blaum für die Mitbetreuerschaft sowie M. Oberthaler, U. Platt und Th. Gasenzer für die Bereitschaft als Gutachter und Prüfer meine Promotion zu begleiten. Ich danke auch F. Schmidt-Kaler und seiner Gruppe, dass sie mich so freundlich aufgenommen und mir schon jetzt eine Stelle nach der Promotion zugesichert hat. And thanks to G. Gabrielse and his team DAAD for the time I could spend at Harvard and for mentioning me in your publication.

Vielen Dank an die ARTEMIS-Crew, Manuel Vogel, Marco Wiesel, M. Sadegh Ebrahimi, G. Birkl, Alexander Martin, Patrick Baus, Florian Vollrath und Christian Vogel, ohne die das Schiff schon längst gesunken wäre. Besonderen Dank, dass ihr die Messungen mit hohem Einsatz weitergeführt habt, als ich mich aus dem Labor zurückziehen musste. Auch dem Abteilungs-Freundeskreis von der GSI, erweitert um Tobias Murböck, Stefan Schmidt, Tobias Gaßner, Zoran Andelkovic und Rodolfo Sánchez, und natürlich den Ehemaligen Benjamin Botermann und Matthias Lochmann möchte ich für die freundschaftliche Atmosphäre am Arbeitsplatz und darüber hinaus danken. Ich würdige die Beiträge der Werk- und Sommerstudenten sowie Praktikanten Rubain Sateu, Mouwafak Shaaban Konstantin Mohr, Julian Glässel, Katharina, Andre, Valentin und Paul.

Thanks to many colleagues from GSI and all over the world for help and inspiring discussions. Here I want to name Stefan Stahl, Vladimir M. Shabaev, Dmitry A. Glazov, Stefan Ulmer, Ina Alber, Pierre-Michel Hillenbrand. Dem treuen Personal der GSI sei für vielfältige Mühen gedankt. Hier kann ich nur beispielhaft Stefan Wilfert, Claus Schroeder, Davide Racano, E. Kammer, M. Müller, Herrn Heinz, K. Schiebel und Bastian Neuburger nennen.

Jetzt ist es an der Zeit, meinen Eltern Andreas und Christa zu danken, dass sie mir das Studium überhaupt erst ermöglicht und mich auf so viele Weise bis heute unterstützt haben. Danke euch und auch meinen Geschwistern mit Ehepartnern, Christoph und Julia, Albrecht und Julia, und auch Birgit für euer Zittern mit mir bis zum Schluss. Auch meine Gemeinde und besonders der Hauskreis, Britta, Debbie, Viola, Maximos, André, Jonas und Pascal sowie unsere Trauzeugen Niklas Johannes Hoffmann und Julia Leichthammer haben mir immer wieder Mut gemacht. Ganz besonders danke ich meiner Frau Jennifer, die in den letzten Wochen sehr viel auf mich verzichtet

hat und doch so treu für mich da war – ich liebe dich! Ich bin so froh, mit dir das Leben zu teilen und auch bald selber wieder viel Zeit für dich zu haben.

Gott... Hat es spannend gemacht. Hat meinen Wunsch nach einer laserspektroskopischen Messung nicht erfüllt. Aber manchmal muss ich eben auf die harte Tour lernen, dass es nicht nach meinen Wünschen geht. Dass der Mensch nicht vom Brot allein lebt. Dass ich nur dich brauche. Und dass du mir - wenn auch nicht diese – so doch andere schöne Messungen geschenkt hast! Danke, dass du bei mir bist in der größten Not, dass du all den Schmerz am eigenen Leib gespürt hast, dass du mich erlöst hast aus der Grube, in die ich mich von der Panik hatte hineinziehen lassen. In den letzten Wochen hatten mich Worte aus den Psalmen sehr ermutigt, aus denen ich noch zitieren möchte:

> „Halleluja! Lobe den HERRN, meine Seele!
> Loben will ich den HERRN mein Leben lang, will spielen meinem Gott, solange ich bin.
> Vertraut nicht auf Edle, auf einen Menschensohn, bei dem keine Hilfe ist!
> Sein Geist geht aus, er kehrt wieder zu seiner Erde: am selben Tag gehen seine Pläne verloren.
> Glücklich der, dessen Hilfe der Gott Jakobs ist, dessen Hoffnung auf dem HERRN, seinem Gott, steht,
> der Himmel und Erde gemacht hat, das Meer und alles, was in ihnen ist; der Treue hält auf ewig.
> Er schafft Recht den Bedrückten, er gibt den Hungrigen Brot. Der HERR macht die Gefangenen frei.
> Der HERR öffnet die Augen der Blinden. Der HERR richtet die Gebeugten auf. Der HERR liebt die Gerechten.
> Der HERR behütet die Fremdlinge, Waisen und Witwen hilft er auf; aber er krümmt den Weg der Gottlosen.
> Der HERR wird regieren in Ewigkeit, dein Gott, Zion, von Generation zu Generation. Halleluja! “
>
> Psalm 146, Revidierte Elberfelder Übersetzung